University of Alberta

Effect of Plasticity on Stress Corrosion Cracking Behavior of X-52 Pipeline Steel in Near-neutral pH Environment

by

Xiaochun LI ©

A thesis submitted to the Faculty of Graduate Studies and Research in partial fulfillment of the requirements for the degree of **Master of Science**

in

Materials Engineering

Department of Chemical and Materials Engineering

Edmonton, Alberta

Spring 2006

Library and
Archives Canada

Bibliothèque et
Archives Canada

Published Heritage
Branch

Direction du
Patrimoine de l'édition

395 Wellington Street
Ottawa ON K1A 0N4
Canada

395, rue Wellington
Ottawa ON K1A 0N4
Canada

NOTICE:
The author has granted a non-exclusive license allowing Library and Archives Canada to reproduce, publish, archive, preserve, conserve, communicate to the public by telecommunication or on the Internet, loan, distribute and sell theses worldwide, for commercial or non-commercial purposes, in microform, paper, electronic and/or any other formats.

The author retains copyright ownership and moral rights in this thesis. Neither the thesis nor substantial extracts from it may be printed or otherwise reproduced without the author's permission.

AVIS:
L'auteur a accordé une licence non exclusive permettant à la Bibliothèque et Archives Canada de reproduire, publier, archiver, sauvegarder, conserver, transmettre au public par télécommunication ou par l'Internet, prêter, distribuer et vendre des thèses partout dans le monde, à des fins commerciales ou autres, sur support microforme, papier, électronique et/ou autres formats.

L'auteur conserve la propriété du droit d'auteur et des droits moraux qui protège cette thèse. Ni la thèse ni des extraits substantiels de celle-ci ne doivent être imprimés ou autrement reproduits sans son autorisation.

In compliance with the Canadian Privacy Act some supporting forms may have been removed from this thesis.

While these forms may be included in the document page count, their removal does not represent any loss of content from the thesis.

Conformément à la loi canadienne sur la protection de la vie privée, quelques formulaires secondaires ont été enlevés de cette thèse.

Bien que ces formulaires aient inclus dans la pagination, il n'y aura aucun contenu manquant.

Canada

Abstract

This research focused on the effect of plasticity on stress corrosion cracking (SCC) of pipeline steel (X-52) in near-neutral pH environment. A simulated near-neutral pH soil solution, termed C1, was used for all the tests. The effects of elastic and plastic deformation on corrosion current were studied. Crack advance was measured in samples with various amounts of plastic deformation by three different techniques, slow strain rate tests (SSRT), potential drop tests and surface replica tests. Crack morphologies and the crack features on the fracture surface were observed by optical microscopy (OM) and scanning electron microscopy (SEM).

All the cracking tests indicated that the cracking rate was enhanced by the plastic deformation. The electrochemical tests showed that corrosion current increased with plastic deformation. The relationship between the cracking mechanisms and plastic deformation was discussed.

Key Words: SCC, near-neutral pH, pipeline steel, plastic deformation, crack growth rate, SSRT, potential drop, surface replica

Acknowledgement

I am earnestly grateful to my supervisors Dr. Regnald L.Eadie and Dr. Jingli Luo whose guidance, suggestions and encouragement led me throughout this thesis, they have always been willing to answer my questions and given me enough support to carry out all the work.

My special thanks should be given to my husband, Mr. Jiang Wang for his love and encouragement in every situation.

I would express my sincere appreciation to Dr. Baotong Lu for his valuable information, suggestion and motivation. I would like to acknowledge Mr. L.L.Zhou, Mr. A. Adeleke, Ms. H.X. Guo and Mr. B.Peng. Without their substantial help and valuable discussion, I cannot do the Master degree successfully.

Appreciation is extended to Mr. T. Barker, Mr. W. Boddez, Mr. B.Scott and all others in the machine shop.

Thanks are also sent to Alberta Energy Research Institute for their financial support through COURSE program.

Xiaochun LI

November 9, 2005

Table of Contents

List of Tables

List of Figures

List of Symbols

a	crack length
aq	absorbed
A	atomic weight
b_A	slope of anodic Tafel line
b_C	slope of cathodic Tafel line
B	sample thickness
C	cathode
D_s	self-diffusion coefficient
E_{corr}	corrosion potential
F	Faradays constant
i_A	anodic current density
i_C	cathodic current density
i_{corr}	corrosion current density
$I_{applied}$	applied constant current
k	Boltzmanns constant
K_I	stress-intensity factor
ΔK_I	difference between maximum and minimum stress-intensity factor
K_C	fracture toughness
K_{IC}	plane strain fracture toughness
K_{ISCC}	critical stress intensity factor for SCC
K_{max}	maximum stress-intensity factor
K_{min}	minimum stress-intensity factor
$K_{t\alpha}$	theoretical stress concentration factor for V-notched flat tensile bar
K_{tu}	stress concentration factor for U-notched flat tensile bar
L	length of sample
l_0	initial gauge length
l_d	gauge length of the strained sample by tensile loading.
n	strain hardening exponent
n	number of electrons in the anodic reaction

P	applied load
r_p	radius of plastic zone size
R	stress ratio
R	resistance
R^2	goodness of fit
R_p	polarization resistance
S	surface area
t	thickness
t_{air}	time to failure in air
t_{cp}	total failure time
t_o	initial thickness of the sample
t_d	thickness of deformed sample by cold rolling
t_{SCC}	time to failure in near-neutral pH solution
T	absolute temperature
V	corrosion rate by weight loss method
V	potential
W	sample width
Z	valence of the solvated species
ε_f	failure elongation
ε_T	true strain
ρ	density
ρ	resistivity
β	geometric factor
σ	stress
σ_{app}	applied stress
σ_{nom}	nominal stress
σ_{yi}	yield strength after releasing the load
σ_{yo}	initial yield strength

σ_{ys}	yield stress
$\sigma_{ys,SCC}$	yield strength in near-neutral pH solution
$\sigma_{ys,air}$	yield strength in air
σ_T	true stress
$\Delta\sigma$	difference of applied stress
η_A	anodic over-potential
η_C	cathodic over-potential
Δg	mass difference

List of Abbreviations

ASTM	American Society for Testing and Materials
CP	cathodic protection
C-SCC	circumferential stress corrosion cracking
C-T	compact toughness
EDX	energy dispersive x-ray
EDM	electrical discharging machining
EIC	environmentally induced cracking
HAC	hydrogen assisted cracking
HIC	hydrogen induced cracking
HV	Vickers hardness
Hrs	hours
IG	intergranular
IGSCC	intergranular stress corrosion cracking
mV	millivolts
mV_{SCE}	millivolts versus a saturated calomel electrode
MVC	microvoid coalescence
NEB	National Energy Board
OCP	open circuit potential
OM	optical microscope
PD	potentiodynamic scan
PR	polarization resistance
RA	reduction in area
%RA	percent reduction in area
RA_{air}	reduction of area of a specimen failed in air
RA_{scc}	reduction of area of a specimen failed due to SCC
SCC	stress corrosion cracking
SEM	scanning electron microscope
SIMS	secondary ion mass spectrometry
SMYS	specified minimum yield strength

SRB	sulfate-reducing bacteria
SSRT	slow strain rate test
TCPL	TransCanada Pipelines Ltd.
TG	transgranular
TGSCC	transgranular stress corrosion cracking
V_{SCE}	voltage versus a saturated calomel electrode
%CW	percent of cold work
%EL	percent of elongation

1 Introduction

There are more than 540,000 kilometres of buried oil and gas pipelines throughout Canada, which carry hydrocarbons in either gas or liquid form including natural gas, crude oil, and high vapour pressure products such as gasoline or jet fuel (NEB report, 1996). Since 1985, when the first near-neutral pH stress corrosion cracking (SCC) was observed by TransCanada PipeLines Ltd. (TCPL) in a tape-coated pipeline, tens of failure has been identified in the pipeline systems in Canada (NEB report, 1996). Near-neutral pH SCC is the form of SCC that is of most significance to Canadian pipelines and it is characterized by wide transgranular cracks in dilute carbonate-bicarbonate solutions with pH of the liquid under the coating in the range 5.5-7.5. Extensive field investigations and laboratory research have shown that a potent environment at the pipe surface which is achieved by the soil solution going through the coating to reach the steel surface, a susceptible pipe material and an adequate stress are the three conditions necessary for SCC occurrence.

Previously, substantial work has been done to investigate the effects of the three fundamental factors, but there is still a great deal that remains unknown or uncertain in terms of the roles played by the key factors such as stress and stress induced plastic deformation. From the design point of view, the structures are designed to try and ensure that only elastic deformation will result when they are operating under pressure. However localized plastic deformation from bending, rolling, or handling is often encountered in the manufacture and assembly of pipeline components that later are exposed to service conditions (Ahmed et al., 1997). There are also many naturally occurring discontinuities such as the longseam weld that will raise the local stress level above the elastic limit. Many corrosion situations such as pitting can cause local discontinuities that will elevate the stress locally above the yield strength. Furthermore, there are several other situations causing localized micro-plastic deformation at stress levels below the yield stress of the steel. Firstly, the surface layer of the pipe wall thickness can deform before the bulk of the wall thickness

1

(Leis, 1990); secondly, cyclic-loading can cause steels to exhibit micro-plastic strains at nominal stress levels where plastic strains would not be expected (CEPA, 1996). Also, hydrogen-assisted plasticity can occur, which may delay the exhaustion of the primary creep and increase the SCC susceptibility (Parkins, 1999). It is therefore desirable to know the pipeline's resistance to near-neutral pH SCC after it experiences some plastic deformation.

The objective of the present research was to investigate the effect of plastic deformation on the susceptibility of pipeline steel (X-52) to near-neutral pH SCC. The investigated plasticity in this study was induced either by cold rolling or tensile loading. The crack growth rate tests were carried out using traditional potential drop tests, slow strain rate tests and surface replica tests, and all the crack growth was occurring in the longitudinal direction of the pipe in order to simulate the situation in the field. Some fast-screening electrochemical tests were also undertaken to study the effect of anodic dissolution on near-neutral pH SCC.

This thesis is presented with a comprehensive literature review at the beginning. It reviews the severity, characteristics and mechanisms of near-neutral pH SCC, and the different methods used in SCC testing. In addition, some basic concepts about the conditions under which the steel experiences deformation and the previous work done on the effect of plasticity on SCC susceptibility are included in the section. This is followed by information about experimental details in Section 3. Then the test results and discussion are reported in Section 4. At last, a few conclusions are drawn based on the results and discussions and some recommendations are given. The references used in the thesis are listed at the end.

2

2 Literature Review

There are two types of SCC that cause failures on pipelines, which are referred to as high pH SCC and near-neutral pH SCC. The mechanism related to high pH SCC is much clearer, and a consensus exists that a preferential anodic dissolution and a film rupture mechanism prevails in this case (Sutcliffe et al., 1972, Pugh, 1985 and Jones, 1992, Pilkey et al., 1995). Since it has been studied for many years, it will not be included in the current literature review. However, the mechanisms of near-neutral pH SCC are far from being well understood (Parkins et al., 1994), this section reviews some of the previous research done on near-neutral pH SCC of pipeline steel. It begins with section 2.1, the severity of near-neutral pH SCC. Section 2.2 introduces the characteristics and fundamental factors which will lead to SCC. The possible mechanisms related to near-neutral pH SCC are discussed in section 2.3. This is followed by section 2.4, concerning the changes to mechanical properties when metals experience some deformation, and then the previous work done on the influence of cold work on SCC are reviewed in section 2.5. The last section, 2.6 will review the techniques for investigating SCC in the laboratory.

3

2.1 The severity of near-neutral pH SCC

SCC is a phenomenon in which time-dependent crack growth occurs when the necessary electrochemical, mechanical and metallurgical conditions exist (Jones, 1992). It is a delayed failure process that contains the following three processes as shown in Figure 2-1:

(1) Crack initiation, stage 1

(2) Steady-state crack propagation, stage 2

(3) Final fracture failure (mechanical fracture), stage 3
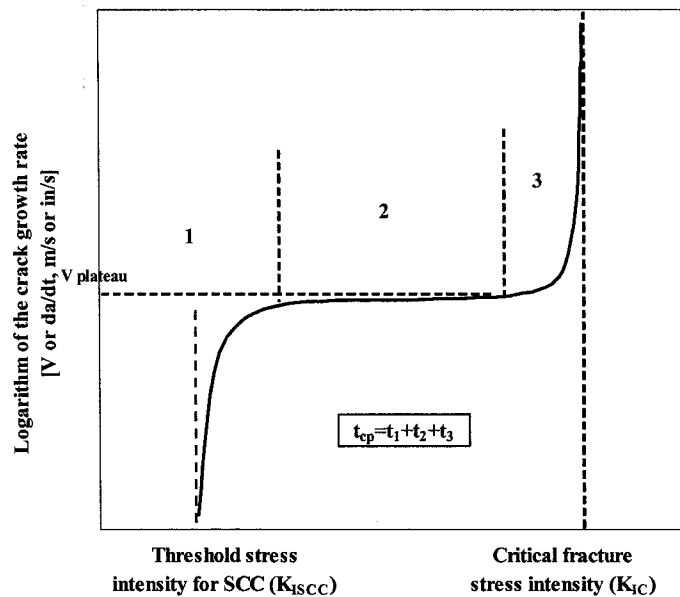
Figure 2-1 Schematic diagram of typical crack-propagation rate as a function of crack- tip stress intensity behavior, illustrating the regions of stage 1, 2 and 3 crack propagation as well as identifying the plateau velocity and the threshold stress intensity (From Jones, 1992)

2.1.1 Failure history

TCPL had three failures on the Northern Ontario portion of the pipeline between March 1985 and March 1986. These failures were attributed to near-neutral pH SCC and were considered at the time to be the first evidence of SCC in Canada. TransCanada experienced its fourth and fifth SCC-related pipeline ruptures in

4

December 1991 near Cardinal, Ontario, and in July 1992 near Tunis, Ontario. From 1977 to 1996, near-neutral pH SCC had caused 22 pipeline failures in Canada. The 22 failures included 12 ruptures and 10 leaks on both natural gas and liquids pipeline systems (CEPA, 1996). NEB report (NEB, 1996) summarized these failures in Figure 2-2.
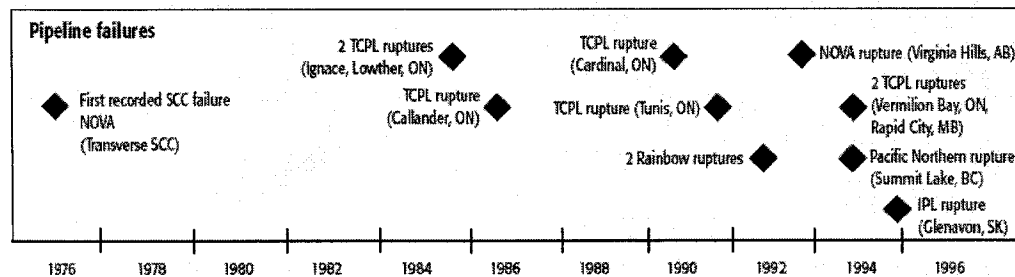
Figure 2-2 Chronology of near-neutral pH SCC events in Canada

(From NEB report, 1996)

From the above figure, the annual occurrence of SCC failures reached as high as four failures in 1990. But from the five-year rolling historical average data from 1989 to 1995, the failure number increased from one failure per year to two failures per year. In 1999, a large pipeline rupture occurred on a 42-inch pipeline in southwestern Alberta. In 2001, a 34-inch oil pipeline of Enbridge failed in central Alberta and about 24,000 bbls of heavy crude oil was released into a frozen slough.

Actually, near-neutral pH SCC has not only happened in Canada but also in many other countries. It was reported that the average incident rate is almost as likely to occur on a gas transmission pipeline within the United States as in Canada (Hall and McMahon, 1999), even though most of these failures were caused by high pH SCC (CEPA, 1996). Although SCC failures on hazardous liquid pipelines in United States have been less frequent when compared with SCC occurrences on natural gas pipelines, three failures of hazardous liquid pipelines during 2003 were attributed to SCC (Baker, 2005). Outside of North America, the former Soviet Union has a similar

5

pipeline failure history caused by near-neutral pH SCC as that in Canada. Further more, SCC affected the following countries Australia, Iran, Iraq, Italy, Pakistan and Saudi Arabia. (CEPA, 1996)

2.1.2 Costs associated with failures

For a pipeline failure, the direct costs include the cost of pipeline repair, property restoration and product lost during pipeline failure etc. The average direct cost of a rupture on a large diameter natural gas pipeline is approximately $1.5 million; for a leak, it is about $150,000.00 (NEB report, 1996)

The indirect costs may include the impacts on the affected communities, loss of system throughput, potential loss of the energy market and addressing concerns over the reliability of the pipeline systems. The worst thing is threat to human life.

Because of the sudden, often unexpected and serious nature of SCC, there is an urgent need for the problem to be controlled. The understanding of the characteristics, the fundamental controlling factors and the mechanisms of near-neutral pH SCC is likely to result in more reliable and practical approaches to this problem.

2.2 Characteristics and controlling factors

Near-neutral pH SCC on pipelines begins when small cracks develop on the outside surface of the buried pipelines. Over a period of years, these individual cracks may lengthen and deepen and the cracks within a colony may join together to form much longer cracks (Jones, 1992). When a crack becomes large enough without penetrating the pipe wall, for the steels with low fracture toughness, the fracture toughness may be exceeded and the resulting fast fracture can propagate for a considerable distance beyond the initial crack. For a steel with high fracture toughness, the failure may involve plastic collapse, a leak occurs (Parkins, 2000)

When describing the characteristics of near-neutral pH SCC, it is customary to

6

compare to high pH SCC. Morphological similarities between high pH SCC and near-neutral pH SCC include both the presence of a large number of colonies of longitudinal cracks linked up to form long shallow cracks which have high aspect ratios (crack length over crack depth) on the outside surface of the affected pipelines and the presence of magnetite and iron carbonate films on the crack surface (Harle et al., 1994, Brongers et al., 2000)

The most obvious identifying characteristic of near-neutral pH SCC in pipelines, regardless of pH (5.5~7.5) value, is the appearance of patches or colonies of parallel cracks on the external surface of the pipeline. There may be several of these colonies on a single joint of pipe and many joints of pipe may be involved. The cracks tend to concentrate near longitudinal welds and the crack densities in localized regions are very high. They are closely spaced and of varying length and depth. These cracks may coalesce to form larger and longer cracks, which in some cases can lead to rupture. If the cracks are sparsely spaced, they might grow through the wall and cause a leak, before they reach a critical length that is sufficient to cause a rupture.

2.2.1 Fracture mode and crack morphology

Compared to high pH SCC, near-neutral pH SCC is characterized by predominately transgranular (TG) cracks, as shown in Figure 2-3, and has cleavage or quasi-cleavage fracture features.

7
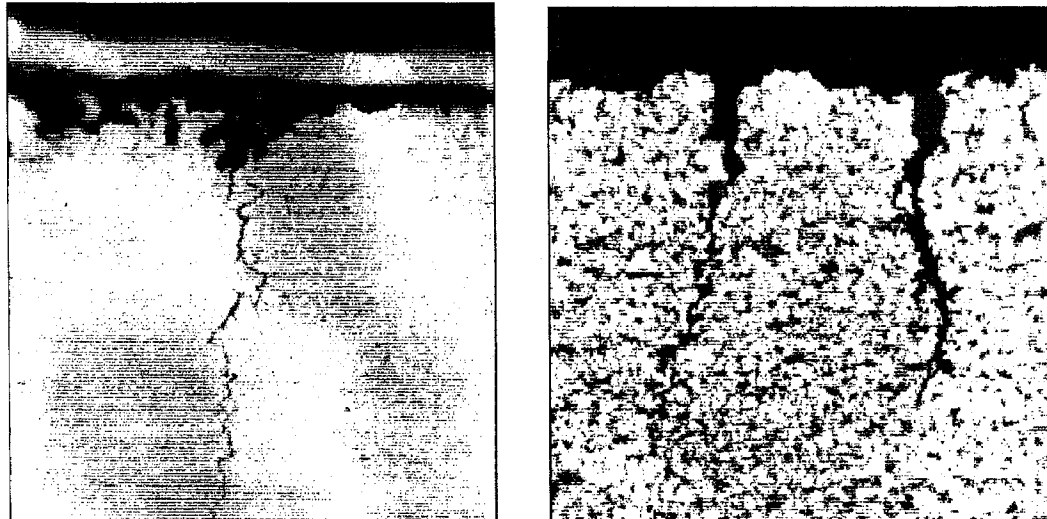
Figure 2-3 Crack growth paths of high pH SCC and near-neutral pH SCC (a) metallographic section of high pH SCC (b) metallographic section of near-neutral pH SCC (From Jones, 1992)

The cracks grow across or through the grains, the sidewalls of the cracks corrode and the cracks appear much wider with appreciable amounts of loosely adherent corrosion products forming in the crack enclaves than is the case with high-pH SCC cracks where the crack sides show little evidence of lateral corrosion, i.e. the opposite sides of the high pH SCC crack match very closely (Parkins, 2000). Near the crack tip, for near-neutral pH SCC crack, little lateral dissolution will have occurred; with the crack becoming narrower, and hence the TG path can be established with certainty only near the crack tip Another feature is that the cracks are filled with corrosion product, and a large amount of white iron carbonate is formed between the coating and pipe surface.

2.2.2 Electrochemical behavior

The electrolyte found under disbonded coating is a very dilute carbonate-bicarbonate solution containing small quantities of chloride and sulfate and also a relatively thick, white deposit of iron carbonate forms under the coating near the cracking region (Chen et al., 2002). The pH of the soil solution at the cracking region of pipeline steel is around 5.5~7.5. It should be noted that "pH" refers to the environment on the pipe

surface at the crack location and not the soil pH. The concentration of bicarbonate-carbonate in near-neutral pH environment is much lower than for the high pH case, only about 0.01 mol/L.

The main anodic reaction is written as Equation 2-1:

$$Fe \rightarrow Fe^{2+} + 2e^-$$ ---2-1

The CO_2 content in the vicinity of pipeline is very important, it helps to maintain the anaerobic condition. Under anaerobic soil environment, when CO_2 penetrates the soil and arrives at the pipe surface, because with the same pH, H_2CO_3 is more corrosive than HCO_3^-, CO_2 could promote the following reaction by increasing the concentration of carbonic acid.

$$CO_2 + H_2O \rightarrow H_2CO_3$$ ------------------------------2-2

From the relative concentrations of the three carbonate species, as shown in Figure 2-4, as pH range varies from 5.5 to 7.5, the main species are HCO_3^- and H_2CO_3, the proportion of them is in the range of 0.13~0.95. So, there are a number of possible cathodic reactions, including:

$$2H^+(aq) + 2e^- \rightarrow H_2$$ -------------------------------------2-3

$$2H_2O + 2e^- \rightarrow H_2 + 2OH^-$$ --------------------------------2-4

$$2H_2CO_3(aq) + 2e^- \rightarrow H_2 + 2HCO_3^-(aq)$$ --------------2-5

$$2HCO_3^-(aq) + 2e^- \rightarrow H_2 + 2CO_3^{2-}(aq)$$ ----------------2-6
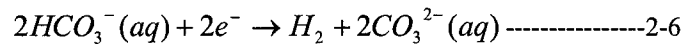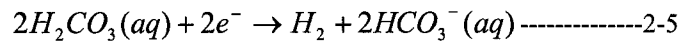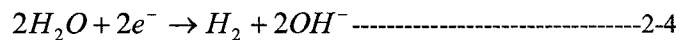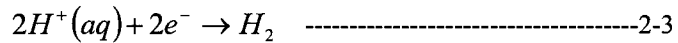
The species, HCO_3^- and H_2CO_3, will dissociate in the solution to provide H^+, so that Equation 2-3 was assumed to be the sole cathodic reaction.

9
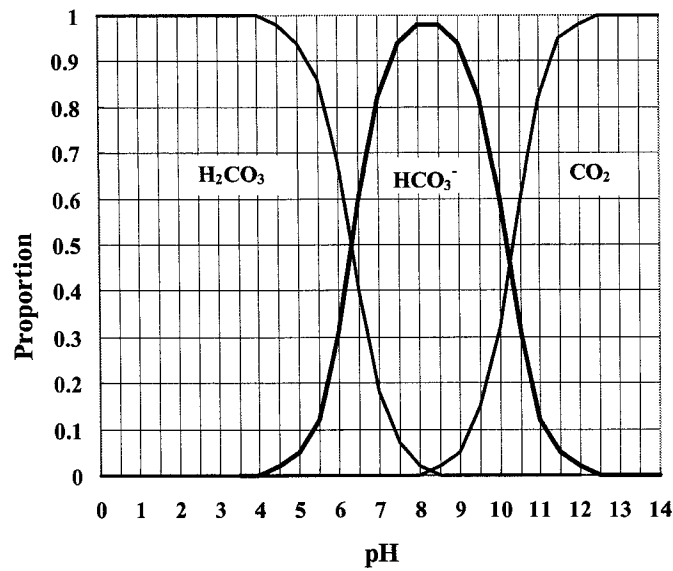
Figure 2-4 Relative concentrations of the three carbonate species in the pH range of 0 to 14

When a potentiodynamic scan is made of steel exposed to near-neutral pH soil solution, there is no passive zone in the polarization curve, and the open circuit potential (OCP) is around $-760\sim-790$ mV$_{SCE}$ (Parkins, 1994).

The differences between high pH SCC and near-neutral pH SCC of pipeline steels are summarized in Table 2-1, which implies different mechanisms of cracking. And also, Figure 2-5, Potential-pH diagram shows the regimes for intergranular SCC and transgranular SCC (Parkins, 2000)

Table 2-1 Comparison between high-pH SCC and near-neutral pH SCC

(Wilmott and Diakow, 1996)

Factors	High-pH SCC	Near-neutral pH SCC
Bicarbonate-carbonate	High, about 1mol/L	Low, about 0.01mol/L
pH value	Around 9.5 (high pH), ≥ 9.3	Around 6.5 (low pH), 5.5~7.5
Temperature sensitivity	Rate increases exponentially	Without

10

	with temperature	
Environmental characteristics	No correlation has been found between the incidence of SCC and soil characteristics close to cracked pipelines.	The CO_2 content in the vicinity of pipeline is important: more CO_2 gives higher cracking rate
Cathodic Potential (Parkins et al., 1994)	-0.60~-0.83 V_{CCS} or –0.52~-0.75 V_{SCE} more positive than E_{corr} more prevalent at higher temperature	At E_{corr} (-0.76~-0.79 V_{CCS} or –0.68~-0.71 V_{SCE}) or slightly cathodic (max.-0.05V) under disbonded coating that shields CP
Association with welds	Without association	Tend to be concentrated near longitudinal welds
Associated reactions and products	Very small amount of iron carbonate is incorporated in the thin magnetite films	Large amount of white iron carbonate is formed between the coating and pipe surface
Cracks	Intergranular, narrow, spaced more widely and with no evidence for corrosion of crack wall. The films are strongly adhered to the crack sides and effectively prevent any lateral dissolution on the sides, IG and TG path can be established.	Transgranular, with very high densities, with wide cracks filled with corrosion product. Significant lateral dissolution occurs, with appreciable amount of loosely adherent corrosion products forming in the crack enclaves. TG path can be established with certainty only near the crack tip
Polarization curve	With active to passive transition	Without passive zone

Potential Vsce

-0.2 -0.4 -0.6 -0.8

Relatively concentrated solutions
containing Na2CO3, NaHCO2 and
CO2 in various proportions

IGSCC

Reduction of hydrogen

Trans. SCC
Dilute solutions
containing HCO3-,Cl-, SO4^2- with
various amount of CO2

5   7   9   11

pH
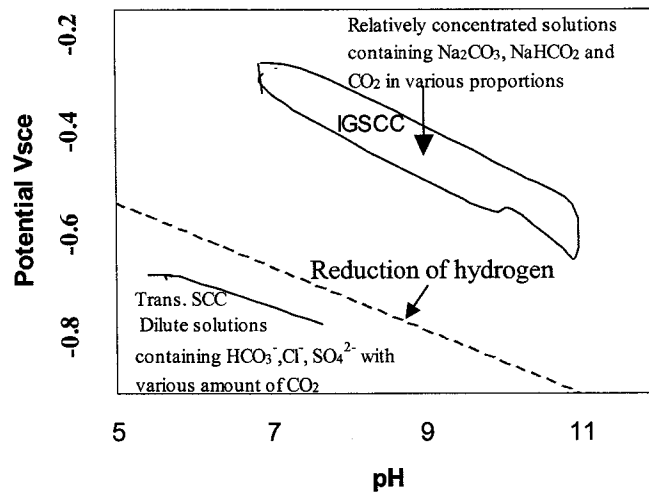
Figure 2-5 Potential-pH diagram showing the regimes for intergranular and trangranular SCC at 24°C in solutions containing different amounts of CO_3^{2-}, HCO_3^- and CO_2 to achieve different pH values (From Parkins, 2000).

2.2.3 Two types cracking in pipeline steel

The great majority of SCC cracking in the Canadian system is usually oriented longitudinally (Zheng et al., 2000), and is called longitudinal cracking or axial cracking. This kind of cracking is driven by the hoop stress which is usually the dominant stress component resulting from the internal pressure of the pipeline and the longitudinal cracks always link up to form long shallow flaws, with length to depth ratios that are typically in the range of 50-200 (Jaske and Beavers, 1998)

However, SCC may also occur in the circumferential direction, termed circumferential cracking (C-SCC) when the predominant stress is an axial stress. Incidents resulting from C-SCC have been reported due to stresses induced by soil creep and localized bending from ground movements, and rock dents; Residual stresses at girth welds may also produce a resultant axial load within a pipeline (Baker, 2005). A few leaks have been found in Italy with the characteristics of being all circumferential cracks (Arrigoni and Sinigaglia, 1999).

12

Figure 2-6 shows these two kinds of cracks (NEB report, 1996). Usually, longitudinal cracking can result in large failure, while the circumferential cracking only results in small leaks. Failure by circumferential SCC has been a rare event (Sutherby, 1998). Therefore, most research has been focused on longitudinal cracks.
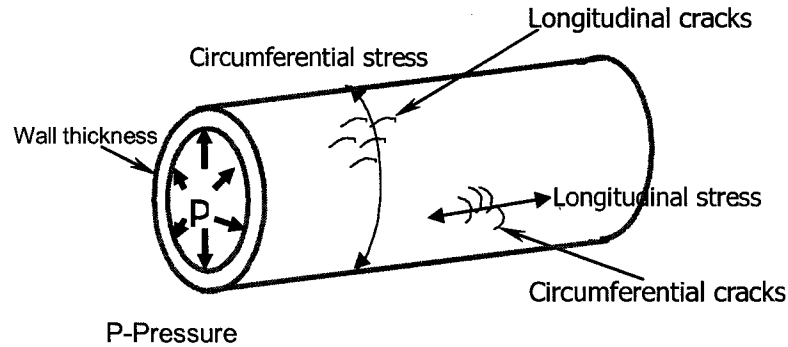
Figure 2-6 Stresses and cracks in pipeline steel (From NEB report, 1996)

2.2.4 Conditions for near-neutral pH SCC

Near-neutral pH SCC happens when the necessary electrochemical, adequate mechanical and metallurgical conditions exist (NEB report, 1996). The important electrochemical parameters include electrochemical potential, pH, impurity concentration and temperature; the important mechanical parameters include stress, stress intensity and strain rate; the significant metallurgical factors include localized microchemistry, bulk composition, deformation character, and yield strength (Jones, 1992).

2.2.4.1 Corrosive environment at the pipe surface

Among all the controlling factors, a prerequisite for crack initiation is that an appropriate environment has come into contact with the pipe surface (Chen et al., 2002). This appropriate environment can only develop after the damage or disbondment of the pipe coating and in the absence of the cathodic current, which is used to control corrosion. SCC has been found in environments with low concentrations of carbonic acid and bicarbonate ions with the presence of other

13

species including chloride, sulfate and nitride ions.

Parkins pointed out those sulfate-reducing bacteria (SRB) have been identified as possible contributory factor to near-neutral pH SCC (Parkins, 1988). An anaerobic soil solution is necessary to create the near-neutral pH SCC environment. In anaerobic soil conditions, SRB may form and reduce sulphate in the soil to sulphide. When water reaches the pipe surface and the corrosion reaction begins, atomic hydrogen is created. The sulfide is a poison to prevent the atomic hydrogen from forming molecular hydrogen. The molecular hydrogen would not be able to penetrate the pipe and would leave the pipe surface, but the atomic hydrogen can penetrate the pipe, it can cause hydrogen embrittlement at the tip of the crack, assisting crack propagation.

Parkins also suggested that carbon dioxide (CO_2) is a possible contributory factor to near-neutral pH SCC (Parkins, 1998). It was described by Johnson et al. and Gu et al. (Johnson et al., 2000, Gu et al., 1999 (2)) that with increasing levels of CO_2, the local corrosion of pipeline steel increases, which will make the crack growth increase during cyclic growth tests. In near-neutral pH soil environment, H_2CO_3 and HCO_3^- are the main species and HCO_3^- concentration is normally about 1000 times larger than CO_3^{2-} concentration. With increasing concentrations of CO_2, the concentration of HCO_3^- increases, and the crack growth rate increases (Parkins, 1998). This means that the HCO_3^- species may play an important role on active crack tips.

Several researchers (Gu et al., 1999 (2), Chen et al., 2002 (2)) showed that the SCC susceptibility did not vary significantly with different concentration of Cl^- ions.

In laboratory testing, cathodic polarization increased the susceptibility to near-neutral pH SCC, possibly by inhibiting general corrosion, which otherwise dissolved the crack initiation pits or defects from the sample surface, or by increasing the hydrogen concentration which promoted hydrogen-assisted crack initiation or propagation (Chen et al., 2002). Rebak et al. (Rebak et al., 1995) found the susceptibility of

14

near-neutral pH SCC was minimum at corrosion potential (E_{corr}), it would increase if the cathodic potential increased. Field experience indicates that if the cathodic protection system provides adequate protection potentials and the coating does not shield the cathodic protection current, the soil electrolyte will have an elevated pH and near-neutral pH SCC will not occur (Beavers et. al, 1998). Chen also got the same conclusion that in the field, cathodic polarization decreases the susceptibility to near-neutral pH SCC by increasing the pH value at the pipe surface to values greater than 7.5 (Chen et al., 2002).

At anodic potential, the SCC susceptibility decreases when the anodic dissolution current is high enough, which will cause general corrosion, dissolving the crack initiation nuclei (Rebak et al., 1995, Gu et al., 1999 (2))

Near-neutral pH SCC appears to occur more frequently in the colder climates. Beavers said at lower temperature, the solubility of CO_2 increases, so the concentration of CO_2 increases, which forms carbonic acid environment, near-neutral pH SCC can occur easily (CEPA report, 1996). However, Parkins pointed out that the crack growth rate is not sensitive to the temperature change at much higher temperatures, the SSR tests show no significant difference for crack growth rate at temperature of 5°C and 45°C (Parkins et al., 1994).

Furthermore, Chen (Chen et al., 2002) found that for different soil solutions, the relative susceptibility to near-neutral pH SCC was determined by the pH values of the soil electrolytes bubbled with a given CO_2/N_2 gas mixture, the soil electrolyte with the higher pH value (up to ~7) is more conducive to near-neutral pH SCC; for a given soil solution, the actual level of CO_2 in the soil electrolyte determines the SCC intensity: the higher level of CO_2, the more susceptible to near-neutral pH SCC.

15

2.2.4.2 Adequate mechanical condition

Compared to high pH SCC, more restricted mechanical loading conditions, cyclic or dynamic loading, are required for near-neutral pH SCC to occur (Beavers and Harle, 1996). In laboratory tests, stress fluctuation, even minor, is required for crack initiation and propagation (Beavers and Hagerdorn, 1996, Plumtree et al., 1999 and Zheng et al., 1997).

Zheng et al. (Zheng et al., 2000) found that when steel is stressed close to its yield point in a susceptible environment, cracks may develop with very minor pressure fluctuation. The SCC initiation lifetime increases with decreasing applied stress, the relationship between the SCC lifetime t_i and the applied stress σ can be expressed as t_i $=\alpha$ $(\sigma_{max}/SMYS)^{-\beta}$, (SMYS=Specified minimum yield strength) (Lu et al., 2002), where σ_{max} is the applied stress level, α and β (≥ 0) are both experimental constants. And also, the SCC crack initiation rate increases with increasing applied stress level (Lu et al., 2002).

For small, shallow surface SCC cracks, the growth rates are independent of applied stress in the range of 40% to 100% SMYS (Wilmott and Sutherby, 1998). This indicates that the absolute loading level has no effect on the early stage of crack propagation (Lu et al., 2002). It is different from the general consideration that as the stress increases, the plastic deformation increases, and more hydrogen enters the crack tip, hydrogen assisted cracking (HAC) will increase, and so crack growth rate will increase (Parkins et al., 1994). They pointed out the reason is that in the early stage of SCC growth, the dominant mechanical driving force may be due to some stress other than hoop stress, such as residual stresses at the pipe wall surface, so the rate is independent of the applied load. Until a certain crack size has been reached where more macro stresses, such as hoop stress, would take over. After that, SCC propagation rates increase as the applied stress increases because the loading conditions control the sharpness of cracks (Wang et al., 1999). And also, for near-neutral pH SCC, the slower frequencies of cyclic loading give larger per-cycle

16

growth rates. Because at low frequency, there is more time for the environment to interact with the crack, which increases the growth rate. However this is only true when the frequency is down to about 0.0001 Hz because at really low rates the cracking may go dormant.

The results of variable amplitude stress conditions conducted at two-stress levels showed that the crack growth accelerates on subsequent cycles following an under-loading. The crack growth is more severe when the under-loads are distributed evenly throughout the load history compared to when they are grouped together in blocks (Williams, 2004).

2.2.4.3 Susceptible metallurgical condition

Near-neutral pH SCC failures occurred on pipelines in which diameters ranged from 114 to 1067 mm, wall thicknesses ranged from 3.2 to 9.4 mm and grades varied from 241 MPa to 448 MPa (NEB report, 1996). The pipe manufacturing process, type of steel, grade of steel, cleanliness, composition of steel, plastic deformation characteristics of the steel, steel working temperature and pipe condition of the steel are all factors affecting the susceptibility of the pipeline to near-neutral pH SCC.

In the laboratory, various grade pipeline steels have been used for SCC investigations, such as X-52, X-60, X-65, X-70 and X-80 etc (Chen et al., 2000, Qiao et al., 1997, Yu et al., 1999, Wang et al., 1999). Normally, X-52, X-60 and X-65 steels are composed of ferrite+ pearlite while X-70, X-80 and X-100 steels have a fine-grained acicular and /or bainitic ferrite microstructure (Parkins, 2000, Misra et al., 2000) because of the advances in alloy design technique and adoption of new controlled-rolling processes. Steels with more uniform microstructures were observed to be less susceptible to SCC when compared with steels containing inhomogeneous microstructures (Kushida et al., 2001), furthermore, Lu and Luo found (Lu and Luo, 2004) that the steels with a microstructure of fine-grained bainite+ ferrite have a better combination of strength and SCC resistance than those with ferrite+ pearlite

17

structures. This means that the higher the grade of the steel, the higher the SCC resistance and also they pointed out that the increase in pearlite content in the microstructures had a detrimental effect on the SCC performance. However, it is believed that even among steels that have similar compositions and microstructures, certain batches of pipeline steel have been found to be much more susceptible to SCC than other batches. The suggested explanation is that the other characteristics of the steel, such as creep response to cyclic loading, maybe be important (Beavers and Harper, 2004, Baker, 2005.).

The coarse-grained heat-affected zone is more susceptible to cracking than the base material in the near-neutral pH environment (Beavers, 1996) and a significant portion of SCC failures has been associated with the welds (Zheng et al., 2000). It was found that the original intact pipeline surface is more conducive to cracking than the polished surface (Wang et al., 1999, Lu et al., 2002))

2.3 Mechanisms of crack initiation and propagation

Research into near-neutral pH SCC has been in progress for about twenty years, but the way in which near-neutral pH SCC initiates and then propagates is not yet completely understood. To date, it is broadly accepted that dissolved hydrogen and anodic dissolution are the two main factors contributing to near-neutral pH SCC (Parkins et al., 1994, Qiao et al., 1997, Lu et al., 2002)

In the past, a large amount of research effort was devoted to the effect of hydrogen ingress and anodic dissolution on the crack propagation process (Parkins et al., 1994, Parkins, 2000, Liberto and Gabetta, 1997 and Mao et al., 2001) while less attention has been put on their effects during crack initiation which comprises the major part of service of pipeline steel (Parkins et al., 1994, Parkins, 2000). Lu and Luo (Lu and Luo, 2005) found that both dissolved hydrogen and anodic dissolution can promote crack initiation. However, if the anodic current density is too high, the potential crack nuclei will dissolve resulting in the retarding of crack initiation. And also, it is well known

18

that crack advance during transgranular SCC is discontinuous, crack advance can be considered as a re-initiation process (Lian and Meletis, 1996). All of these make the study of crack initiation process much more important.

2.3.1 Factors controlling SCC initiation

The research on near-neutral pH SCC initiation and early propagation behavior of pipeline steel is limited (Parkins, 2000), although these processes occupy the major part of the service lifetime of pipelines (NEB report, 1996). From the results of Wang et al. (Wang et al., 1999), there are three types of crack initiation sites: the surface depression regions where the majority of cracks are located; pre-existing crack-like defects at which cracks develop and the non-metallic inclusions, which develop into pits.

Crack initiation can be divided into two types, pit cracks and non-pit cracks (Lu et al., 2002). Non-pit cracks are more likely to initiate at the locations with localized plastic deformation (Lu et al., 2002) when a certain amplitude of stress fluctuation and a substantial number of load cycles are applied (Wang et al., 1999); pit cracks initiate at the most favorable crack initiation pitting sites where there is a dissolution of /around non-metallic inclusions (Elboujdaini et al., 2000(1), Elboujdaini et al., 2000(2) and Lu et al., 2002) and this produces a stress concentration and the local electrochemical conditions to promote crack initiation.

Several factors have been identified that affect SCC initiation, such as applied stress level, chemical composition, microstructure and yield strength of the steels, although a definitive mechanism of SCC initiation is still not available.

Crack initiation was found to be a competitive process in which cracks formed first at the most favorable sites and then at the less favorable sites (Wang et al., 1999). Reducing the content of non-metallic inclusions in the microstructure can increase the crack initiation life of pipeline steel to near-neutral pH SCC (Lu et al., 2002). Parkins

19

et al. (Parkins et al., 1994) investigated the surface conditions effect on the near-neutral pH SCC process and found corrosion cracks are more readily to initiate from the side with the original intact pipe surface than the polished surface on the opposite side of X-65 pipeline steel sample. Removing the local surface discontinuities can also increase the crack initiation life by affecting the stress amplitude and the number of load cycles required for crack initiation (Wang et al., 1999).

Lu et al. (Lu et al., 2002) conducted a SCC test with dog-bone type samples of X-70 pipeline steel, the maximum stress applied was 1.05 SMYS (specified minimum yield stress) and a stress ratio $R=\sigma_{min}/\sigma_{max}=0.5$. The results (as shown in Figures 2-7 and 2-8) indicated that with increasing applied stress level, the crack initiation rate increased and the SCC initiation life of X-70 pipeline steel decreased.
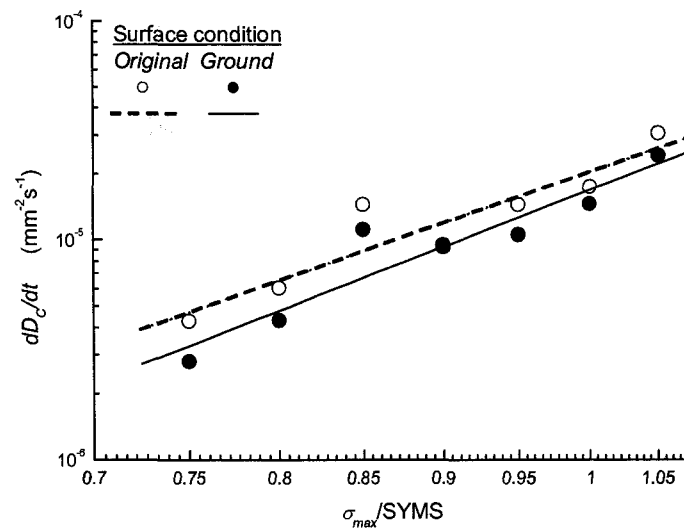
Figure 2-7 Stress-dependence of crack initiation time (From Lu et al., 2002)

20
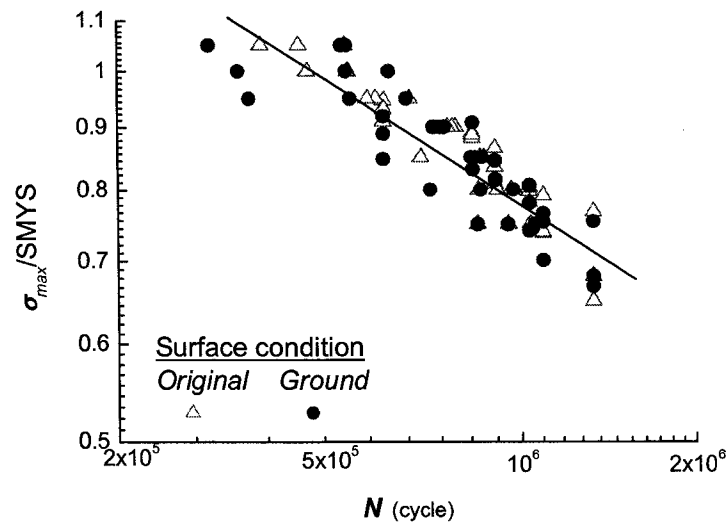
Figure 2-8 SCC initiation life curves of X-70 steel (From Lu et al., 2002)

Frost et al. (Frost et al., 1974) pointed out that the stress needed to initiate plastic deformation at the surface layer of the pipe is lower than that needed in the bulk material, so SCC can be initiated at stress levels well below the bulk yield strength of the steels. And also, decreasing the frequency of cyclic loading applied to pipeline steels, which will give more time for the environment to interact with the potential crack initiation site, and will also decrease the crack initiation life by the contribution of pitting to crack initiation (Lu et al., 2002).

From the NEB report (NEB report, 1996), higher strength steels may be more susceptible to near-neutral pH SCC since plasticity on the pipe surface is the primary factor that causes SCC initiation. The controlled rolling process and precipitation hardening in high grade steel is likely to cause an increase in dislocation density, this will give a noticeable drop in ductility when moving to higher strength steel. (Vadhwana and Chen, 2002). With the improved tensile properties, the ductility of the steel would decrease which will make crack initiation easier.

21

2.3.2 Mechanisms of SCC propagation

After initiation, the cracks may extend by growing in both longitudinal and thickness directions, which could lead to coalescence of the most closely spaced cracks. The coalescence would make the cracks grow more quickly and eventually lead to failure.

As mentioned before, the anodic dissolution and ingress of hydrogen are the two fundamental factors contributing to near-neutral pH SCC (Parkins, 1994, Gu et al., 1999).

2.3.2.1 Anodic dissolution

It is clear from the observed nature of the cracks that corrosion occurs not only at the crack tip but also on the crack wall. And also, Bulger (Bulger, 2000) presented a linear relationship between the SCC resistance and polarization resistance of X-70 steel under various heat treatment conditions. This implies that anodic dissolution may play a key role in the near-neutral pH SCC process of pipeline steel.

But it is doubtful that growth can be explained entirely in terms of a dissolution process, because at high stress or strains level, the observed growth rates are markedly greater than that can be accounted for by rates of dissolution in near-neutral pH environments. Many other researchers (Ahmed et al., 1997, Wilmot and Sutherby, 1998, Zhang et al., 1999, Brongers et al., 2000 and Parkins, 2000) used various specimens for crack propagation evaluation; the maximum crack growth rate is estimated to be in the order of 10^{-6} mm/s. It is much larger than the maximum crack growth rate from dissolution acting alone.

2.3.2.2 Hydrogen assisted cracking

Hydrogen facilitates crack growth by promoting reduced ductility. There are two pieces of evidence (NEB report, 1996) in support of hydrogen playing a role in the overall growth process, however this evidence is circumstantial rather than direct. Firstly, the fracture surface invariably displays areas of quasi-cleavage, which is often

22

associated with hydrogen-induced cracking. A further indication of the entry of hydrogen into the steel is the secondary cracks that are not connected to the outer surface of the sample and which are nucleated on bands of pearlitic material. These cannot be formed by anodic dissolution.

Ahmed et al. (Ahmed et al., 1997) showed that near-neutral pH SCC is related to hydrogen-assisted cracking, which is exacerbated by the presence of MnS acting as a hydrogen source as well as a trap. It facilitates the entry of hydrogen into the metal by poisoning the recombination reaction of atomic hydrogen.

In the absence of significant cathodic protection current reaching the pipe surface, the pipe surface will be at open circuit potential and the discharge of hydrogen will require a balancing anodic reaction, indicated by dissolution on the crack sides (Parkins, 1994). In addition, Yu et al. and Scott et al. have suggested that the mechanism of near-neutral pH SCC was possibly dominated by hydrogen facilitated anodic dissolution at anodic potential and near the corrosion potential because at these potentials, local dissolution or pitting occur first, generating H^+ which results in local acidification within individual pits. This acidification could facilitate some corrosion reactions and increase both the crack initiation and propagation. At cathodic potentials, the cracking might be controlled by a hydrogen-induced cracking (HIC) mechanism when hydrogen concentration reached a critical value (Yu et al., 1999, Scott et al., 1998, Gu et al., 1999 (2)).

2.4 Plastic deformation of metal materials

When sufficient load is applied to a metal, it will cause the metal to change shape. This change in shape is called deformation. A temporary shape change is called elastic deformation. In other words, elastic deformation is a change in shape of a material at low stress that is recoverable after the stress is removed. This type of deformation involves stretching of the bonds, but the atoms do not slip past each other.

23

When the stress is sufficient to permanently deform the metal, it is called plastic deformation. On a microscopic scale, plastic deformation corresponds to the net movement of large numbers of atoms in response to an applied stress. During this process, from an atomic perspective, plastic deformation corresponds to the breaking of bonds with original atom neighbors and then reforming bonds with new neighbors as large number of atoms move relative to one another; upon removal of the stress they do not return to their original positions.

2.4.1 Tensile properties

For most metallic materials, elastic deformation persists only to strains of about 0.005 (Callister, 2002). As the material is deformed beyond this point, termed the yielding point, plastic deformation occurs. The yield strength can be determined by the 0.002 strain offset method (Callister, 2002).

Plastic deformation involves the breaking of a limited number of atomic bonds by the movement of dislocations. However, the movement of dislocations allows atoms in crystal planes to slip past one another at much low stress levels. Since the energy required for moving dislocations is lowest along the densest planes of atoms, dislocations have a preferred direction of travel within a grain of the material. This results in slip that occurs along parallel planes within the grain. These parallel slip planes group together to form slip bands, which can be seen with an optical microscope. A slip band appears as a single line under the microscope, but it is in fact made up of closely spaced parallel slip planes as shown in the image of Figure 2-9.

24
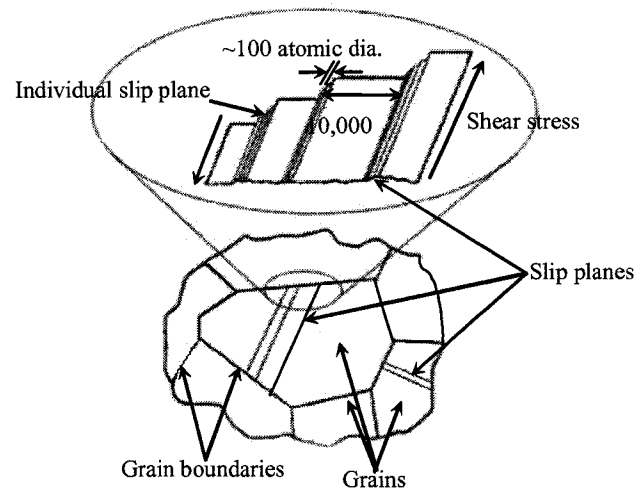
Figure 2-9 Slip plane of plastic deformed metal

Ductility is commonly defined as the ability of a material to plastically deform easily upon the application of a tensile load or as the ability of a material to withstand plastic deformation without rupture.

The yield strength and ductility of many metals can change if the conditions are altered.

2.4.2 Strain hardening effect

The strain hardening effect is shown in the following figure. Upon release of the load during the stress-strain process, some fraction of the total deformation is recovered as elastic strain, the magnitude of this elastic strain corresponds to the strain recovery, as shown in Figure 2-10. And also the unloading curve traces a nearly straight-line path from the point D of unloading. If the load is reapplied, the curve will traverse essentially the same linear portion in the direction opposite to unloading, yielding will again occur at the stress level where the unloading began. The whole process is illustrated in Figure 2-10.
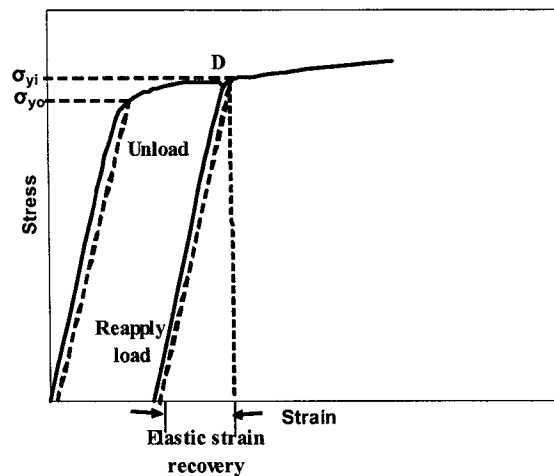
Figure 2-10 Schematic tensile stress-strain diagrams showing the phenomena of elastic strain recovery and strain hardening. The initial yield strength is designated as σ_{yo}, σ_{yi} is the yield strength after releasing the load at point D, and then upon reloading (From Callister, 2002).

Cold work is performed in a temperature region and over a time interval to obtain plastic deformation, but not relieving the strain hardening. It tends to make metals much stronger and less ductile.

The dislocation density in a metal increases with cold work due to dislocation multiplication or the formation of new dislocations. Consequently, the dislocations are positioned closer together, the average distance of separation between dislocations decreases. On average, dislocation-dislocation strain interactions are repulsive. The net result of this repulsive effect is the motion of dislocation is counteracted by the presence of other dislocations. As the dislocation density increases with cold work, the resistance of dislocation motion by the presence of the other dislocations becomes more pronounced. Therefore, the applied stress needed to deform a metal, increases. This means that the yield stress of the metal increases with increasing cold work. The influence of cold work on the stress-strain behavior of steel is vividly portrayed in Figure 2-11.

26
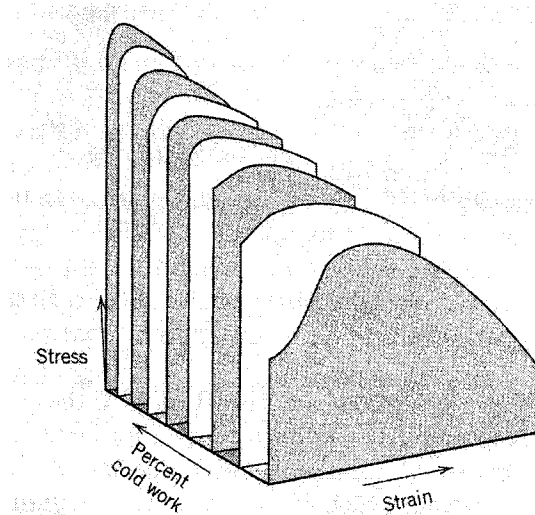
Figure 2-11 Influence of cold work on the stress-strain behavior for a low carbon steel (Bardes, 1978).

From the mathematical expression relating true stress and true strain

$$\sigma_T = K\varepsilon_T^n \quad \text{------------------------------------2-7}$$

where K and n are constants varying from alloy to alloy and also depending on the condition of material, the parameter n is often termed the strain hardening exponent, which has a value less than unity and is a measure of the ability of a metal to strain hardening; the larger its magnitude, the greater the strain hardening for a given amount of plastic strain.

Strain hardening is often utilized commercially to enhance the mechanical properties of metals during fabrication procedures. This effect may be removed by an annealing heat treatment. The heating of a cold-worked metal to or above the temperature at which metal atoms return to their equilibrium positions will increase the ductility of the metal.

2.5 The relationship between cold work and SCC susceptibility

Based on the fact that the ingress of hydrogen and anodic dissolution are involved in the cracking process, much research work was conducted on the effect of cold work

27

on dissolved hydrogen in steel and anodic dissolution during SCC process.

Vadhwana and Chen (Vadhwana and Chen, 2002) measured the diffusible and trapped hydrogen contents of different samples (X-65, X-80, X100) after experiencing various mechanical loading conditions and hydrogen precharging. They concluded that pre-plastic strain increases both the number of diffusible hydrogen atoms and the number of trapped hydrogen atom in all grades of pipeline steel, and also the highest amount of hydrogen was found in the highest grades of steel (X-100).

Rebak et al. conducted a constant load test using a notched non-fatigue pre-cracked sample of X-52 pipeline steel in deaerated NS4 soil solution at 50°C (Rebak et al., 1995). The crack growth rate for a non-cold worked sample could be estimated to be less than 5×10^{-9} mm/s. While other researchers have used fatigue pre-cracked samples, which have a cold work region at the tip of the pre-crack, the crack growth rates they got are much larger than 5×10^{-9} mm/s (Urednicek et al., 1992, Harle and Beavers, 1993, Szklarska-Smialowska et al., 1994, Parkins et al., 1994). Based on these facts, Rebak et al. (Rebak et al., 1995) pointed out that in the cold work regions, the material was especially predisposed to cracking. After the crack passed through the preexisting cold work region, cracking would stop. They concluded that cold work and localized strain are accelerating factors for SCC.

In the field, pipeline steels experience significant cyclic loading, which might cause some plastic deformation before the pipe material is exposed to the groundwater upon deterioration of the coating. So Wang et al. (Wang et al., 2002) conducted a test to study the effect of pre-cyclic loading on the initiation of SCC in pipeline steels exposed to a near-neutral pH soil solution. Two grades of steels, X-80 and X-65, were loaded in air. For a single test, the maximum stress was kept constant and less than the yield stress of the material and the amplitude of the loading regime was changed with time. The results showed that pre-cyclic loading causes micro-crack initiation on pipeline steel surfaces during subsequent corrosion exposure under constant load and

28

cathodic polarization (η_c=50 mV) conditions. The formation of these micro-cracks was attributed to localized deformation, such as that from persistent slip bands. However, there were no such micro-cracks observed at OCP because of uniform surface corrosion.

To date, only a few investigations have dealt with the effect of plasticity on the dissolution process (Garz and Hafke, 1971, Gutman et al., 1996). Gutman used 316L stainless steel, which could manifest active and passive regions on potentiodynamic polarization curves in the electrolyte of 0.1 N Na_2SO_4+ 5% H_2SO_4. It showed an increase of dissolution current density as a function of plastic strain (Gutman et al., 1996). And also, Sahal et al. investigated the plastic strain effect on the dissolution process of polycrystalline nickel in H_2SO_4 solution and got the same conclusion that in the active region, the corrosion current density is higher for the strained material than for the unstrained one (Sahal et al., 2004).

Because of its complicated nature, the current understanding of the effect of cold work on the susceptibility to near-neutral pH SCC is still insufficient, particularly the influence of cold work on anodic dissolution in near-neutral pH environment, and also much more work should focus on giving direct evidence of the effect of cold work on crack propagation in pipeline steel.

2.6 Techniques for SCC investigation

In the field, cracking takes over 15 years to manifest (Rebak et al., 1995). This implies that either the crack growth rates are very low or the induction time of cracking is very long. However, to study the variables that control cracking, a crack has to be reproduced in a reasonable time. In order to accelerate near-neutral pH SCC, usually, a fatigue pre-cracked compact toughness (C-T) sample is used for accelerating SCC test and improving the experimental reproducibility. Modifying a simulated service environment and making it more aggressive can produce an environment that accelerates SCC. For example, changing solution pH and

29

concentration of the species in solution can promote SCC easily. In addition, more severe loading conditions, such as much larger applied stress, smaller R-ratio, and higher loading frequency, are commonly used.

2.6.1 Mechanical test methods

Mechanical tests include constant load tests, constant extension tests, cyclic loading tests and slow strain rate tests (SSRT). The last one is the most popular one used in SCC investigation.

The SSRT method was developed by Parkins and co-workers in 1960's (Humphries and Parkins, 1967), it is for accelerating the SCC process in laboratory testing by using a tensile sample exposed to more aggressive environmental conditions. The principal advantage of this type of test is the rapidity with which the SCC susceptibility of a particular alloy and environment can be assessed. The test always ends in sample fracture, and the fracture surface is examined and compared with the fracture surface obtained in air. In addition to its timesaving benefits, less scatter occurs in the test results.

The most significant variable in SSRT is the strain rate, if the strain rate is too high, ductile fracture will occur before the necessary corrosion reactions can take place. So it is necessary to use relatively low stain rates. The most severe strain rate must be determined for the alloy and environment system.

SSRT can be used to test a wide variety of product forms, including parts joined by welding; tests can be conducted in tensile stress, in bending, or with plain, notched, or pre-cracked samples.

For smooth samples, the strain rate at the onset of the test is clearly defined, but, once the cracks have initiated and grown, straining is likely to concentrate in the vicinity of the crack tip, and the effective strain rate is unknown. The effective strain rates are

30

likely to be much higher than that for the same deflection rate applied to plain samples. Notched or precracked samples can be used to restrict cracking to a given location; and these kind of samples can also be used to restrict load requirements where bending may offer an added benefit. The section thickness or diameter of such samples is relatively small, so the testing duration is short.

Based on year's experience, the material's susceptibility to SCC is generally expressed by comparing many parameters, for examples:

a), time to failure, often normalized with respect to the time to failure in inert environment (air), t_{SCC}/t_{air}, and the smaller the time ratio, the larger the SCC susceptibility.

b), percent of reduction in area (RA%), the ratio of reduction in area of material tested in SCC causing environment and in air, RA_{SCC}/RA_{air}, and the smaller the ratio, the larger the SCC susceptibility.

c), percent of elongation after completion of the test. It is often expressed in the form of the ratio of total plastic deformation in a given environment to that in air ($\varepsilon_{SCC}/\varepsilon_{air}$). The smaller the ratio of $\varepsilon_{SCC}/\varepsilon_{air}$, the larger SCC susceptibility.

2.6.2 Corrosion and Electrochemical tests

There are many kinds of corrosion test methods, including potentiodynamic polarization, linear polarization resistance, potentiostatic test and so on. In fact, although they cannot give direct information about the material's SCC behavior; at least some corrosion characteristics can be obtained and used to understand the contribution of corrosion to SCC.

2.6.2.1 Potentiodynamic polarization

For an electrochemical reaction, the anodic polarization current density is

$$i_A=i_{corr}[\exp(2.3\eta_A/\ b_A)-\exp(-2.3\eta_A/b_C)]\text{------------------------2-8}$$

The cathodic polarization current density is

$$i_C=i_{corr}[\exp(2.3\eta_C/b_C)-\exp(-2.3\eta_C/b_A)]\text{------------------------2-9}$$

31

where i_{corr} is the corrosion current, η_A and η_C are anodic and cathodic over-potential (the difference between the applied potential and corrosion potential), A and C are the anode and cathode.

The corrosion rate (corrosion current) can be obtained by the following methods:

a) Tafel linear extrapolation method

When the over-potential is larger than 50mV, the relationship between over-potential and the logarithm of polarization current density is linear:

$$\eta_A = - b_A \lg i_{corr} + b_A \lg i_A \quad \text{----------------------------- 2-10}$$

$$\eta_C = - b_C \lg i_{corr} + b_C \lg i_C \quad \text{----------------------------- 2-11}$$

The linear curves are called Tafel lines. b_A and b_C are the slopes of anodic and cathodic Tafel lines, where $b_A = 2.3RT/\beta nF$ and $b_C = 2.3RT/\alpha nF$

Corrosion potential and corrosion current density can be obtained by extrapolating both the anodic and cathodic Tafel lines.

There are some possible errors that need to be considered. Because the over-potential is large, the potential is far from the corrosion potential and interferes with the corrosion system; the current needed to enter the Tafel linear region is large, the surface status of the electrode, the real area of the electrode and the concentration of the surrounding solution will change a lot; and also at the larger current, the effect of solution resistance on the potential measurement will be significant and it will produce some error for the i_{corr} measurement.

b) Linear polarization resistance method

When the over-potential is less than 10mV, the relationship between over-potential and polarization current density is linear, the slope of the line is the polarization resistance R_P, $R_P = (d\eta_C/di_C)_{\eta \to 0} = (d\eta_A/di_A)_{\eta \to 0}$

32

The Stern formula gives the corrosion current density

$$i_{corr} = B/R_P \text{ ----------------------------------2-12}$$

where $B = b_A b_C/[2.3(b_A + b_C)]$

This is the general electrochemical method to get the corrosion current.

2.6.2.2 Weight loss method

Many researchers use weight loss test to determine the general corrosion rate. This method uses the following formula to calculate the corrosion rate according to the weight loss after corrosion process.

$$V = \Delta g/(S.t) \text{ ----------------------------------2-13}$$

Where Δg is the mass difference of the sample before and after the test, S is the surface area of the sample and t is the test time.

For uniform corrosion, the relationship between the corrosion rate and the corrosion current is:

$$V = Ai_{corr}/nF \text{ -------------------------------2-14}$$

A is the atomic weight of the metal, n is the number of electrons in the anodic reaction and F is the Faraday constant.

This method is good whenever the corrosion product can be removed easily from the surface. However if the corrosion product is attached to the sample tightly, the weight gain method could be used, and in such a case Δg in Equation 2-13 is the mass difference in gram of the sample after and before the test.

Because corrosion is a long-term phenomenon, long-term weight loss test is often used for measuring the corrosion rate.

2.6.3 SCC tests

The SCC tests are conducted on a material testing system under a cyclic loading condition. Because SCC is really a long-time process, in the laboratory test, accelerated methods are always used. Usually, the fatigue pre-cracked samples, more aggressive simulated service environments and more severe loading conditions are applied for the crack propagation test. But for crack initiation tests, only more aggressive environments and more severe loading conditions can be used.

2.6.3.1 Potential drop method

The potential drop method is often used to measure the crack propagation rate. Usually, a fatigue pre-cracked C-T sample, a much higher frequency and a more severe cyclic loading are applied on the sample in order to accelerate the test.

Figure 2-12 illustrates the potential drop method. This method relies on measuring changes in the potential field in a specimen as a consequence of geometric changes due to crack growth. it can be used to measure the accurate crack extension.
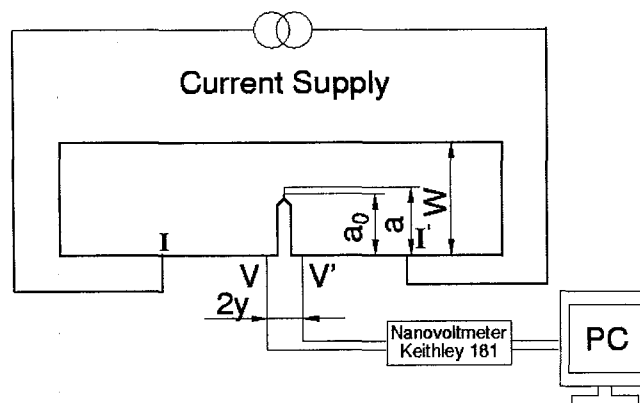
Figure 2-12 Schematic of potential drop method

At the points (I, I') a direct current is supplied during the sampling period. An increase in crack length produces an increase of the potential drop measured between the potential leads (V, V'). This can be used to compute the crack growth increment(a-a_0). In order to ensure that the potential change between the potential

34

leads is only the result of crack growth, the test environment is kept in an insulated chamber and a thermostat is used is keep the temperature constant.

2.6.3.2 Surface replicating method

A first class lever system was used in the cyclic loading frame for the surface replica test. The working principle of the first class lever is shown in Figure 2-13. A fulcrum is positioned between the *load* and the *effort*. The arm ratio from the loading side (*effort*) to the working side (*load*) is known. The loading side is being controlled by mechanically driven motor operated at specified frequency, which gives the working side a cyclic loading condition.
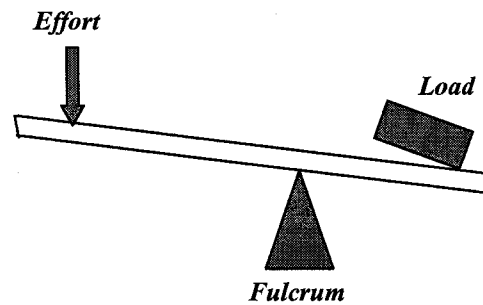
Figure 2-13 the principle of the cyclic loading frame

This kind of test can be conducted on the smooth (or notched) or pre-cracked samples to investigate crack initiation and crack propagation behavior respectively. The morphology of the crack can be recorded by replicating tape. By studying the changes with time, the crack initiation time, crack growth length, and crack growth rate can be obtained.

35

3 Experimental Details

3.1 Materials

X-52 low carbon steel was obtained from Enbridge and came from a line with a polyethylene tape coating that had experienced environmentally assisted cracking after thirty-four years of service. The pipe had an external diameter of 34" (864 mm) and had a measured thickness of 7.1 mm. The chemical composition of a typical heat is listed in table 3-1. The microstructure consisted of fine pearlite and ferrite with a grain size of 10 μm to 20 μm, as shown in Figure 3-1. The specified minimum yield strength (SMYS) was 390.0 MPa and the ultimate strength was 589 MPa.

Table 3-1 Chemical composition of the X-52 pipeline steel used in this study (wt. %)

Elements	X-52
C (Carbon)	0.261
Mn (Manganese)	1.150
P (Phosphorus)	0.008
S (Sulfur)	0.019
Si (Silicon)	0.036
Cu (Copper)	0.033
Sn (Tin)	0.002
Ni (Nickel)	0.032
Cr (Chromium)	0.027
Mo (Molybdenum)	0.013
Al (Aluminum)	0.002
V (Vanadium)	0.003
Nb (Niobium)	0.003
Ti (Titanium)	0.002
Co (Cobalt)	0.006
Fe (Iron)	Balance

36

Figure 3-1 Microstructure of X-52 pipeline steel

3.2 Test solution

The NS4 synthetic solution (Table 3-2) has been widely used to simulate the soil solution in the study of near-neutral pH SCC behavior. However, the other synthetic soil solution, termed C1 with composition shown in Table 3-3, was designed based on field data from pipeline failure sites (Chen et al., 2002). From previous research (Chen et al., 2004), C1 solution was more aggressive to SCC than NS4 solution, so all the tests were conducted using C1 solution. The C1 solution was prepared using deionized water and was bubbled with 5% CO_2 in oxygen-free N_2 gas for at least 24 hours before being introduced to the test cells. The bubbling gas was also maintained during each test in order to keep the pH value of the solution at 5.89 and also to get anaerobic environments.

Table 3-2 Chemical components of NS4 solution (Bubbled with 5%CO_2+N_2 balanced)

Composition (g/L)	$MgSO_4 \cdot 7H_2O$	$CaCl_2$	KCl	$NaHCO_3$	pH
NS4	0.131	0.137	0.122	0.483	6.51

Table 3-3 Chemical components of C1 solution (Bubbled with 5% CO_2+N_2 balanced)

Composition (g/L)	$MgSO_4 \cdot 7H_2O$	$CaCl_2$	KCl	$NaHCO_3$	$CaCO_3$	pH
C1	0.0274	0.0255	0.0035	0.0195	0.0061	5.89

37

3.3 Sample preparation

X-52 steel was machined into round smooth tensile samples, as shown in Figure 3-2, for electrochemical tests and slow strain rate tests (SSRT); compact toughness (C-T) samples, as shown in Figure 3-3, for potential drop tests and double notched flat tensile samples, as shown in Figure 3-5, for surface replica tests. In order to investigate the effect of plastic deformation, the samples were pre-strained based on the following formula:

$$\%CW \text{ in rolling: } \%CW = \left(\frac{t_0 - t_d}{t_0}\right) \times 100 \quad \text{------------------------3-1}$$

$$\%CW \text{ in tension: } \%EL = \left(\frac{l_0 - l_d}{l_0}\right) \times 100 \quad \text{--------------------------3-2}$$

Where %CW and %EL present the percent of cold work and percent of elongation respectively, t_0 is the initial thickness of the sample and t_d is the thickness of deformed sample by cold rolling, and l_0 is the initial gauge length of the sample and l_d is the gauge length of the strained sample by tensile loading.

3.3.1 Round tensile sample

The length direction of the round tensile sample was parallel to the circumferential direction of the pipeline steel in order to ensure that the subsequent crack growth was in the longitudinal direction of the pipe as observed in the field. After the samples were machined from the pipe using electrical discharging machining (EDM), the round tensile samples were pre-strained in the gauge length area by an INSTRON hydraulic test frame at a relatively fast elongation rate, 0.02 mm/min. Different amount of plastic deformation, such as 1%, 2%, 4% and 8% were obtained as determined by an extensometer. The sample surface in the reduced area was polished to a 600-grit finish in an orientation parallel to the subsequent loading direction of the SSRT.
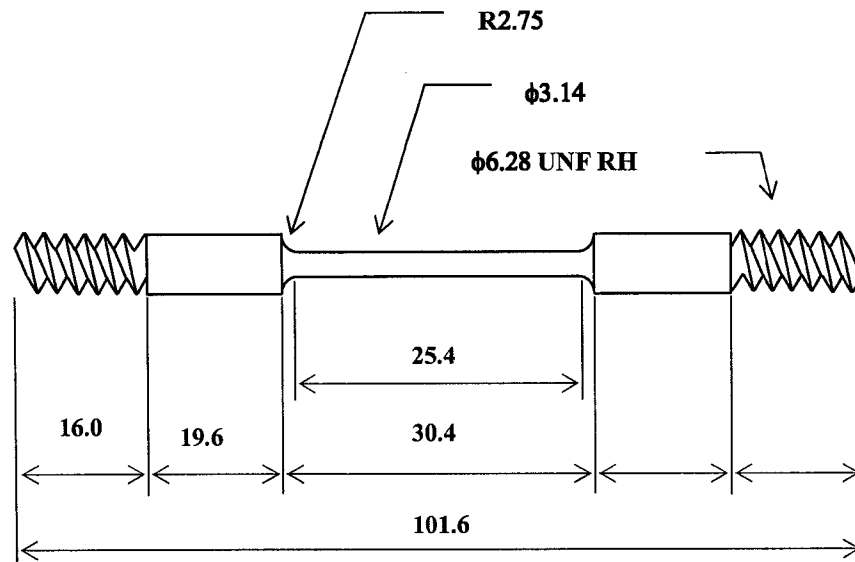
Figure 3-2: Round tensile sample   (unit: mm)

The round tensile samples for electrochemical tests, after pre-straining, were coated using epoxy resin so that just the reduced area was exposed to the test solution for the subsequent electrochemical measurements.

3.3.2 Compact toughness (C-T) sample

The materials cut from the longitudinal direction of the pipeline materials were cold rolled to different amount of plastic deformation (5%, 8%, 10%), then the C-T shape was made using EDM according to ASTM Standard E813-89 except for sample thickness (B), which was limited by the maximum pipe wall thickness that could be utilized. A sharp notch was introduced on the sample along the longitudinal direction with the notch radius being 0.15 mm. The C-T samples were pre-fatigued in air using an INSTRON machine to produce a sharp crack from the machined notch tip, in accordance with ASTM E647. The sample surface was polished to a mirror finish in order to check the crack growth length during pre-fatigue. The maximum stress intensity factor during pre-fatigue was always kept less than 15 MPam$^{1/2}$, which is the lowest limit used in the potential drop test. A load shedding technique was used as

39

shown in Figure 3-4, which intermittently decreased the load as the crack increased in length, was used to minimize the plastic zone size at the crack tip during pre-fatigue. And also a high frequency (16 Hz) was employed for the fatigue loading. The pre-fatigued crack length on both sides of the surface was controlled to be 2-3 mm long. The difference in crack length on the sides of the surfaces of each sample was less than 0.2 mm.

Figure 3-3 Dimension of compact toughness (C-T) sample

Figure 3-4 Schematic of load shedding method for pre-fatigue.

40

3.3.3 Double notched flat tensile sample

The length direction of the double-notched tensile samples was coincident with the pipe circumferential direction in order to ensure the crack growth direction was the same as that in the field. After they were machined from the pipe steel using EDM, the smooth flat tensile samples were loaded in the INSTRON machine, which was used to give them uniform plastic deformation, for example 4%, 8% and 10%. After pre-straining, notches were made on both edges of the samples using EDM. Then the double notched flat tensile samples were pre-fatigued in air using compressive cyclic load, with an absolute value of the minimum stress of 90% of the yield stress measured before the sample was pre-strained. The R ratio of the fatigue (the maximum stress over the minimum stress, since it is compressive) was 0.1 and the frequency was 16 Hz, to produce a sharp crack from the machined notch tip. The pre-fatigued crack length on both edges of the sample was controlled to be 200-300 micron long. The difference in crack length on both sides of each sample was less than 20 micron. The sample surface in the reduced area was polished to a 600-grit finish in an orientation parallel to the subsequent loading direction.
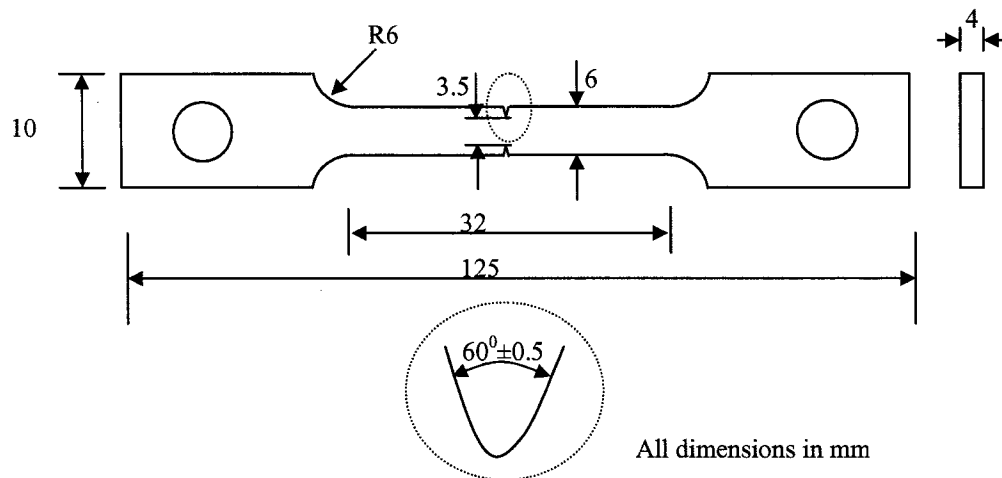
Figure 3-5: Double notched flat tensile sample

Prior to testing, each surface of the sample was degreased using an organic solution (acetone) to remove any surface deposit that might contaminate the test electrolyte.

41

3.4 Test apparatus

3.4.1 INSTRON loading machine

SSRT was conducted in an INSTRON Machine operated by Instron Series IX software. The maximum load capacity of the INSTRON is about 100 kgf and load protection was set at 0.5kN to prevent the machine from running after the sample fractured. All the slow strain rate tests were conducted in position-control mode with a crosshead speed of 0.0004 mm/min for samples tested in C1 solution and a crosshead speed of 0.05 mm/min for samples tested in air.

3.4.2 GAMRY electrochemical system

A potentiostat with GAMRY electrochemical measurement system was used for all electrochemical tests. The GAMRYs DC105 software was used for the open circuit potential, polarization resistance, potentiodynamic and potentiostatic tests. The loading machine was also the INSTRON machine, which can also give the cyclic loading with the WAVE MAKER software.

3.4.3 EnduraTEC equipment

EnduraTEC equipment, which has a controlling system using WinTest software and a data acquisition system with LabView software, was used for the low frequency cyclic loading, potential drop test. Also, a temperature controller was operated to keep the samples working under a nearly constant temperature, the temperature change was controlled to ± 0.1 °C.

3.4.4 First class lever system

A first class lever system was used for the surface-replicating test. The arm ratio from the loading side (*effort*, as shown in Figure 2-13) to the working side (*load*, as shown in Figure 2-13) was 12.83:1. The loading side was controlled by mechanically driven motor operated at specified frequency, which gave the working side the cyclic loading condition.

3.4.5 Microscopes (OM and SEM)

Light optical microscope (OM), Olympus PM3, was used to examine the pre-crack length for sample preparation for both the potential drop test and the surface-replicating test. And also OM was used for the weekly crack growth length measurements of the surface replica tests. Hitachi S-2700 Scanning Electron Microscope Link EXL EDS System (SEM) was utilized to investigate the fracture surfaces and side surfaces of samples from slow strain-rate testing and surface morphology of C-T samples and double notched tensile samples obtained from potential drop tests and surface replica tests respectively.

3.5 Test procedures and data analysis

Several types of test have been performed to investigate the effect of plasticity on the cracking rate. These included electrochemical tests and slow strain rate tests on smooth round tensile samples, potential drop tests on pre-fatigued compact toughness (C-T) samples and surface replica tests on pre-cracked flat tensile samples. Further details of these test techniques are given below.

3.5.1 Slow strain rate test (SSRT)

The slow strain rate test is a rapid method of analyzing different variables that affect SCC susceptibility. The pre-strained round tensile sample was sealed in a plastic container, which was made from transparent polymethyl methacrylate material as shown in Figure 3-6. It contained openings for gas inlet, gas outlet and the sample. An O-ring was placed in the opening on the lid and the other one was placed in the opening on the bottom of the cell in order to prevent leakage of the test solution. The SSRT for the samples tested in C1 solution was normally begun at a crosshead speed of 0.0004mm/min, which corresponded to an initial strain rate of 2.62×10^{-7} s^{-1}, while the crosshead speed of 0.05 mm/min was used for the samples tested in air, which corresponded to a strain rate of 3.28×10^{-5} s^{-1}. The test solution was pre-saturated for two hours with 5% $CO_2 + N_2$ gas mixture to stabilize the system to the open circuit potential (OCP) and was continuously bubbled with 5% $CO_2 + N_2$ gas mixture during

43

the test. The load-elongation curve was recorded. After the test was complete, the fractured sample was immediately removed, ultrasonically cleaned using alcohol or acetone and placed in a desiccator for storage until future SEM examination.
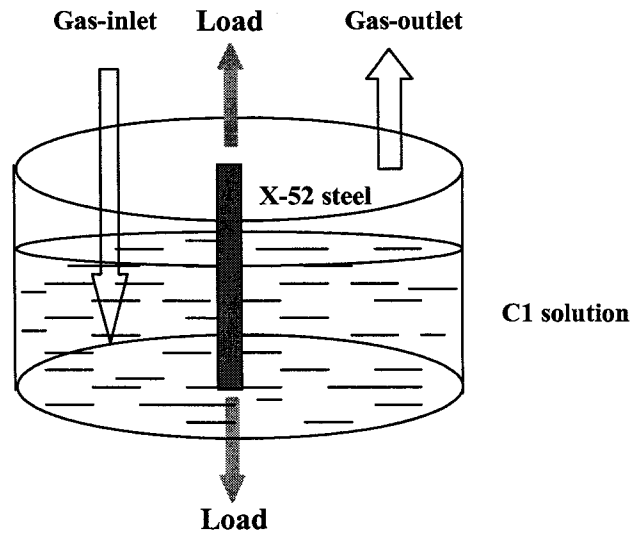
Figure 3-6 Set-up of SSRT cell

The SSRT was conducted on samples in both deaerated C1 solution at open circuit potential (OCP) and an inert environment (air). Figure 3-7 shows the experimental set-up in C1 solution.
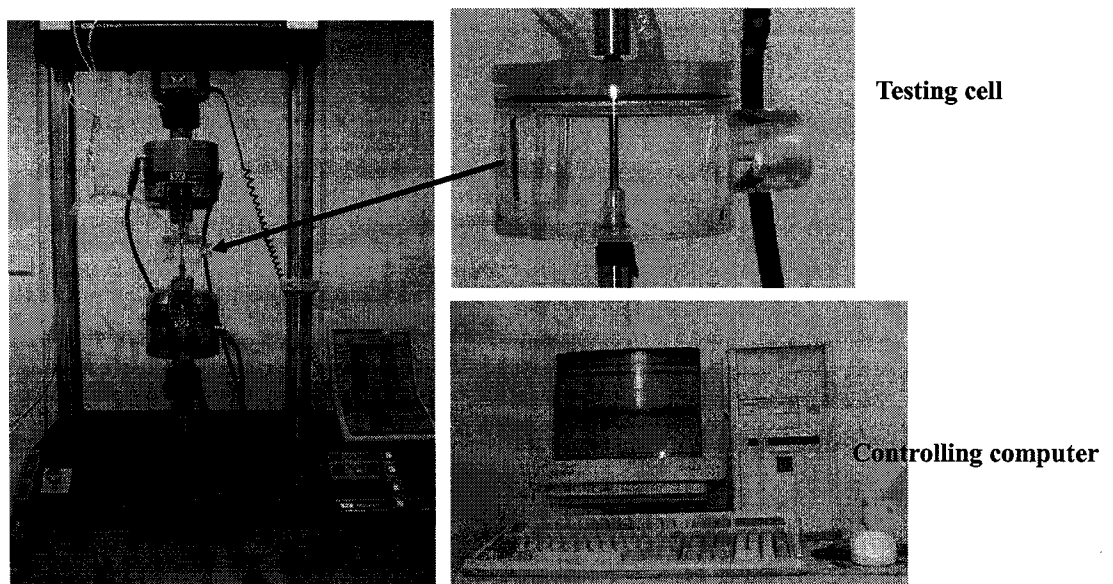
Figure 3-7 Experimental set-up of SSRT

To determine the severity of SCC, a comparison was made between a sample fractured in air and one fractured in the C1 solution. In both cases, the strain to fracture (ε) and reduction of area at fracture (%RA) were determined and the ratio, RA_{SCC}/RA_{air} determined the SCC severity. The severity increased with decreasing value of RA_{SCC}/RA_{air}. And also, the fracture surface was examined using the SEM to determine the fracture features. Failure due to near-neutral pH SCC should have quasi-cleavage on the fracture surface rather than microvoid coalescence.

3.5.2 Electrochemical tests

Based on the fact that the appropriate experiments required to simulate SCC behaviour usually take a large amount of time to complete, it is therefore advantageous to carry out fast-screening tests using electrochemical methods. In this regards, two types of electrochemical tests were conducted namely: linear polarization resistance (Rp) tests and potentiodynamic polarization tests. All the tests were carried out in C1 solution and bubbled with 5% CO_2+N_2 gas mixture. The round tensile sample was sealed in a plastic container, which was almost the same as used for SSR testing except it consisted of extra openings for the reference electrode and counter electrode, as shown in Figure 3-8. A platinum wire (~99.9% pure) of diameter 0.5mm was used as a counter electrode while the saturated calomel electrode (SCE) was used as the reference electrode. A salt bridge was used at the tip of reference electrode to reduce the solution resistance and the contamination of the testing solutions. All electrodes were connected to a GAMRY potentiostat to generate the output from the corrosion cell.

45
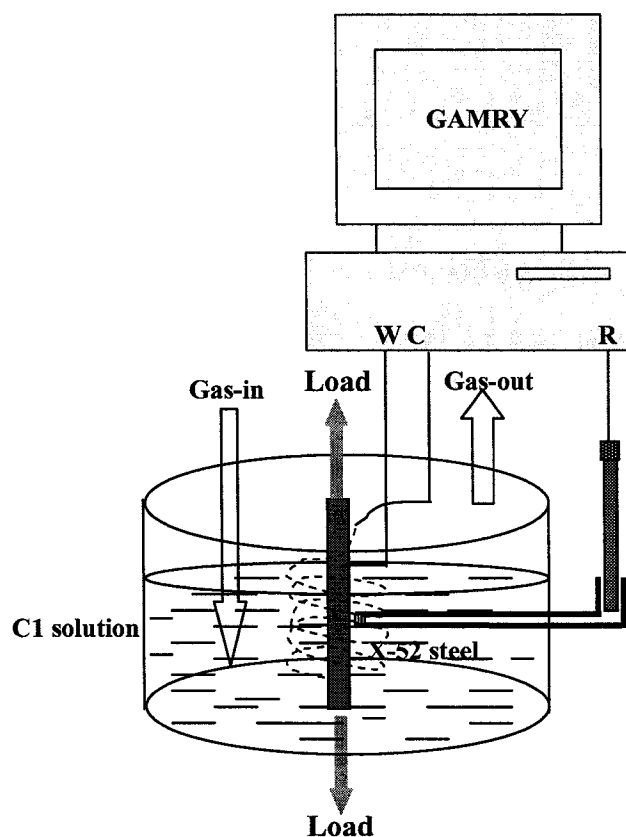
Figure 3-8 Set-up of electrochemical test

The INSTRON machine was used to give the different loading conditions. Short term (1 hour) and long term (24 hours) Rp tests were conducted under cyclic loading conditions in the elastic stress range of the material. Since SCC usually occurs within the vicinity of open circuit potential (OCP), Rp measurement was conducted in the range of ±10mV OCP with scan rate of 0.167mV/sec. A potentiodynamic test was performed to investigate the kinetics of corrosion, the polarization curve was obtained at a scan rate of 0.2 mV/sec starting approximately 250 mV more negative than the OCP and scanning in the noble direction to a potential 650 mV more positive than OCP.

46

3.5.3 Potential drop test

The EnduraTEC equipment was used for the potential drop tests. In each tests, a pre-cracked C-T sample was electrically isolated from the loading clevises and cell hardware and was cyclically loaded in C1 solution bubbled with 5% CO_2+N_2 gas mixture in the plastic cell, as shown in Figure 3-9. A sine waveform load was used with a loading frequency of 0.0025 Hz (relatively high, 216 cycles/day), and R-ratios of 0.375, 0.5 and 0.625. The maximum and minimum stresses were controlled to achieve a maximum stress intensity factor (K) close to 40 $Mpam^{1/2}$, and a ΔK in the range 15 to 25 $MPam^{1/2}$.
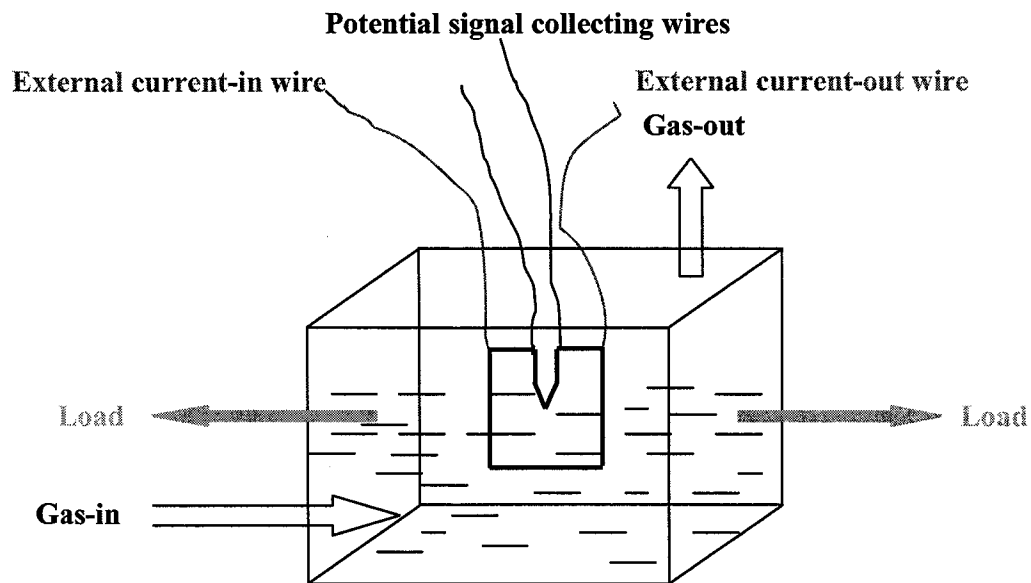
Figure 3-9 Set-up of potential drop testing cell

Crack growth was monitored by a potential drop system, as shown in Figure 3-10.
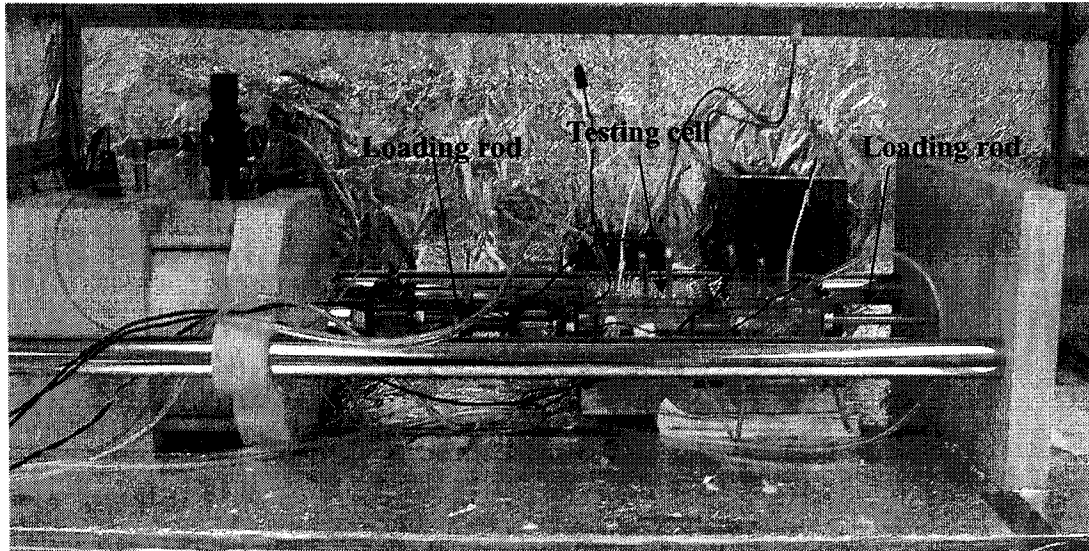
Figure 3-10 Experimental set-up of EnduraTEC equipment

In the system, a constant current of 10 amps was applied across the crack crevice, and the change of potential with time caused by crack growth can be related to crack length. The constant current was applied to the sample only at the time of potential measurement, which was performed approximately every 1 hour for a length of time equal to that of one loading cycle in order to minimize the heating effects from the electrical current. At least 40 data points were collected for each loading cycle. Each of the data points is an average of 20 measurements at positive current, and 20 at reversed current polarity in order to reduce the amount of noise in the data and enable better curve fitting. The test temperature was controlled to be 30 ± 0.1°C in order to eliminate the temperature effect on the resistance of the sample.

After the test was finished, the samples were immersed in liquid nitrogen for about 10 min, and then were broken open. The crack faces were cleaned ultrasonically in acetone solution and the cleaned fracture surfaces were examined by optical microscopy to measure the actual crack growth length, which corresponded to the total potential change recorded. This gave the correspondence between crack growth length and potential change.

48

The stress intensity factor (K_I) could be calculated according to ASTM 399-90 to estimate the stress intensity level in front of the notch tip (Anderson, 1995).

$$f\left(\frac{a}{w}\right) = \frac{K_I B \sqrt{w}}{P} = \left(1 - \frac{a}{w}\right)^{-\frac{3}{2}}\left[\left(2 + \frac{a}{w}\right)\left(0.886 + 4.64\frac{a}{w} - 13.32\left(\frac{a}{w}\right)^2 + 14.72\left(\frac{a}{w}\right)^3 - 5.6\left(\frac{a}{w}\right)^4\right)\right]$$

------------------------------------3-3

Where a and B are crack length and sample thickness, respectively; w is the width of the sample and P is the applied load.

3.5.4 Surface replica test

The cyclic loading regime simulated pressure fluctuations on an operating pipeline and was applied using a mechanical cyclic loading frame system, which is schematically shown in Figure 3-11. The pre-cracked tensile samples were cyclically loaded in C1 solution bubbled with 5% $CO_2 + N_2$ gas mixture. A triangle waveform load was used with a loading frequency of 5.787×10^{-4} Hz (50 cycles/day), and a R of 0.21 (R=minimum stress / maximum stress). The test cell set up is shown in Figure 3-12. The maximum stress used in the test was around 0.9 SMYS (specified minimum yield stress before the samples were pre-strained). The tensile samples were pin-hole loaded in series and sealed in the plastic test cells with the test solution filled above the reduced area of the samples.

The test was interrupted after the desired time (usually one week) for crack growth measurements. Crack growth lengths were measured by replicating technology (Parkins, 1999). In order to make crack observation easier, it is of practical importance to keep the cracks open by using a static load equal to the maximum cyclic load of the test during the replicating process (Lu et al., 2002). The appropriate length of acetate tape with acetone on one side was pressed firmly on the crack tip area of the sample being careful to apply tape so as to squeeze out air bubbles. Usually 20 to 30 minutes later, after the tape had dried thoroughly, the replica was

49

stripped from sample surface, the replicating process using acetone-treated replica tape is shown in Figure 3-13. This replica would generally showed dirt from the surface. It is best to discard this replica and repeat the above steps to get a clean replica. The edges of replicating tape were fastened down, and the replica was measured using optical microscopy (OM). After the test was finished, the fractography of the broken samples were examined with SEM to identify the cracking features.
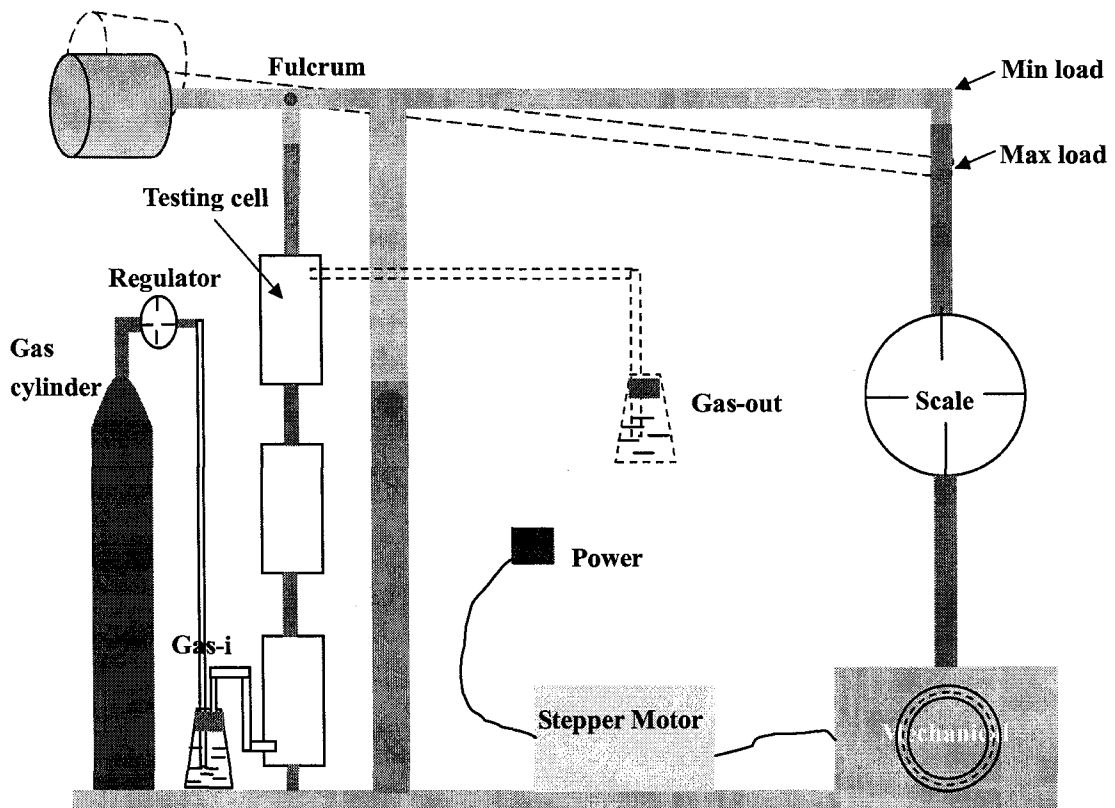
Figure 3-11 Experimental set-up of surface replica test

50
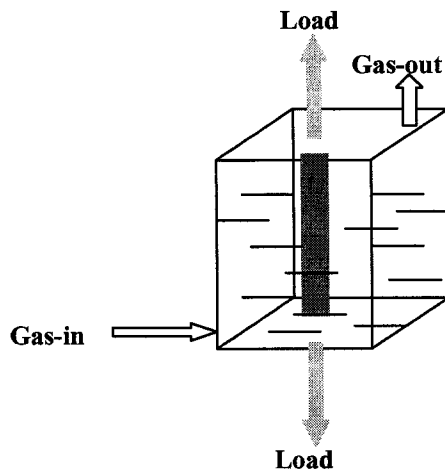
Figure 3-12 Set-up of surface replica testing cell
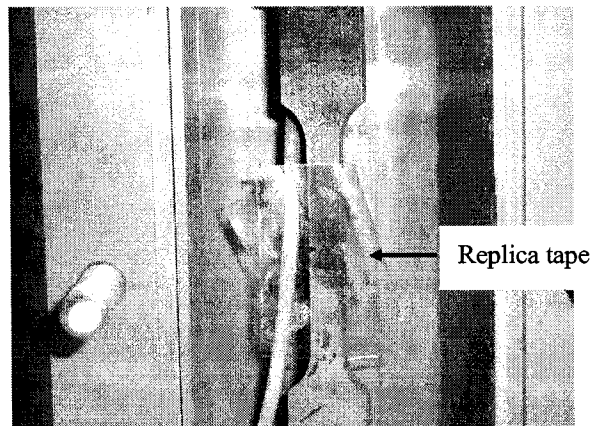
Figure 3-13 Replicating process using acetone-treated replica tape

For double notched sample with cracks subjected to tensile loading, the stress intensity factor (K_I) was calculated using the following formula (Anderson, 1995):

$$f\left(\frac{a}{w}\right) = \frac{K_I B\sqrt{w}}{P} = \frac{\sqrt{\frac{\pi a}{2w}}}{\sqrt{1-\frac{a}{w}}}\left[1.122 - 0.561\left(\frac{a}{w}\right) - 0.205\left(\frac{a}{w}\right)^2 + 0.471\left(\frac{a}{w}\right)^3 + 0.190\left(\frac{a}{w}\right)^4\right]$$

---3-4

Where 2w is the width of the sample, B is the thickness of the sample, P is the applied load, and a is the crack depth from the edge to the crack tip.

51

4 Results and Discussion

The influence of cold work on properties and on near-neutral pH SCC was studied from various aspects. Section 4.1 shows the changed mechanical properties, such as elongated grains, increased yield strength as well as hardness due to strain hardening. This is followed by section 4.2, electrochemical characteristic studies of potentiodynamic polarization behaviour and linear polarization resistance. The main objective of these measurements was to evaluate the effect of deformation on corrosion rate. Sections 4.3, 4.4 and 4.5 are the main parts of this thesis work, which present the results of SSRT, potential drop tests and surface replica tests, respectively. The fracture characteristics and the relationship between plasticity and SCC susceptibility are obtained. Finally, a brief discussion of the above results is made in section 4.6 based on the main factors contributing to near-neutral pH SCC.

4.1 Microstructure and Mechanical properties

Plastic deformation is permanent and un-recoverable, and strength and hardness are measures of a material's resistance to this kind of deformation. On a microscopic scale, plastic deformation corresponds to the net movement of large numbers of atoms in response to an applied stress. During this process, the interatomic bonds must be ruptured and then reformed, and the grains must be elongated; on a macroscopic scale, the strength and hardness are increased while the ductility is sacrificed.

4.1.1 Microstructure of deformed materials

Figure 4-1 presents the metallographic images of un-deformed sample (0%) and 10% plastic strained sample. The microstructure of X-52 steel consisted of fine pearlite and ferrite with a grain size of 10 um to 20 um, as shown in Figure 4-1 (a) while the 10% deformed samples had elongated pearlite and ferrite as presented in Figure 4-1 (b). As the percentage of cold work increased, the grains were more and more elongated along the tensile loading direction, which is illustrated as the arrowhead directions.

(a)0%	(d) 10%

Tensile loading direction

Figure 4-1 Microstructures of samples with various amounts of plastic deformation, the bright part is ferrite and the dark one is pearlite.

4.1.2 Tensile properties

Figure 4-2 shows the yield strength of the samples with different amount of plastic deformation. The actual yield strength increased from 448 MPa to 617 MPa for samples with 0%, 1%, 2%, 4%, and 8% plastic deformation tested in air. For samples tested in C1 solution whose composition was given in Table 3-3 in the experimental section, the yield strength had the same increasing trend and the value changed from 439 MPa to 607 MPa for the 0% to 8% pre-strained samples.
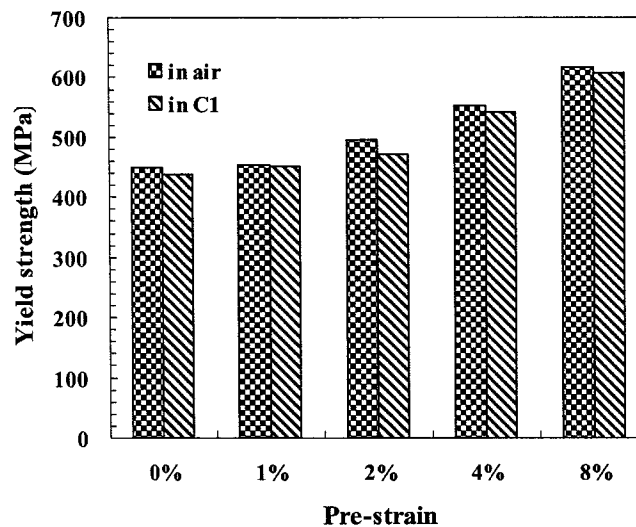
Figure 4-2 Yield strength of various amounts of pre-strained samples tested in air and in C1 solution.

The increase of yield strength with cold work of materials tested in air and in C1 solution is plotted in Figure 4-3. The maximum yield strength increase of the 8% sample to the un-deformed sample was around 40%. The yield strength had a slightly smaller increase for materials tested in C1 solution than for those tested in air.

54

50%

40%

♦ Yied strength in air
● Yield strength in C1

Pecentage of increase

30%

20%

10%

0%

0%   1%   2%   4%   8%
              Pre-strain
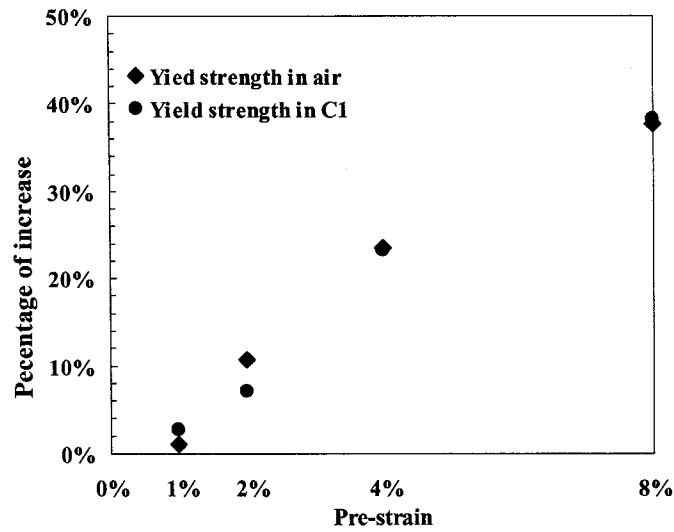
Figure 4-3 Yield strength increase of various amounts of pre-strained samples tested in air and in C1 solution (compared to the undeformed sample)

4.1.3 Hardness of deformed materials

Hardness is a material's resistance to localized plastic deformation. For Vickers micro-hardness test, a small diamond indenter is forced into the surface of the test material. The softer the material, the larger and the deeper the indentation, and the lower the hardness index number. Also, the Vickers micro-hardness test requires careful sample surface preparation, such as grinding, polishing and etching.

Results of the average of three measurements on each sample are shown in Figure 4-4, the hardness of X-52 steel increased with increasing plastic deformation.

55
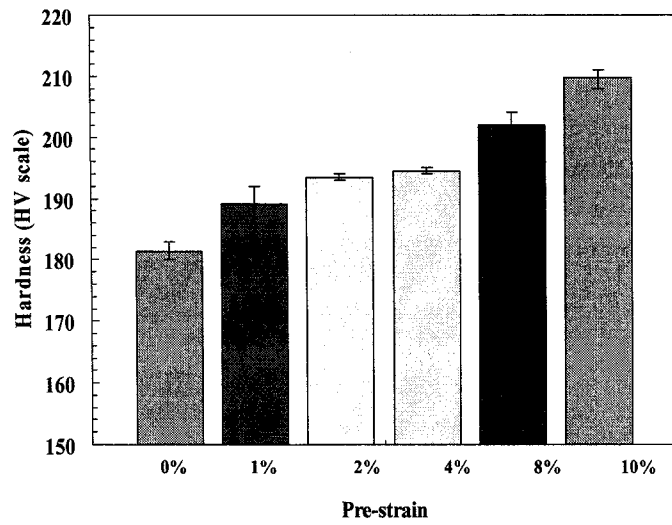
Figure 4-4 Hardness of the deformed samples, applied load: 2kg, loading time: 20 s.

Both strength and hardness are indicators of a metal's resistance to plastic deformation. Consequently, they are readily proportional as shown in Figure 4-5. This linear relationship between yield strength and hardness of steels has been reported by different researchers (Davis, 1998 and Bulger, 2000)
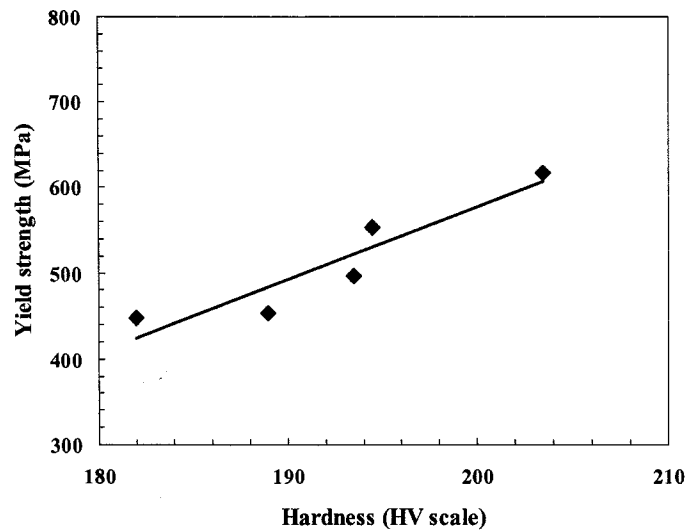
Figure 4-5 Relationship of yield strength and hardness of the deformed samples

56

4.2 Electrochemical characteristics

Based on the fact that the appropriate experiment required to simulate SCC behaviour usually takes large amount of time to complete, it is therefore desirable to carry out fast-screening tests using electrochemical methods. These studies can provide a rough idea of the rate of anodic dissolution and this can be compared to SCC velocity.

4.2.1 Effect of plastic deformation on OCP and corrosion rate

Figure 4-6 shows the polarization curves of samples with different amount of plastic deformation measured in C1 solution at room temperature. These curves were obtained when the open circuit potentials (OCPs) were stable after the samples had been exposed to the solution for one hour. It was demonstrated that the OCP of X-52 steel in near-neutral pH environment was around -740 mV and there was no active to passive transition zone as many researchers have observed before (Parkins, 1998, Beavers et al., 1998 and Gu et al., 1999 (1)). Therefore, during the crack growth process, dissolution was not localized, and there was no passivation on crack walls to prevent lateral dissolution and retain the crack shape.
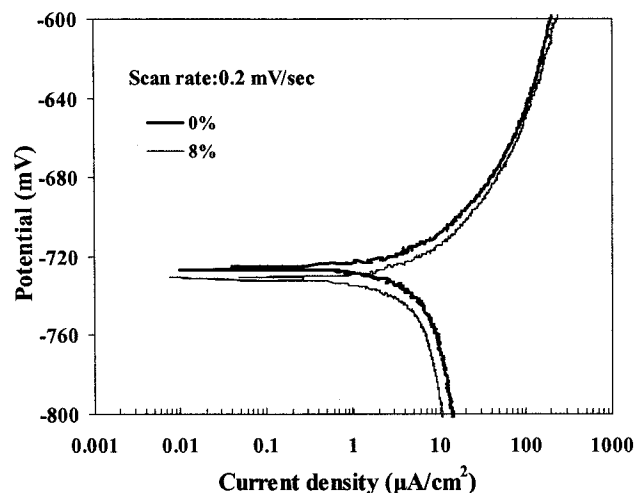
Figure 4-6 Polarization curves of samples with various amounts of prior plastic deformation tested in C1 solution.

The OCPs and corrosion current densities of the steels determined from the polarization curves are plotted against various plastically deformed samples in Figure 4-7. It is seen that the OCP appeared to be not very sensitive to plastic deformation (the maximum difference of OCP between various amounts of pre-strained samples was just 25 mV). However, the corrosion current was much higher for samples with more plastic deformation and the maximum difference of corrosion current density was around 130 $\mu A/cm^2$.
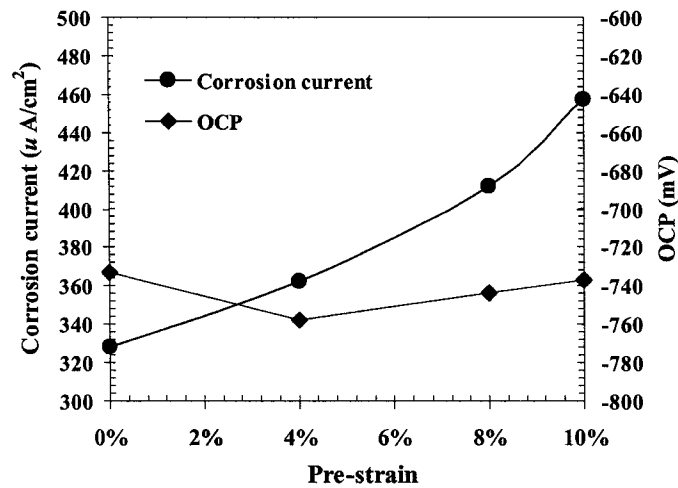
Figure 4-7 OCPs and corrosion rates of samples with various amounts of plastic deformation

4.2.2 Effect of cyclic stress on corrosion rate

It is broadly believed that SCC in near-neutral pH environment is the synergistic effect of anodic dissolution and hydrogen-assisted cracking. Based on this fact, a set of fast screening tests, linear polarization resistance (Rp) tests, were designed to investigate the corrosion rates of samples under cyclic loading condition in the elastic range of the steel in near-neutral pH environment. As a control experiment, the Rp was also measured under the stress free condition. Short-term (around 1 hour) and long-term (around 24 hours) Rp were obtained and the results are shown in Figure 4-8. For the short-term test, the Rp was measured every 5 minutes. While for the long-term test, the Rp was measured every 1 hour.

58
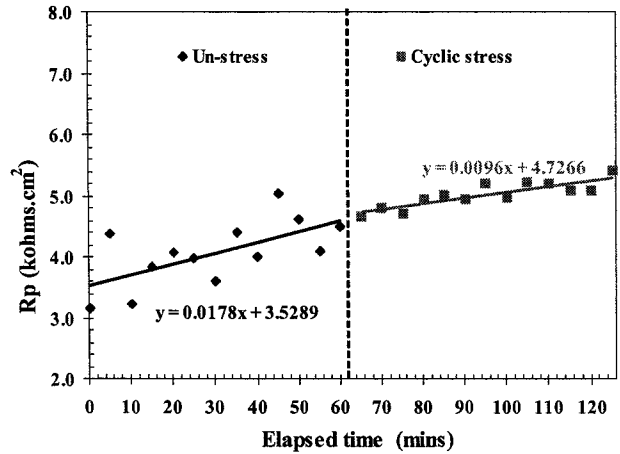
(a) Short term (1 hour)
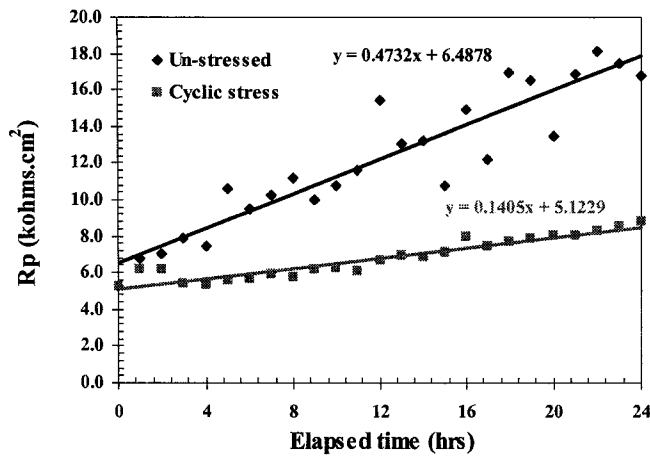
(b) Long-term (24 hours)

Figure 4-8 Linear polarization resistances of the un-deformed samples under stress free and cyclic stress condition in the elastic range of X-52 steel.

The two tests in the short-term group were conducted on the same sample continuously. After 1-hour test under stress free condition, the cyclic elastic stress was given on the sample immediately without taking the sample out of the test cell, as shown in Figure 4-8 (a). It is reasonable to continue the test without re-polishing the sample surface because the sample was just immersed in the solution for two hours (1 hour for deaerating and 1 hour for Rp measurement). However, for the long-term test, the sample had to be re-polished after the testing under stress free condition because

59

25 hours (1 hour for deaerating and 24 hours for Rp measurement) was a really long time and the surface condition of the sample would have changed too much. This re-polishing effect can be observed from the start points of the two tests in long-term group which was shown in Figure 4-8 (b), they fell at almost the same point.

The slope of the trend line of the above data shows an increase in Rp with time. From Figure 4-8 (a), the increase rate of Rp under stress free condition was 0.018 (min^{-1}), while it was 0.010 (min^{-1}) for sample under the cyclic elastic stress condition. This result indicated that the cyclic stress made the Rp increase more slowly with time compared to the relatively large rate of increase of Rp under stress free condition. This effect is more apparent when the samples were tested for long term (24 hours) as shown in Figure 4-8 (b). The Rp-increasing slope of sample tested under stress free condition was 0.473 (hr^{-1}), which was much higher than that under the cyclic elastic stress condition, $0.141(hr^{-1})$. This indicates that the cyclic elastic stress slowed the rate of increase of the polarization resistance.

Recalling corrosion mechanism, at the linear polarization zone (over-potential< 10 mV), the Stern formula gives the relationship of corrosion current density and the polarization resistance: $i_{corr} = \dfrac{B}{R_P}$, Where $B = \dfrac{b_A b_C}{2.3(b_A + b_C)}$, b_A and b_C are the slopes of Tafel lines and A and C are anode and cathode.

The corrosion current density is inversely proportional to the polarization resistance, so the corrosion current density increases more slowly with time under the effect of cyclic elastic stress.

All of these electrochemical measurements indicate that the anodic dissolution rate could be increased when the material is under loading condition in a near-neutral pH environment. However, these are just fast screening tests, the anodic current detection needs to be conducted during the SCC process.

60

4.3 SSRT behaviour

The slow strain rate tensile testing is a convenient method for a quick evaluation of the susceptibility of a material to SCC. Tensile samples are pulled to failure in an inert environment (air) and in a near-neutral pH SCC causing environment (C1 solution), and then a ratio of the ductility of material tested in C1 solution to that in air is used to compare the susceptibility of the SCC. For example, if the ductility is decreased due to SCC, the ratio will decrease. Therefore the ratio indicates the severity of SCC. The choice of the failure ratio used to determine the resistance of SCC in not limited to the ductility, but can be yield strength, time to failure or reduction in area.

In this section, the samples were pre-strained to different amount of plastic deformation, and then the SSRT were performed on the pre-strained samples to determine if the plastic deformation has an effect on SCC severity.

4.3.1 Stress-strain curves of the deformed materials

The influence of pre-strain on the SSRT properties of the steel in air and in C1 solution was investigated and the typical experimental results are presented in Figures 4-9. The stress-strain curves for the samples tested in C1 solution and in air were basically identical up to the ultimate tensile strength and then there was a faster decline of the stress with increasing strain for the sample in tested C1 solution compared to that completed in air. The stress-strain behavior of samples with 1%, 2% and 4% pre-strain was similar to that with 0% pre-strain. Pre-strain made the samples lose some ductility comparing Figure 4-9 to Figure 4-10, which are Stress-strain curves for 0% and 1% samples. The ductility decreased by the amount of the pre-strain, for both samples tested in air and in C1 solution. Since the loss of ductility for the 8% pre-strained sample was too much, the stress-strain curves fell down soon after the yielding point, as shown in Figures 4-11.

61
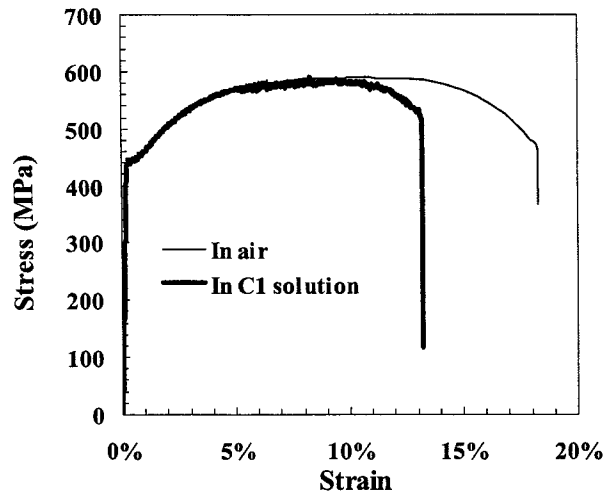
Figure 4-9 Stress strain curves of 0% samples tested in air and in the C1 solution

(strain rate in C1 solution: $2.62 \times 10^{-7} s^{-1}$, strain rate in air: $3.28 \times 10^{-5} s^{-1}$)
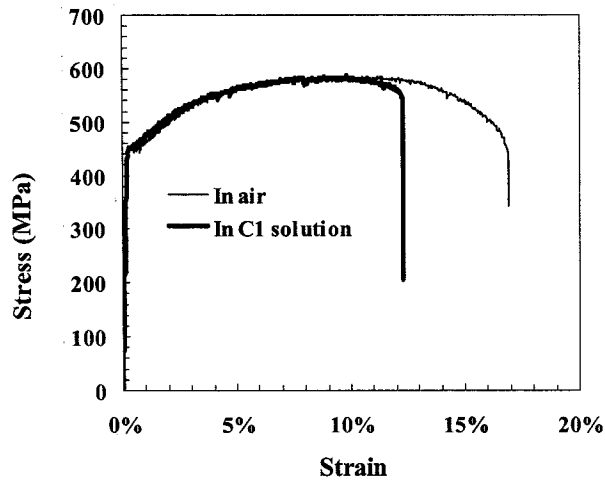
Figure 4-10 Stress strain curves of 1% samples tested in air and in the C1 solution

(strain rate in C1 solution: $2.62 \times 10^{-7} s^{-1}$, strain rate in air: $3.28 \times 10^{-5} s^{-1}$)

62
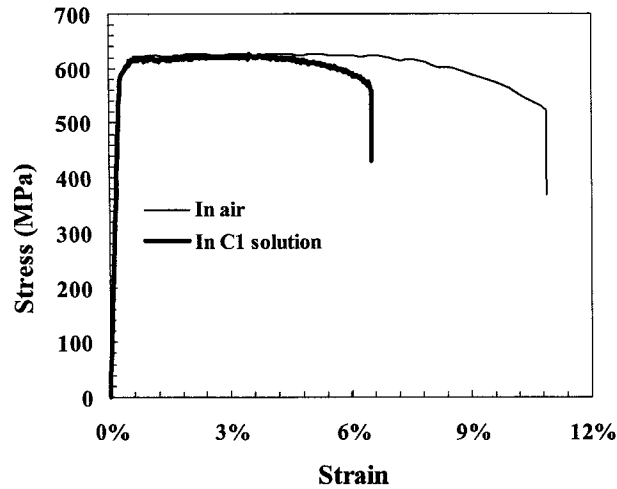
Figure 4-11 Stress strain curves of 8 % samples tested in air and in the C1 solution

(strain rate in C1 solution: $2.62 \times 10^{-7} s^{-1}$, strain rate in air: $3.28 \times 10^{-5} s^{-1}$)

The remaining ductility of all the pre-strained samples is summarized in Figure 4-12. As expected, the ductility of the material was sacrificed because of pre-staining. The un-deformed (0%) samples had the highest ductility both in air and in C1 solution, which were 18.3% and 13.3% respectively. While the ductility of the 8% pre-strained samples tested in air and in C1 solution were just 10.9% and 6.5% respectively. Other samples had the intermediate ductility depending on the amount of pre-strain. Finally, it could be concluded that the ductility decreased with the increase of the amount of pre-strain, and for the samples with the same amount of pre-strain, the ductility tested in air was always higher than that tested in C1 solution. The reason for this difference could be explained by the quasi-cleavage failure observed when the material was exposed to C1 solution. This will be discussed further in the next section.

63
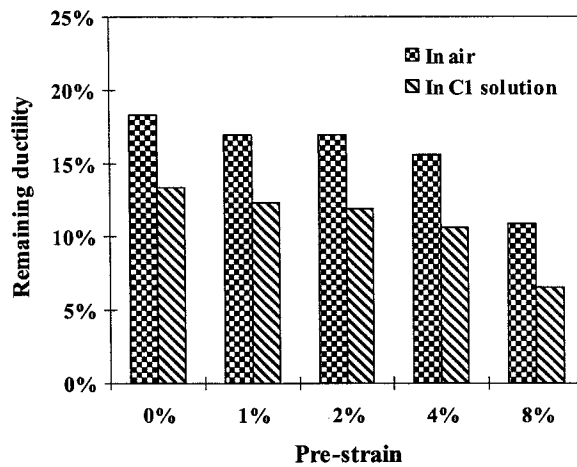
Figure 4-12 Remaining ductility (%EL) of various amounts of pre-strained samples

(the initial gauge length is 25.4 mm)

Figure 4-13 summarizes the total effects of cold work: increased yield strength and decreased ductility. By using 0% sample as the standard, all the data in Figure 4-13 were based on this reference. For the most severe case, the 8% pre-strained sample had 60% yield strength increase comparing to the 0% sample, but the remaining ductility was only one third of that for the sample with no pre-strain.
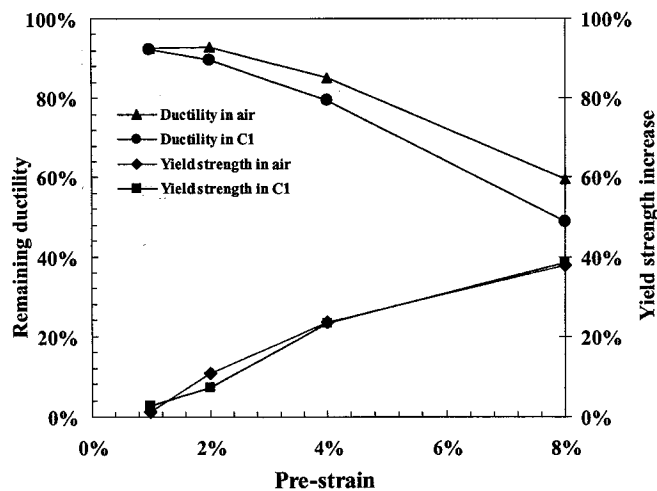
Figure 4-13 Remaining ductility (%EL) and yield strength increase of various amounts of pre-strained samples (the initial gauge length is 25.4 mm)

64

4.3.2 SCC susceptibility assessment

Based on the above analysis, there are big differences in the ductility of different samples tested in air and in C1 solution. A comparison of the reduction in area, as shown in Figure 4-14, also shows that there is a significant difference in ductility and hence in the ratio of the reduction in area to rupture in C1 solution and in air. It is proved again that RA_{SCC}/RA_{air} can be used as the indicator of susceptibility to near-neutral pH SCC. The magnitude of the failure ratio indicates the SCC severity with a decreasing value indicating more severe SCC. Based on years of development of this test method, typically, a ratio <0.85 indicates that SCC has occurred (Bulger, 2000).
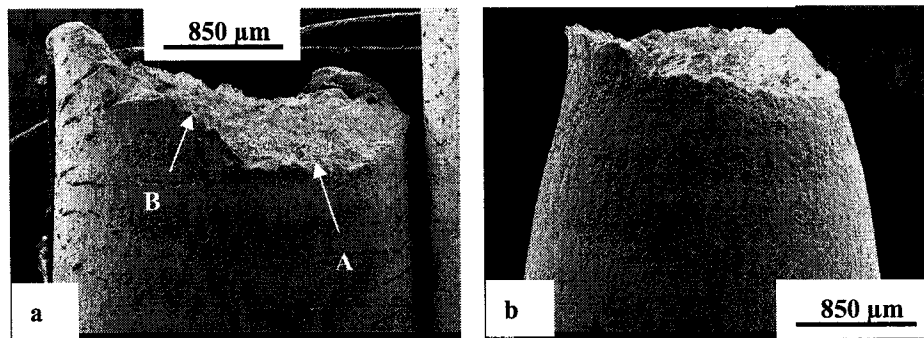
Figure 4-14: Images of the failed un-deformed samples (a) in C1 solution, (b) in air

The results of the SSRT of various amounts of pre-strained samples are plotted in Figure 4-15. The 8% pre-strained sample had the least resistance to near-neutral-pH SCC as indicated by having the lowest failure ratios of 62.9%. Conversely, the 0% pre-strained sample had greatest resistance to SCC with a failure ratio of 66.9%. The other samples had intermediate failure ratios with the 1% sample showing more resistant to SCC than the 2% and 4% samples.

65
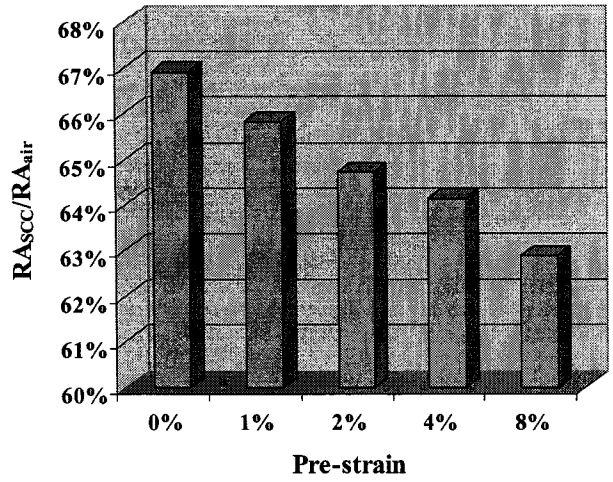
Figure 4-15 SCC performance of various amounts of pre-strained samples in C1 solution

The reproducibility of this SCC susceptibility assessment was checked by another two samples (0% and 4%) immersed in C1 solution. Figure 4-16 shows several stress-strain curves of the 4% pre-strained samples tested in air and in C1 solution. The error bars of the reduction in area showing in Figure 4-17 imply that the reproducibility of this SSRT method is good enough and it can be used to assess SCC susceptibility of variously pre-strained samples.
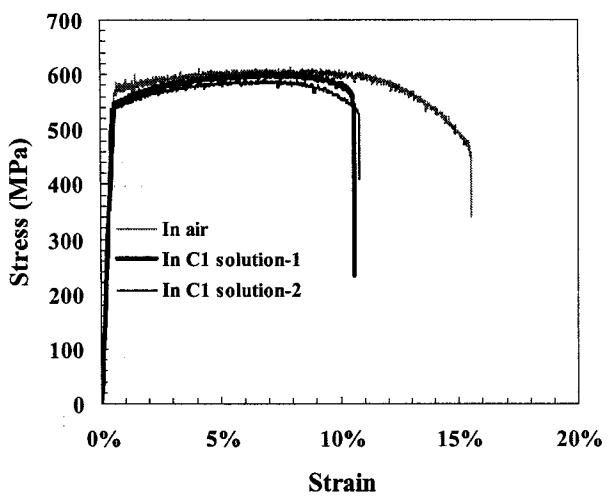
Figure 4-16 Stress strain curves of the 8 % samples tested in air and in the C1 solution

(strain rate in solution: $2.62 \times 10^{-7} s^{-1}$, strain rate in air: $3.28 \times 10^{-5} s^{-1}$)

66
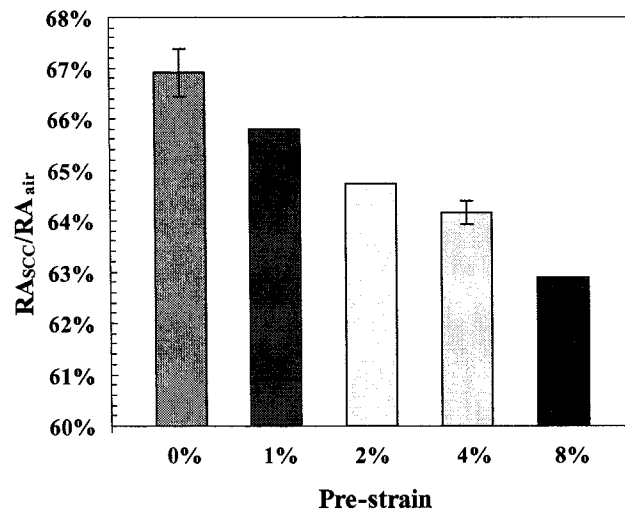
Figure 4-17 Reduction in area of the 0% and 4% pre-strained samples showing the reproducibility of the SSRT method

The variation in the severity of the SCC with a variation in the amount of pre-strain indicates that SCC resistance is a function of prior plastic deformation. Although it is conclusive from the SSRT, other test results from potential drop tests and surface replica tests, which will be shown in the following sections, are consistent with it.

4.3.3 Fractography of the fracture surface

Based on years of experience, there are two pre-conditions for using SSRT to investigate the material's susceptibility to SCC. The first one was mentioned in section 4.3.2, the failure ratio in SCC causing environment and in air is less than 0.85. The second condition is that the fracture surface displays features that indicate the failure is due to SCC rather than mechanical failure, which means there is some cleavage or quasi-cleavage on the fracture surface.

There is another reason to examine the fracture surfaces. Section 4.3.2 showed that varying the amount of prior plastic deformation of X-52 pipeline steel varied the severity of near-neutral-pH SCC. The variations in severity ranged from relatively

67

severe in the samples with large pre-strain, mild in the samples with small pre-strain and light in the un-deformed sample. A hypothesis is that this severity is also reflected on the fracture surfaces.

The fracture surfaces of the pre-strained samples failed in C1 solution were examined using SEM and the results are shown in Figure 4-18. All of these pictures were taken near the edges of the fracture surfaces.

Figure 4-18 (a) is the fracture surface of the 0% sample showing a large portion of quasi-cleavage facets. The size of the biggest facet in the center of the image is around 35 μm, as shown by the arrow in Figure 4-18 (a). The fracture surface of the 1% sample in Figure 4-18 (b) shows a slightly larger quasi-cleavage region cross the image from the top right hand to the bottom left side and surrounded by some small microvoid coalescence on the right side and ductile tearing on the left side. The size of the biggest facet in the center is around 40μm. This is followed by the fracture surface of the 2% sample, which has a traditional cleavage facet with a size of about 40 μm in the bottom of a hole. The generation of the hole probably is due to the dissolution of the manganese sulphide (MnS), the evidence will be shown in Section 4.3.4. For the 4% sample, some small dimples intersect with the two big facets in the center. Even though some corrosion product is still on the fracture surface of the 8% sample, the quasi-cleavage still could be observed on the bottom of the hole.

There are also secondary cracks on the fracture surface of the 0% sample. These secondary cracks are transgranular demonstrating that the proper test conditions were achieved during testing. The walls of the cracks are much wider because of lateral dissolution (Wang et al., 1998) and the tips of the cracks are much blunter indicating that they have become dormant.

All of these quasi-cleavage and secondary cracks are indications of occurrence of near-neutral pH SCC.

68
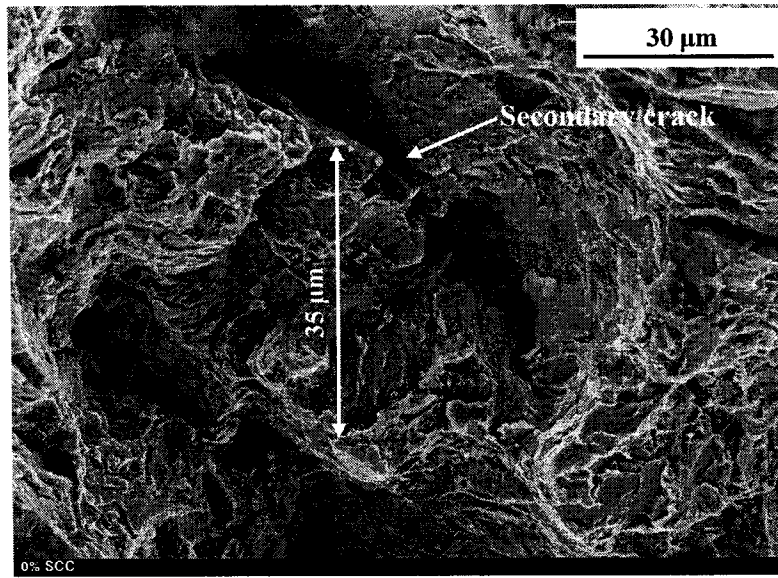
(a) 0%
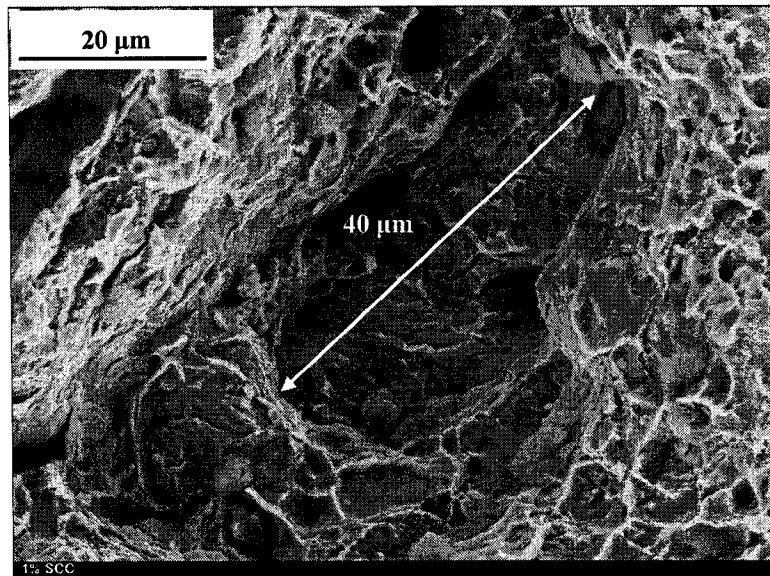
(b) 1%
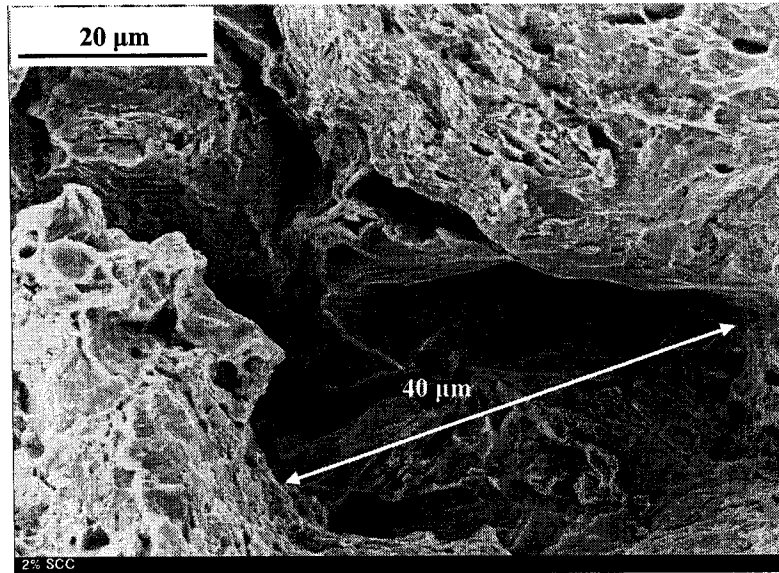
(c) 2%
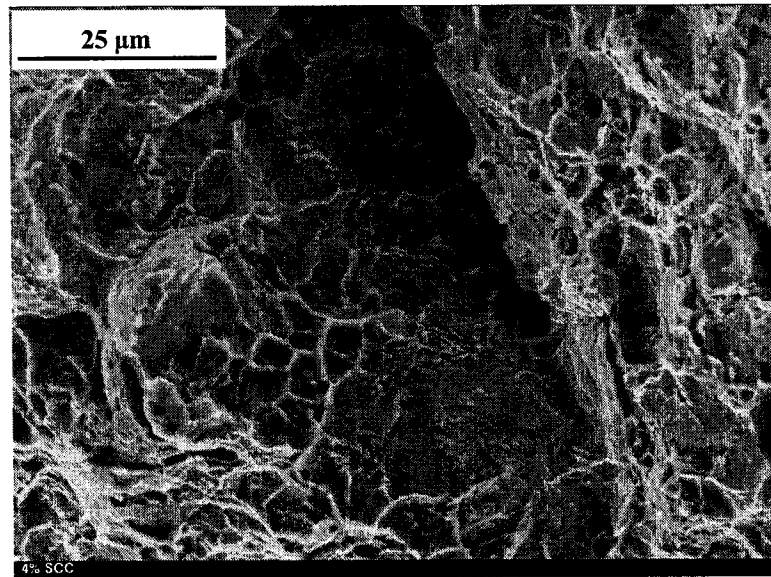
(d) 4%
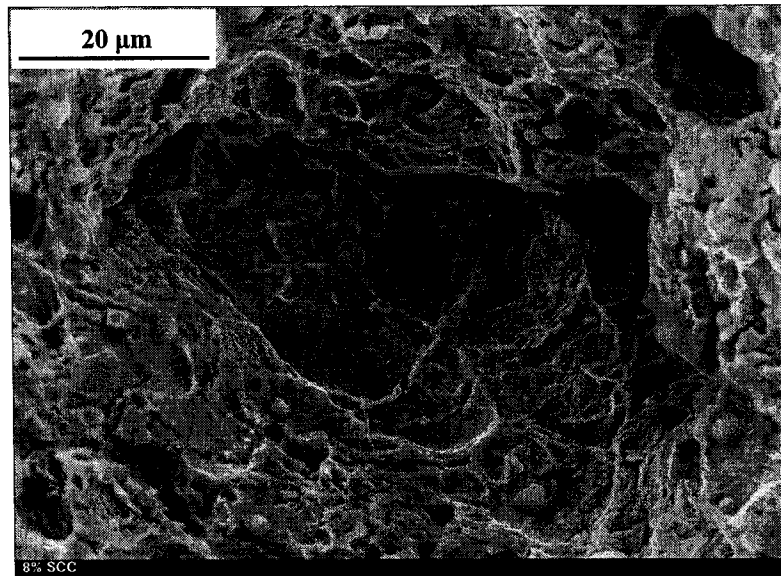
(e) 8%

Figure 4-18 SEM images showing fracture surfaces of the pre-strained samples tested in Cl solution, quasi-cleavage and dimples mixed on the surface

Based on the above examination, SCC readily occurred at the edges of the fracture surface, some part of which displayed quasi-cleavage and secondary cracks. At the center of the fracture surface, ductile dimples were found.

In order to compare the fracture mode, the fracture surfaces of samples failed in air were also examined. Figure 4-19 shows the typical ductile fracture, the dimples were the halves of the coalesced microvoids.
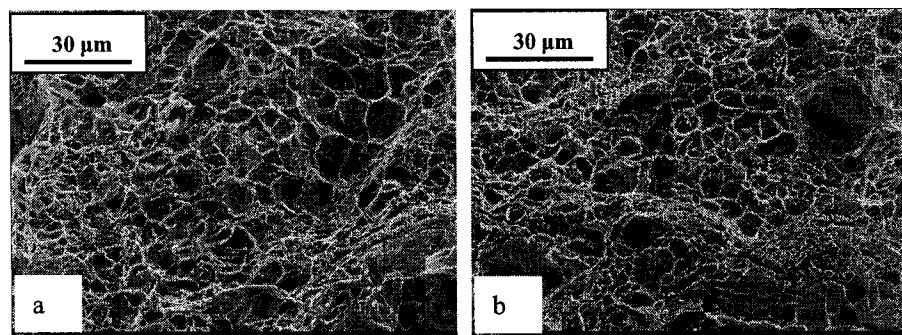
Figure 4-19 SEM images showing the ductile fracture of samples tested in air (a) 0% sample (b) 1% sample

71

The fracture surface tested in C1 solution generally consisted of a flat area at the edge (site A in Figure 4-14(a)), which was perpendicular to the stress axis, and a surface inclined to the stress axis (site B in Figure 4-14 (a)). The cup-cone feature, which was often seen on fracture surfaces of samples tested in air, as shown in Figure 4-14 (b), was not observed on the fracture surfaces of samples tested in C1 solution, indicating that failure initiated from surface cracks rather than from void-induced cracks at the center of the sample (Chen et al., 2002). The flat area at the edge of the fracture surface resulted from the cracks at the sample surface, while the inclined surface at the failed end was observed to take place at the final stage of failure and was caused by slant tearing as a result of the reduction in cross-section area by necking and by SCC on the surface (Chen et al., 2002). Another reason is that the inclined cracks might have resulted from preferential dissolution at the persistent slip bands arising from tensile loading (Wang et al., 2000).

Figure 4-20 shows the surface cracks of different pre-strained samples. A series of small surface cracks were along the pre-existing crack-like defects, and some of these small cracks were approximately perpendicular to the principal tensile loading direction, while the others were about 45 degree to the stress axis. The small cracks joined together, and further growth occurred only at the two extreme ends.

The flat surface cracks characterized by cracks perpendicular to the stress axis, should have taken place at the locations with the highest stress regardless of plastic deformation. However, the 45-degree slant cracks coincided with the direction of the highest shear stress on the sample. On the plane with the highest shear stress, slip steps could be formed on the sample surface, which would cause further corrosion (Chen et al., 2002).

72
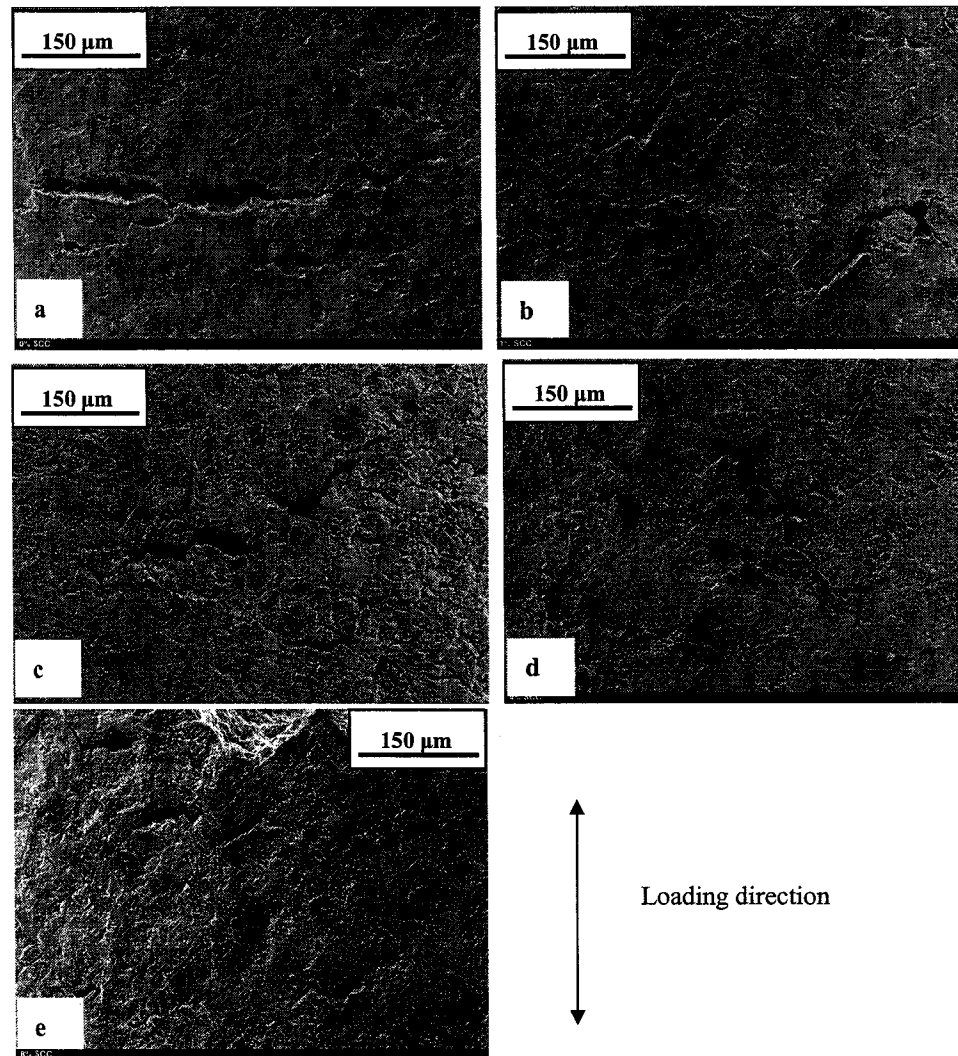
Figure 4-20 Surface cracks near the failed ends of the of various amounts of pre-strained samples tested in Cl solution (a) 0% (b) 1% (c) 2% (d) 4% (e) 8%

In the above figures, the 0% pre-strained sample only had the flat surface cracks and the other samples had the mixed slant and flat surface cracks. The occurrence of the slant cracks on the surfaces of the samples with more prior plastic deformation was ascribed to the loss of ductility during pre-strain, which would induce lower exposure time in the solution when conducting SSRT. Hence there was only insignificant corrosion dissolution or hydrogen cracking at stress raisers on the surface, even though there were more dislocations.

73

In Figure 4-20, the width and length of the surface cracks are different, but there is no definite trend. There are three reasons behind this difference. The first is the different dissolution rates of the crack walls. From the results of section 4.2.1, the dissolution rate is much higher for samples with a larger amount of plastic deformation, and this makes the crack much wider and longer for more deformed samples. The second reason is that cracks will initiate on non-metallic inclusions, it means that the size of the inclusions would affect the shape of the cracks (Wang et al., 1998). Thirdly, since the sample already lost some ductility due to pre-strain, the lower the pre-strain, the more the remaining ductility. This is confirmed by different sample failure times under the same strain rate, for example, it was 7 days to rupture for the 0% sample, but the 8% sample failed at the end of the fourth day. The longer test time would allow much heavier corrosive attack on the crack walls and much more crack growth.

The surface crack in Figure 4-21 shows a central cavernous region with a much slenderer crack emanating from either side. This can be explained as the crack initiation on the dissolution site of an MnS inclusion. After dissolution occurs on the crack walls as the crack grows, it is more likely to cause widening of the crack mouth.
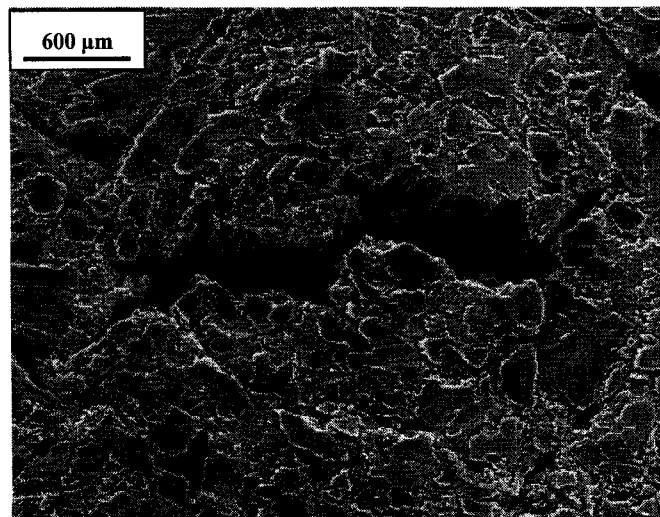
Figure 4-21 Surface crack of the 2% pre-strained sample tested in C1 solution.

74

4.3.4 Effect of MnS

The involvement of MnS inclusions is demonstrated in Figure 4-22. It contains the biggest inclusion found in the fracture surface of the 8% sample, which has a width around 8 μm and length of about 120 μm, and also a much smaller inclusion is included in Figure 4-22, which has a width of 2 μm and a length of 25 μm. Based on EDX analysis (Figure 4-23), these inclusions are all MnS. If some elongated MnS inclusions dissolve in some region that will change the electrolyte chemistry and lead to local acidification of the crack tip (Kuniya et al., 1992). So the dissolution of MnS acts as both a hydrogen source and trapping site, which will accelerate near-neutral pH SCC.

Another possible effect of MnS proposed by Wranglen involves the preferential dissolution of the matrix surrounding a MnS inclusion (Wranglen, 1974). MnS is noble to iron and is slightly soluble in most solutions. In terms of composition, the matrix surrounding the MnS inclusion is contaminated with sulphur and submicroscopic MnS inclusions. During the corrosion process, the main MnS inclusion is a cathodic site for hydrogen reduction, the surrounding sulphur containing matrix is a highly active anodic site and severely corroded. The surrounding matrix, which is highly corroded can be explained from the following three reasons: firstly, MnS is noble to iron so there is a galvanic effect; secondly, the fine dispersion of submicroscopic MnS inclusions increases the surface area between the cathode (MnS) and anode (iron) and thirdly, a submicroscopic MnS inclusion has higher solubility creating sulphide ions that polarize the cathodic and anodic reactions.

The possible reason of these two opposite opinions is the different composition of the test solutions, which will affect the relative potential of MnS and irons. Based on the above analysis, no matter whether there is dissolution of MnS or the surrounding matrix, the effect of MnS inclusion is either providing more hydrogen into the steel or increasing local anodic dissolution rate.

75
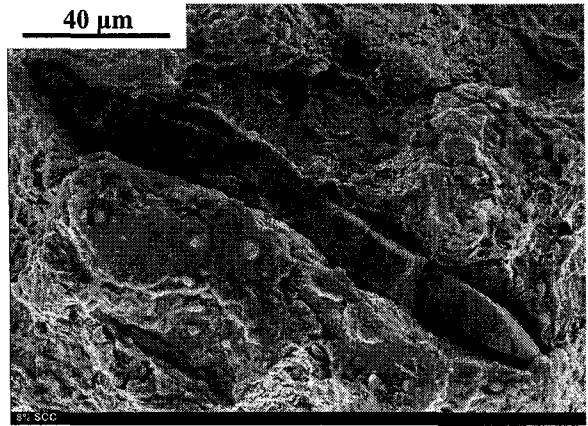
Figure 4-22 Elongated MnS inclusions in X-52 low carbon steel
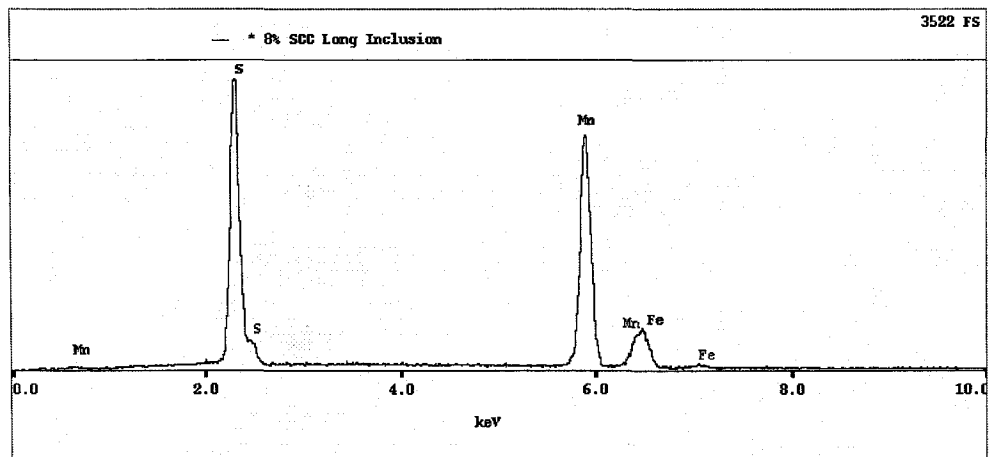
Figure 4-23 EDX analysis showing the composition of the inclusion

76

4.4 Potential drop test

The direct-current-potential-drop method brings more reliable results in measuring crack length at constant temperatures (Nakai and Wei, 1989, Gu and Yu, 1990). It can give the relationship between the crack growth length and the measured potential drop.

According to literature, within the relative crack size range (a/W) of 0.3 to 0.5, when the ratio of crack length increament to the initial crack size ($\Delta a/a_0$) is less than 0.2, the crack length increament can be quite reasonably related to the potential drop by a linear relationship (Johnson, 1965, McIntyre, 1974)

4.4.1 Potential drop profiles

As described in the experimental section, four different cold worked samples were tested. In the test setup, two samples were tested together. During each test, different loading conditions were applied, which corresponded to different R-ratios. The changing stress intensity factor (ΔK_I) should be determined by the changing load. By considering the crack geometry, the variation of load was achieved by changing the minimum load while keeping the maximum load constant.

Typical potential drop profiles of samples with various plastic deformations are shown in Figure 4-24. As illustrated on these curves, at the initial stages I, the changes in potential drop were extremely fast until the number of cycles reached 350, which corresponded to the end of stage I. These parts of the curves were eliminated since they did not reflect actual crack growths but the pre-crack opening effects. For the stages, where $\Delta K_I \approx 25$ MPa$\sqrt{m}$ and 20 MPa$\sqrt{m}$, the curves obtained from potential drop tests for all the samples were relatively linear. It indicated that the crack growth length could be related to the measured potential drop directly. However, for the 0% sample, at the first stage, where $\Delta K_I \approx 15$ MPa$\sqrt{m}$, the data were more scattered. It is believed that this problem was caused by temperature control difficulties. In order to

77

eliminate this scattering, more cycles were used for this stage, which allowed crack growth measurement to be made from the linear part of the curve. From the point of consistency, more cycles were also given to the second stage of $\Delta K_I \approx 15$ MPa $\sqrt{m}$ of the 0% sample and the all the stages of $\Delta K_I \approx 15$ MPa $\sqrt{m}$ of the other three samples. For the tests of the 5% and 8% samples, at the stages II, as shown in Figures 4-24 (b) and (c), no data were collected.
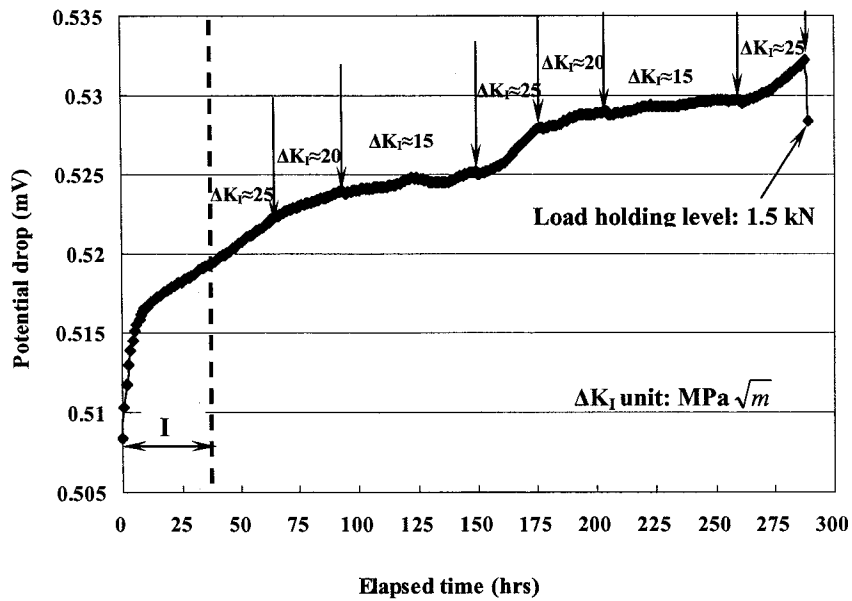
(a) 0% pre-strain
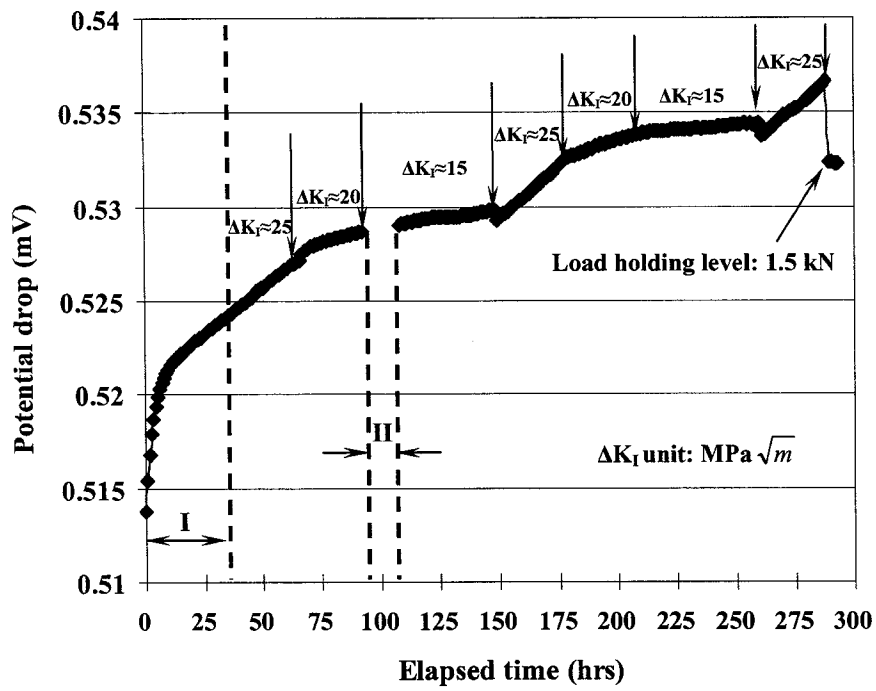
(b) 5% pre-strain
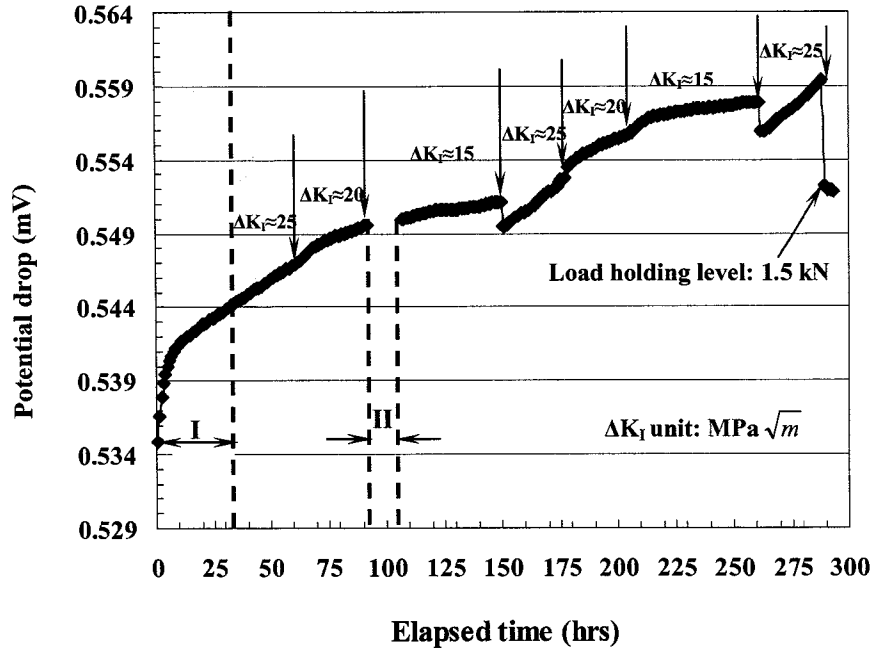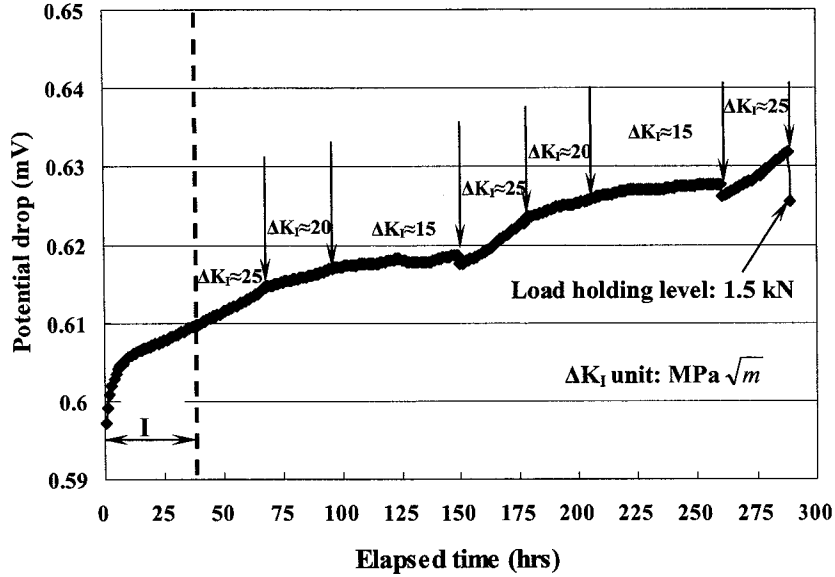
(c) 8% pre-strain

Figure 4-24 Potential drop curves of various amounts of pre-strained samples at different ΔK_I

(d) 10% pre-strain

At each stage, the different slope of the potential drop curve indicates the crack growth rate is different. The higher the slope, the faster the crack growth. The slopes of the three stages, where $\Delta K_I \approx 25$ MPa$\sqrt{m}$, of the 0% sample as shown in Figure 4-24 (a) were almost the same. Similar trends were also observed for the stages, where $\Delta K_I \approx 20$ MPa$\sqrt{m}$ and the stages, where $\Delta K_I \approx 15$ MPa$\sqrt{m}$ as shown in Table 4-1. The same trends of the slopes were observed for the 5%, 8% and 10% samples, but they were a little higher than that of the 0% sample. The relatively average slope ranking was: 10% >8% > 5% >0%, as shown in Figure 4-25.

80

Table 4-1 The slopes of potential drop vs. time curves at different ΔK_I stages

Pre-strained sample	Slope (mV/hour)		
	$\Delta K_I \approx 25$ MPa$\sqrt{m}$	$\Delta K_I \approx 20$ MPa$\sqrt{m}$	$\Delta K_I \approx 15$ MPa$\sqrt{m}$
0%	1.2×10^{-7}, 9.0×10^{-8}, 9.2×10^{-8}	4.2×10^{-8}, 3.4×10^{-8}	1.2×10^{-8}, 9.8×10^{-9}
5%	1.0×10^{-7}, 8.8×10^{-8}, 9.7×10^{-8}	4.2×10^{-8}, 4.3×10^{-8}	1.4×10^{-8}, 1.2×10^{-8}
8%	1.1×10^{-7}, 1.2×10^{-7}, 1.3×10^{-7}	6.7×10^{-8}, 7.8×10^{-8}	2.2×10^{-8}, 1.8×10^{-8}
10%	1.4×10^{-7}, 2.1×10^{-7}, 2.1×10^{-7}	8.5×10^{-8}, 7.7×10^{-8}	2.4×10^{-8}, 2.6×10^{-8}
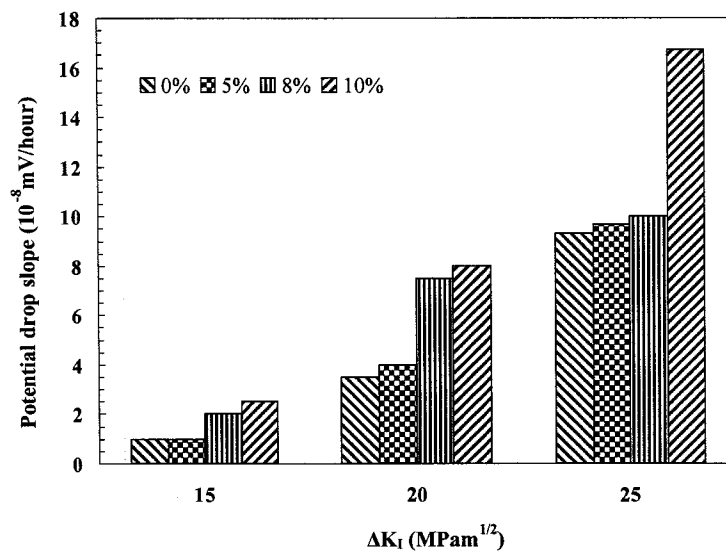
Figure 4-25 Average potential drop slopes of the pre-strained samples at different ΔK_I

In Figure 4-25, for all the samples, the slopes of potential drop increased as the ΔK_I increased. This implied that the crack growth rate increased with ΔK_I. The good reproducibility of slope of each stage, as demonstrated in Table 4-1 supports the contention that the measured potential drop was due to the change in the crack growth rate caused by changing of load.

It can be concluded now that the crack growth rate ranking is: 10% >8% >5% >0%. However, the exact growth rate value in terms of mm/s and/or mm/cycle should be determined based on crack growth and potential drop measurements.

81

4.4.2 Crack growth measurement

After the tests, the samples were cut into halves along the thickness. One half was used for the crack path examination as presented in Section 4.4.3, the other half was broken open in liquid nitrogen for crack growth measurement. As shown in Figure 4-26, the regions between the pre-fatigue lines and crack end tip lines were the crack growth areas due to near-neutral pH SCC.

(a) 0%
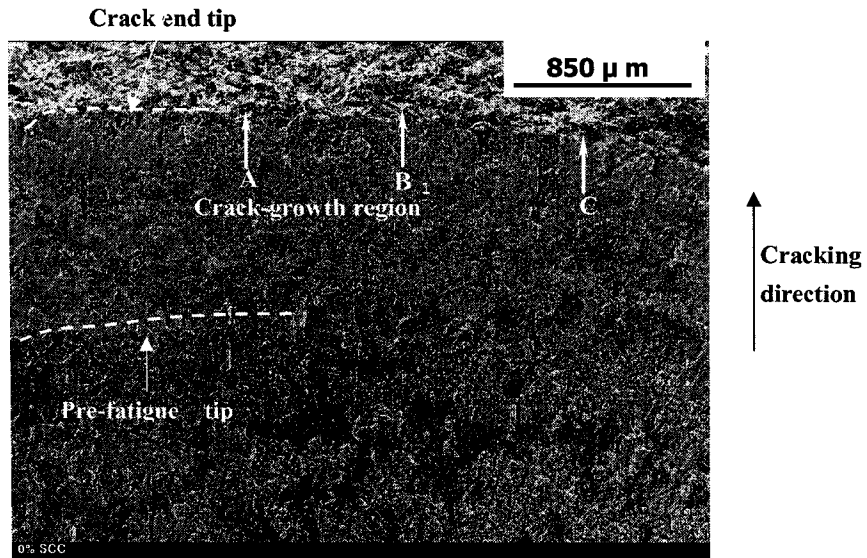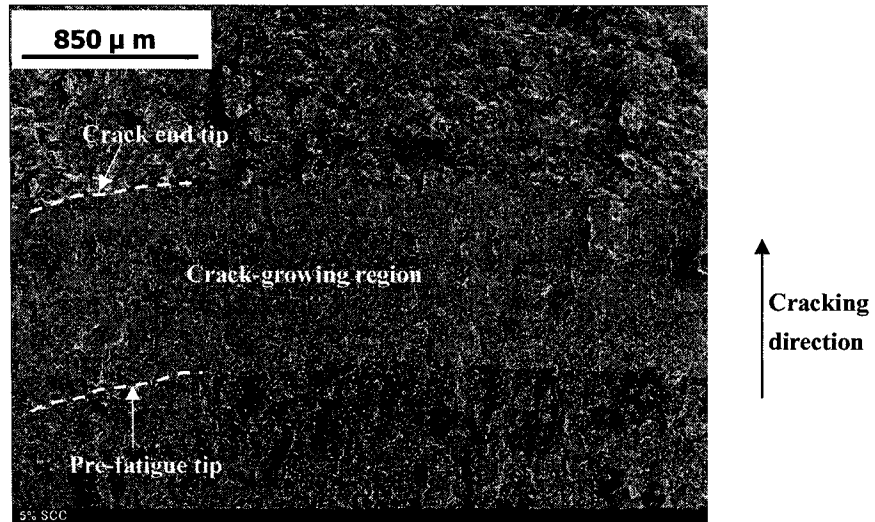
(b) 5%
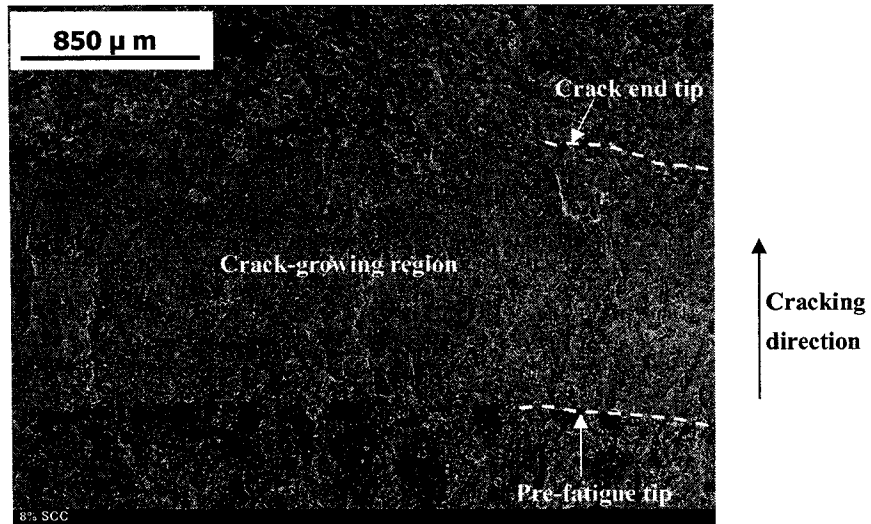
(c) 8%
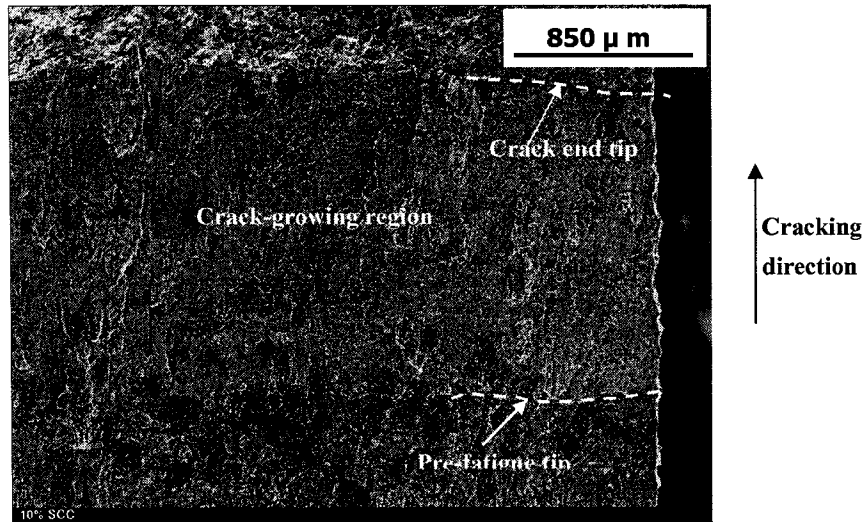
(d) 10%

Figure 4-26 SEM fractograghs showing the crack growth of samples with various amounts of prior plastic deformations

For each sample, the crack growth length was measured at three different points, A, B and C, as shown in Figure 4-28 (a). The crack growth lengths of different amounts of pre-strained samples are summarized in Figure 4-27. There are two reasons for the use of the three-point method. The pre-crack came out on the two sides surface of the sample was not equal, as shown in Table 4-2. Crack 1 is the crack coming out on one

83

surface, and crack 2 is the same crack coming out on the other surface. The actual crack length used for the calculation is the average of these two. On the other hand, the subsequent crack growth might not be uniform.

Table 4-2 Pre-crack lengths of various amounts of pre-strained samples

Sample ID	0%	5%	8%	10%
Crack 1 (mm)	2.47	2.465	2.60	2.46
Crack 2 (mm)	2.48	2.47	2.67	2.47
Average (mm)	2.475	2.4675	2.635	2.465
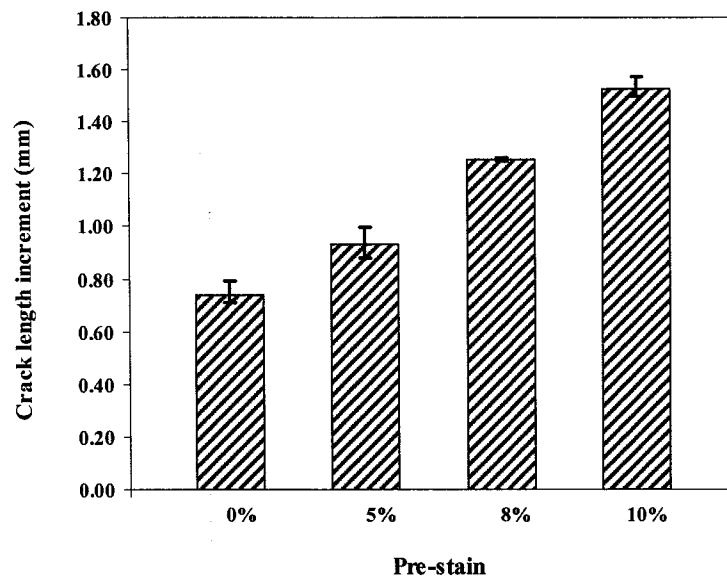
Figure 4-27 Crack growth length of various amounts of pre-strained samples.

From Figure 4-27, the 10% sample had the highest crack growth length, 1.52 mm, during a12 day test. While the crack growth length for the 0% sample was relatively small, 0.74 mm. The crack growth lengths of the other samples were in between those of 10% and 0% samples.

84

4.4.3 Crack path

Samples were prepared for optical microscopy examination by polishing the sides of the samples to reveal the crack path. Examination showed transgranular cracks traversing both pearlite and ferrite to the crack tip, and also the cracks meandered as shown in Figure 4-28.
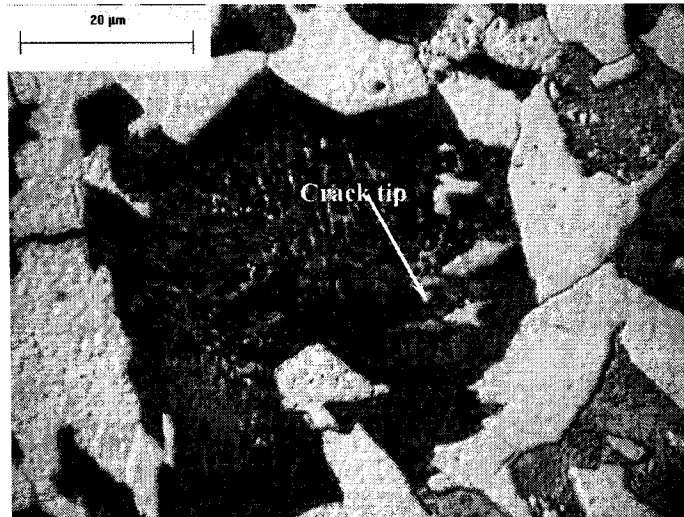
(a) 0%
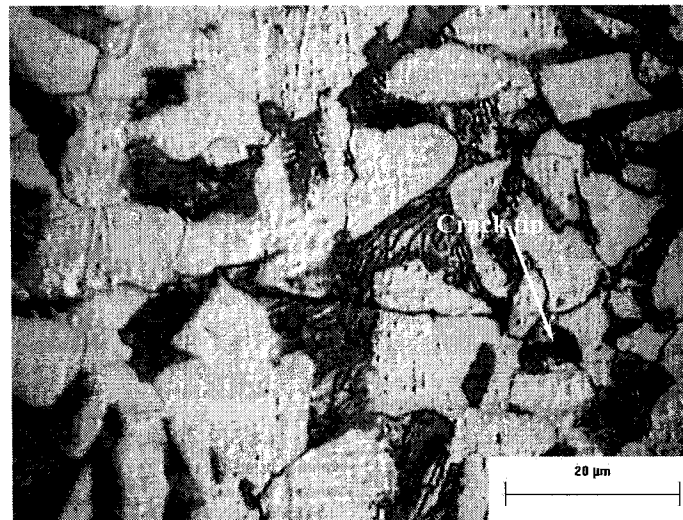
(b) 10%

Figure 4-28 Images showing the crack tip morphologies of various amounts of pre-strained samples after cracking in C1 solution (etched with 2% nital)

85

4.4.4 Quasi-cleavage on the fracture surface

The fracture features were examined by the SEM, as shown in Figure 4-29. The fracture surface of all the samples displayed quasi-cleavage and secondary cracks.

(a) 0%
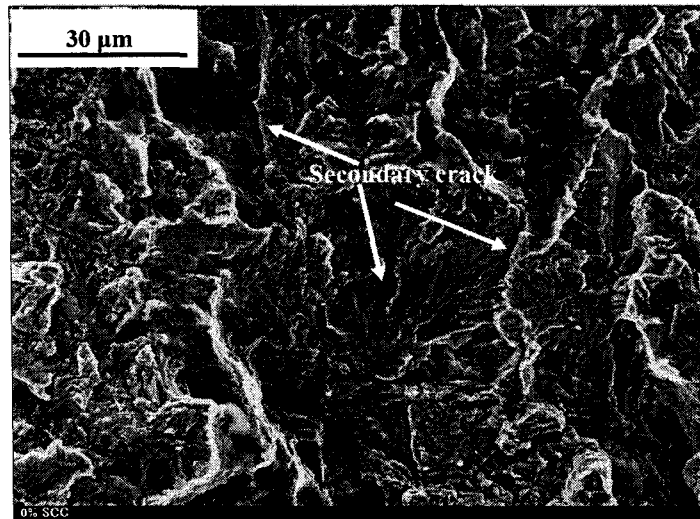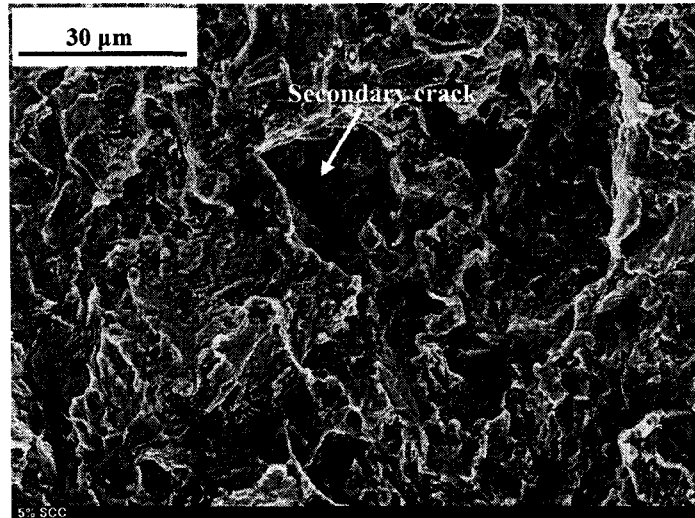
(b) 5%
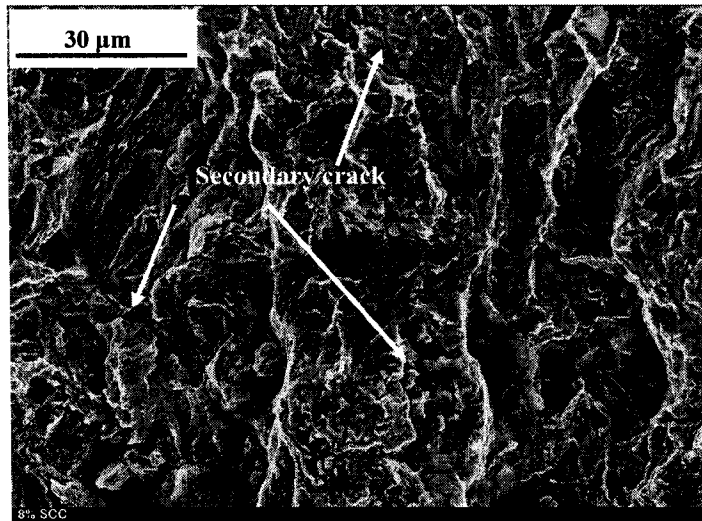
(c) 8%
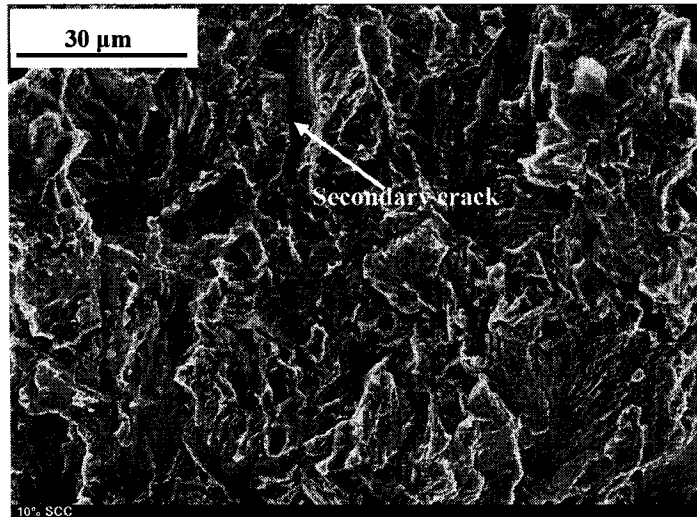
(d) 10%

Figure 4-29 SEM images showing the quasi-cleavage on the fracture surface of

various amounts of pre-strained samples

4.4.5 Crack growth rate

Based on the measurements, after 12 days testing, the 0% sample had a total potential

drop 1.54×10^{-5} mV with a crack growth length 0.74 mm while the potential drop for

10% sample was 2.58×10^{-5} mV and the crack growth length was 1.52 mm. Based on

these data, the correspondence between crack growth length and potential change can

be summarized in the Table 4-3.

Table 4-3 Data of crack growth rate measurements

Sample ID	0%	5%	8%	10%
Crack length(mm)	0.7413	0.9347	1.2520	1.5247
Potential drop(mV)	1.54E-05	1.57E-05	1.74E-05	2.58E-05
Correspondence(mm/mV)	48076	59429	71768	59041

After getting the crack growth length of per unit potential change, the crack growth rate can be got by multiplying this value by the potential change then dividing by the loading time of each loading stage.

Different loading stages correspond to different ΔK_I values. The exact ΔK_I value is also related to the actual crack length according to Equation 3-3 in the experimental section.

Finally, the crack growth rate for each ΔK_I stage could be obtained. The calculated average crack growth rates are given in terms of growth in millimeter per cycle, which are shown in logarithm scale in Figures 4-30. The data of 5%, 8% and 10% samples are fit well with the linear lines since the goodness of fit of interpolation is reflected in the goodness of fit value, R^2, approaching unity. Even the R^2 is 0.852 for 0% sample, but the linear line still can be used to roughly show the trend of the crack growth rate.
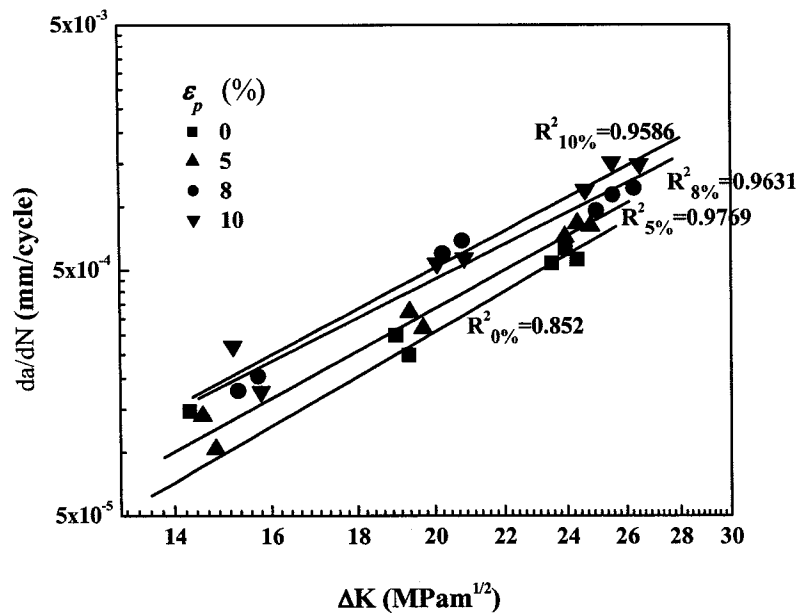
Figure 4-30 Crack growth rates of various amounts of pre-strained samples at different ΔK_I conditions in near-neutral pH environment.

In Figure 4-30, when ΔK_I was larger than 14 MPa$\sqrt{m}$, the crack growth rate increased with percent deformation and the crack growth rate in terms of mm/s was in the range of 1.02×10^{-7} mm/s to 3.39×10^{-6} mm/s. It fell into the same range as Harle and Beavers obtained (Harle and Beavers, 1993). The crack growth rate they got based on potential drop measurements by using API X-65 line pipe steel also ranged from 10^{-7} mm/s to 10^{-6} mm/s.

Figure 4-31 plots the crack growth rate against the yield strength of various amounts of pre-strained samples at different ΔK_I conditions. The maximum yield strength increase of the 10% sample compared to the 0% sample was about 41%. However, when ΔK_I was around 15 MPa$\sqrt{m}$, 20 MPa$\sqrt{m}$ and 25 MPa$\sqrt{m}$, the crack growth rates of the 10% sample severely increased to 2.2, 2.2 and 2.3 times compared to those of the 0% sample respectively.
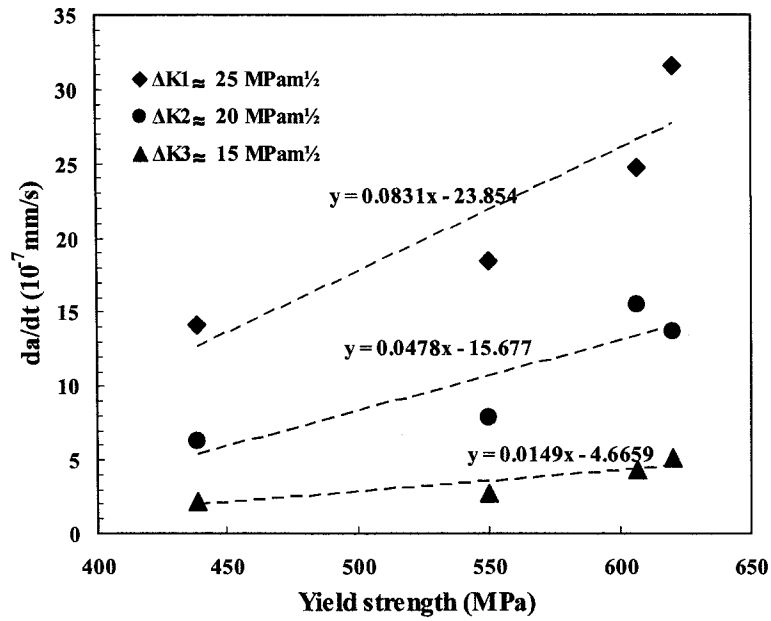
Figure 4-31 Crack growth rates (mm/s) against yield strength of the pre-strained samples at different ΔK_I conditions in near-neutral pH environment.

From the slopes of the trend lines of each loading stage in Figure 4-31, with the yield strength increasing, the increase rate of crack growth velocity under $\Delta K_I \approx 25$ MPa$\sqrt{m}$ was 8 times to that under $\Delta K_I \approx 15$ MPa$\sqrt{m}$. It implies that more severe loading condition gave much greater crack growth rate increase with higher yield strength.

90

4.5 Surface replica test

The first class lever system was employed in this kind of test. Lower applied stress level and lower frequency made it much closer to the service condition of the pipeline steel.

4.5.1 Compressive cyclic stress used for pre-fatigue

The traditional fatigue method used tensile cyclic loading to produce tensile-compressive stress in front of the notch tip (Anderson, 1995), so the crack can be initiated. However, based on the existent experiment condition, the size of the tensile sample as shown in Figure 3-5 in the experimental section is very small. It is not large enough to employ the traditional fatigue method to obtain the pre-crack.

A new fatigue method, compressive cyclic loading, is usually used in ceramic industry to get a pre-crack. It was employed here to create small size pre-cracks. A compressive stress, -90% yield stress of the material, was used as the minimum stress (σ_{min}), and an R ratio of 0.1, a relatively high frequency of 16Hz and a sine wave form were selected to define the loading conditions. For this case, R ratio was defined as: $R = \frac{\sigma_{max}}{\sigma_{min}}$. The principle of the method is shown in Figure 4-32.

(a)   (b)

(c)   (d)
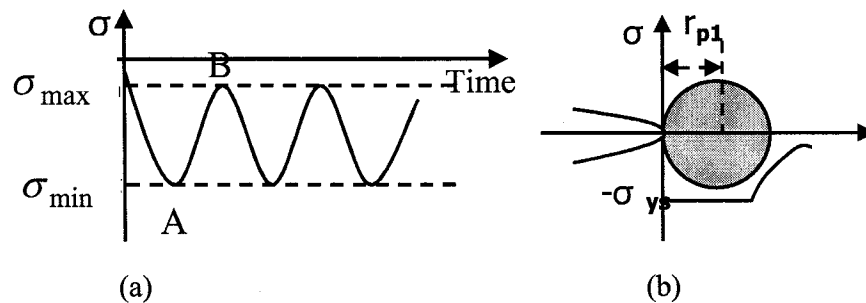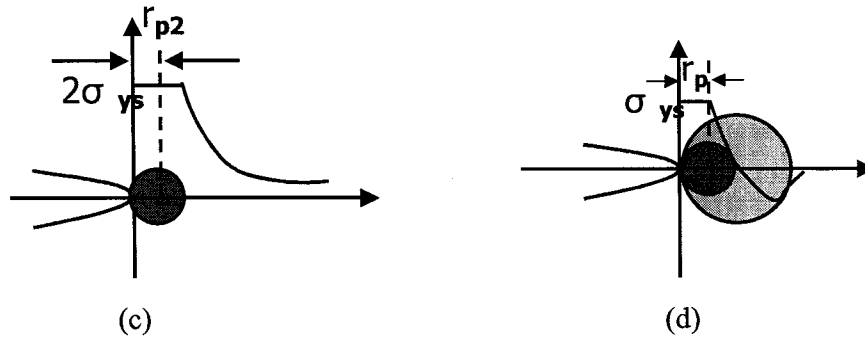
Figure 4-32 Schematic of compressive cyclic stress method for fatigue pre-cracking (a) Compressive loading (b) Stress field and plastic zone at the notch tip when the material is loaded to point A, K_{min} (c) Stress field and plastic zone at the notch tip when the material is loaded to point B, K_{max} (d) Stress field and plastic zone at the notch tip after unloading.

The angle of the notch in the tensile specimen is $60°$, and the radius of the notch is 0.42 mm, so it is not very blunt, the method for analyzing a crack can be roughly used here.

At the notch tip, according to the stress field equation

$$\sigma_y = \frac{k}{\sqrt{2\pi r}} \qquad \text{-------------------------------------4-2}$$

as $r \to 0$, $\sigma_y > \sigma_{ys}$ (or $\sigma_y > 3\sigma_{ys}$), there will be a small scale yielding, a plastic zone forms at the notch tip.

When the sample is loaded to point A (K_{min}), the estimated radius of the plastic zone size can be expressed as Equation 4-3

$$r_{p1} = \frac{(K_{min})^2}{2\pi(-\sigma_{ys})^2} \qquad \text{-------------------------------------4-3}$$

the notch tip is in compressive stress field, as shown in Figure 4-32 (b). Following an approach proposed by Rice (Rice, 1967), the reverse plasticity could be analyzed by

92

means of the Dugdale-Barenblatt strip yield model; the advantage of this model is that it permits superposition of loading and unloading stress fields. When the sample is unloaded to point B (K_{max}), the material near the notch tip exhibits reverse plasticity, the effective yield stress for reverse yielding is $2\sigma_{ys}$, since the material in the plastic zone must be stressed to σ_{ys} from an initial value of $-\sigma_{ys}$. So a tensile stress intensity, ΔK can be imposed. Figure 4-32 (c) illustrates the stress distribution and the plastic zone at the notch tip when the material was loaded to point B, the estimated radius of the plastic zone is written as Equation 4-4

$$r_{p2} = \frac{(K_{max})^2}{2\pi(2\sigma_{ys})^2} \text{-------------------------------------4-4}$$

Because of the redistribution of stress upon unloading, part of the material that was previously in the monotonic compressive plastic zone is now in tension, as shown in Figure 4-32 (d), and hence a pre-crack can be created.

The pre-crack lengths of various amounts of pre-strained samples are shown in Table 4-4. During fatigue, the crack came out on the two side surfaces of the sample. Crack 1 was the length on one side surface and crack 2 was the length on the other surface, the actual crack length could be considered as the average of these two lengths. From Table 4-4, the length difference on two sides was less than 20 μm. The 4% sample had the largest pre-crack length, which was 254.2 μm. It was followed by the 8% sample with 250.5 μm long pre-crack and the 10% sample had the smallest pre-crack with a length of 218.8 μm.

Table 4-4 Pre-crack lengths of various amounts of pre-strained samples

Sample ID	4%	8%	10%
Crack 1 (μm)	255.4	252.6	213.4
Crack 2 (μm)	253.0	248.4	224.2
Average (μm)	254.2	250.5	218.8

93

4.5.2 Maximum applied stress determination

In order to determine the appropriate maximum stress applied on the double-notched tensile sample, the stress concentration factor should be calculated prior to conducting the SCC test.

Figure 4-33 is the schematic drawing of double-notched tensile sample showing the meaning of the symbols used in the following calculation. From Pilkey's book (Pilkey, 1997), for a flat tension bar with opposite V-shaped notches, the theoretical stress concentration factor, $K_{t\alpha}$, could be obtained from Equation 4-5 if $2t/H=0.398$ and α <90°. For this specific case, $2t/H=2\times1.25/6=0.416$, it is very close to 0.398 and $\alpha=60°<90°$, so the $K_{t\alpha}$ could be calculated based on Equation 4-5.
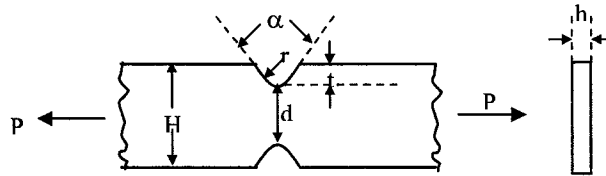
Figure 4-33 Schematic drawing of a double-notched tensile sample

$$K_{t\alpha}=K_{tu} \quad \text{------------------------------------- 4-5}$$

Where K_{tu} is the stress concentration factor for U-notched flat tensile bar with the same geometry except $\alpha=0°$.

Since $t/r=1.25/0.6=2.08$, it is in the range 2.0~50.0, for U-notched bar, K_{tu} can be calculated by Equation 4-6 (Pilkey, 1997):

$$K_{tu}= \ C_1 + C_2\left(\frac{2t}{H}\right) + C_3\left(\frac{2t}{H}\right)^2 + C_4\left(\frac{2t}{H}\right)^3 \text{----------------------4-6}$$

94

$$C_1 = 1.037 + 1.991\sqrt{\frac{t}{r}} + 0.002\frac{t}{r}$$

$$C_2 = -1.886 - 2.181\sqrt{\frac{t}{r}} - 0.048\frac{t}{r}$$

Where
$$C_3 = 0.649 + 1.086\sqrt{\frac{t}{r}} + 0.142\frac{t}{r}$$
and H= 6mm

$$C_4 = 1.218 - 0.922\sqrt{\frac{t}{r}} - 0.086\frac{t}{r}$$

From Equations 4-5 and 4-6, the stress concentration factor, $K_{t\alpha}$, at the notch tip finally can be estimated to be 2.19.

From Sections 4.3 and 4.4, the yield stresses for the 4%, 8% and 10% samples tested in near-neutral pH environment were 541 MPa, 607 MPa and 620 MPa respectively. In the field, all the pipelines were designed to operate in the elastic stress range of the steel. In order to simulate this service condition, the maximum load applied on the samples was 5.49 kN, which corresponded to a nominal stress (σ_{nom}) of 228.75 MPa on the un-notched flat sample. Because of the stress concentration at the notch tip, the actual stress on the cross section of the notch surface was 501 MPa ($K_{t\alpha}\cdot\sigma_{nom}$), it was estimated of 92%, 83% and 81% of the yield strength of the 4%, 8% and 10% samples.

4.5.3 Crack growth length measurement

In order to measure the crack growth length, the test was interrupted weekly and the acetate replica was used to obtain the crack morphology. Pictures in Figure 4-34 are representatives of crack morphologies observed under OM.
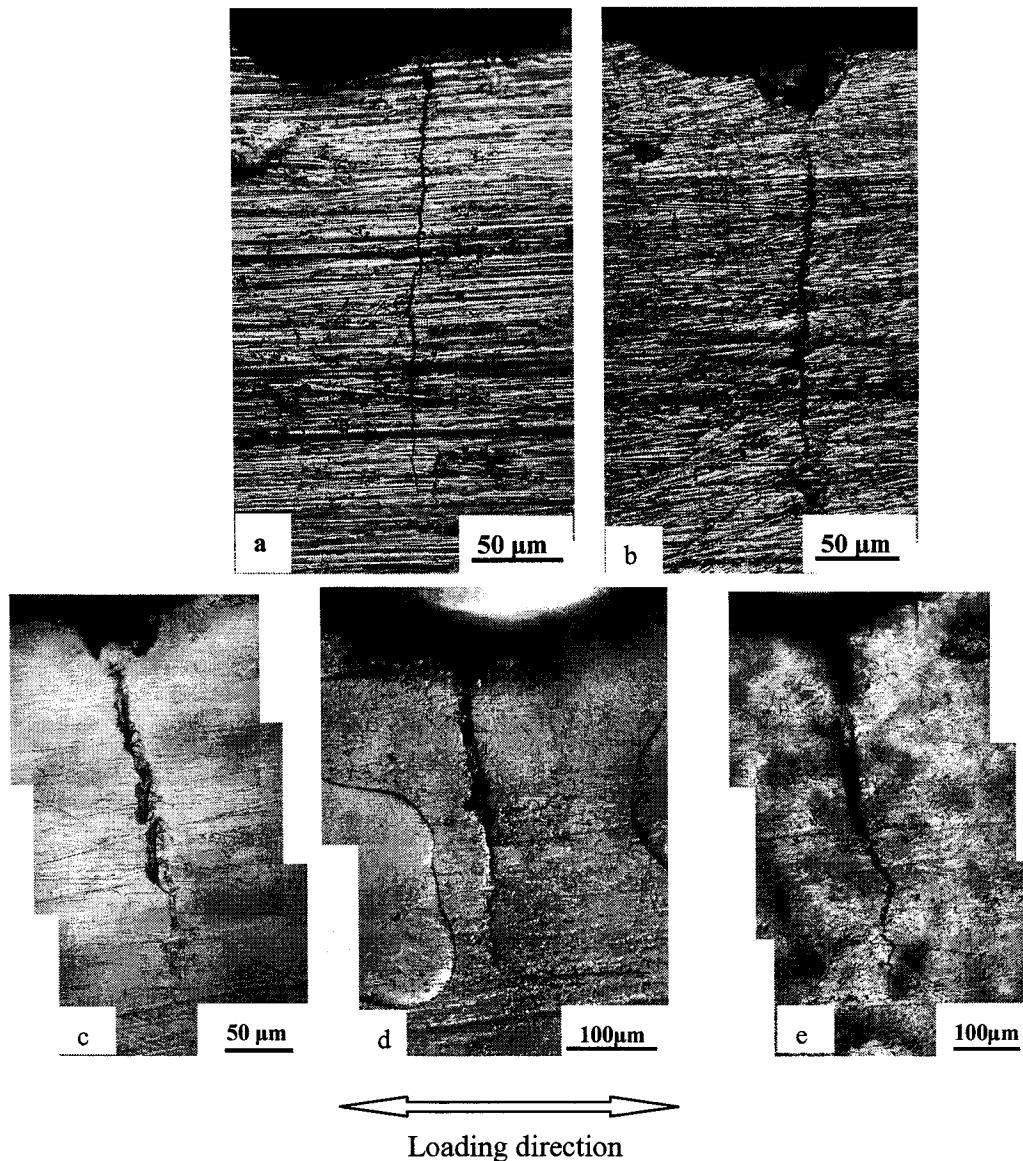
Figure 4-34 Crack morphologies of the 8% pre-strained sample during surface replica test (a) the original pre-crack, (b) one-week crack, (c) two-week crack, (d) four-week crack, (e) five-week crack

The path of pre-crack was transgranular and most pre-cracks tended to show some meandering. When the sample was subjected to C1 solution and cyclic loading, the crack was still transgranular but it became wider and was filled with corrosion products, because anodic dissolution during the SCC process in near-neutral pH environment occurred not only at the crack tip but also on the crack walls. However, since the dissolution rate at the tip was high enough, the crack tip was still kept

96

extremely sharp. All of these were shown in Figure 4-34, the crack changed from a relatively narrow one (Figure 4-34 (a)) to a much wider one after the sample experienced some SCC (Figure 4-34 (b)-(e)). Therefore, other than the width, there was no significant difference in crack morphologies between the pre-crack and subsequent crack experienced some SCC growth, since both were transgranular.

The OM measurements gave crack growth length after seven days of the 4% sample as 14.7 μm, while for the 8% sample it was 18.6 μm, and for the 10% sample it was 34.4 μm, as shown in Figure 4-35. One thing should be noted here is that in most cases, different amounts of SCC growth were observed on two surfaces on the opposite side of the same crack, possibly because of non-uniformity of the crack arrest, sometimes at MnS particles (Ahmed et al., 1997). So, the crack growth lengths were measured on both sides and the average was used for the subsequent calculation.
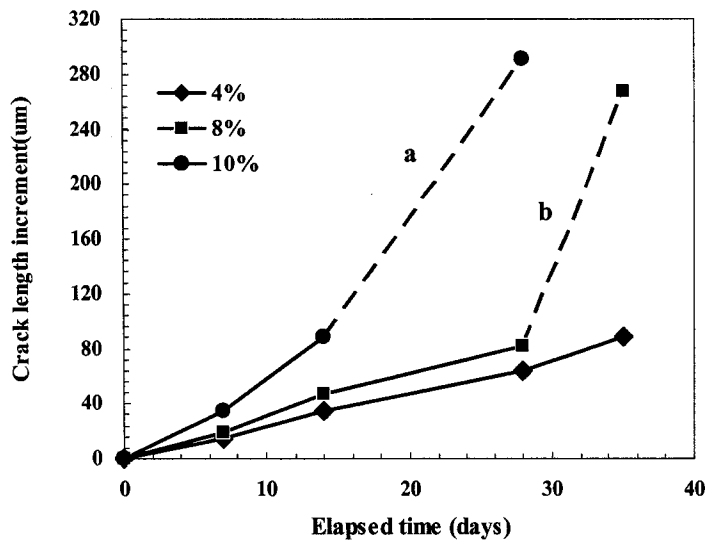
Figure 4-35 Crack length increment with time of surface replica tests

In the second week, the cracks on the 4%, 8% and 10% samples all showed continuous growth and the crack length increment order did not change. But the crack

growth rates, which were indicated by the slopes of the crack length increment curves, started to increase.

The crack length increment of the third and fourth week was still in the same order, 29.4 μm was for the 4% sample, 34.3 μm for the 8% sample, but the 10% sample had an extremely large crack length increment of 202.5 μm as shown by the dashed line "a" in Figure 4-35. This could be ascribed to the fact that at the beginning of the third week, the actual stress at the notch cross section of the 10% sample was 452.50 MPa (calculated based on Equation 3-4), but the stress for plastic collapse was just 310.23 MPa. Plastic collapse could occur before the stress intensity factor reached the fracture toughness, which was around 90 MPa $\sqrt{m}$. This was confirmed by the fourth week's measurements, the crack length for the 10% sample was 509.7 μm, $K_{I, max}$ was 35.0 MPa $\sqrt{m}$ and the sample failed after 30 days.

In the fifth week, the crack growth length of the 4% sample was a little longer, 24.19 μm and $K_{I, max}$ was 29.3 MPa $\sqrt{m}$; the 8% sample had a relatively larger growth length 186.1 μm (the dashed line "b" in Figure 4-35) and $K_{I, max}$ was 33.8 MPa $\sqrt{m}$. Finally, the 8% and 4% samples failed respectively after 45 days and 47 days by plastic collapse.

It is seen that the crack growth rate of the 10% sample was larger than those of the 8% sample and the 4% sample.

4.5.4 Quasi-cleavage on the fracture surface

Following the OM examination, in order to further clarify the crack characteristics, the cracks were broken open in liquid nitrogen to observe the fracture surfaces. SEM fractographs were taken for all the failed samples. Figure 4-36 is representative of all

98

the samples. The crack growth direction, the machined notch tip and the pre-crack boundary are indicated in Figure 4-36 (a).
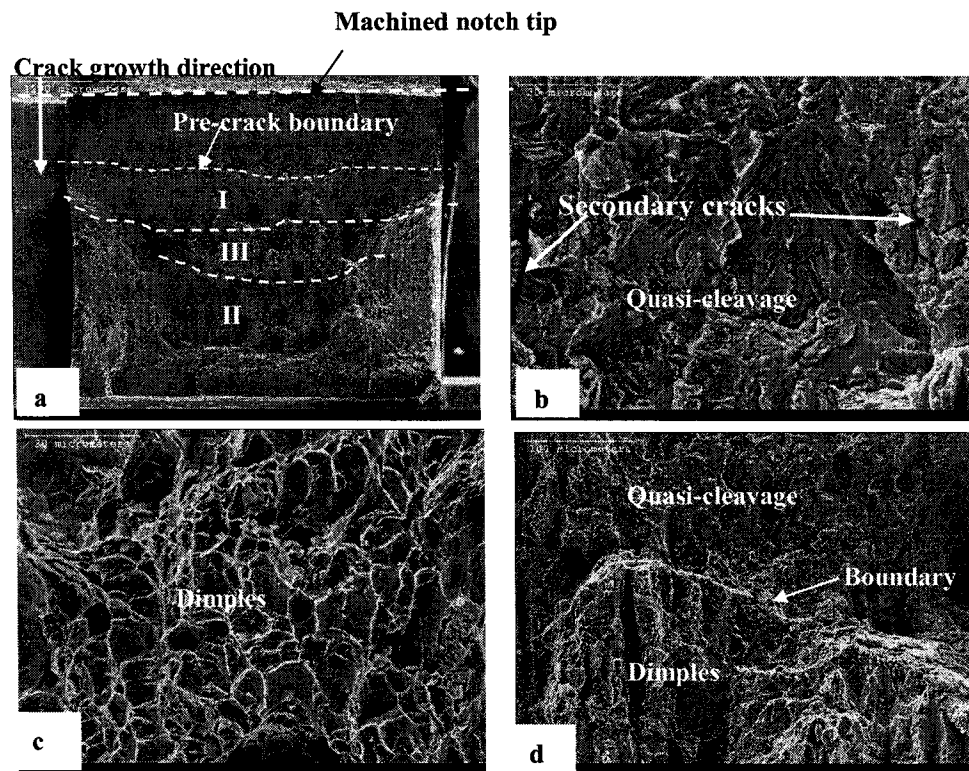
Figure 4-36 SEM fractographs showing fracture surface of the 8% pre-strained sample (a) the panorama of the fracture surface, (b) edge, quasi-cleavage, (c) Middle, dimples, (d) Boundary, transition from quasi-cleavage to ductile fracture.

SEM observation found that the samples typically displayed characteristics of SCC on the fracture surfaces. As shown in region I in Figure 4-36 (a), SCC readily occurred at the edge of the fracture surface, some parts of which displayed quasi-cleavage and secondary cracks, the enlarged image was shown in Figure 4-36 (b). In the middle part of the fracture surface, dimples were found, as shown in region II in Figure 4-36 (a). Figure 4-36 (c) is the enlarged image from region II, showing the traditional ductile fracture features. Region III in Figure 4-36 (a) contains the boundary lines of the fracture mode transition from quasi-cleavage to ductile fracture, and the specific transition line, quasi-cleavage and ductile features are shown in Figure 4-36 (d).

99

Similar fracture morphologies were seen in the other samples, the SEM pictures of the 4% and 10% samples showing the quasi-cleavage features are shown in Figures 4-37 and 4-38.
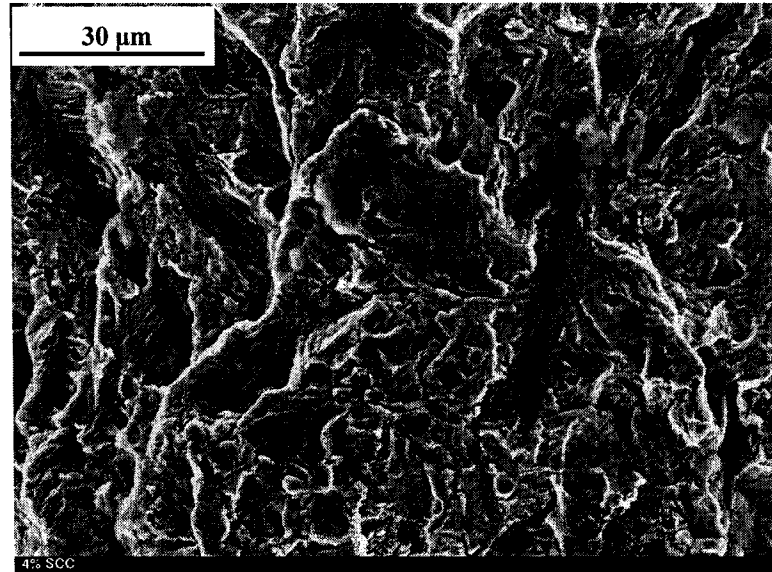
Figure 4-37 Fracture surface of the 4% sample showing quasi-cleavage
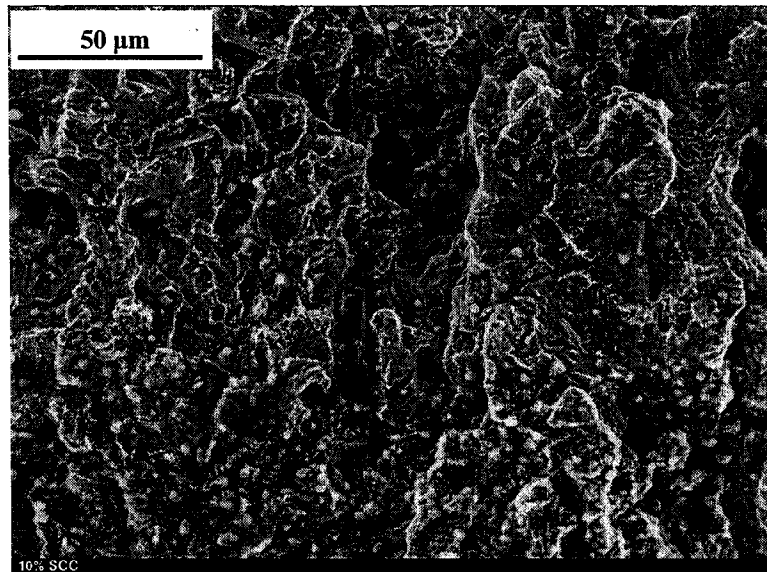
Figure 4-38 Fracture surface of the 10% sample showing quasi-cleavage

(There are nodules of $CaCO_3$ in the lower edge of this picture,

which are unrelated to the quasi-cleavage process)

100

It is well known that the development of near-neutral pH SCC is influenced by the loading conditions and the presence of a critical environment at the crack tip. All of the above results indicate that near-neutral pH SCC had been generated with a maximum stress of around 90% of the yield stress of the material, a loading frequency of 50 cycles/day (5.8×10^{-4} s^{-1}) and an R ratio of 0.2.

4.5.5 Crack growth rate

After getting the crack increment weekly, the growth rate can be estimated by dividing by the test periods. Figure 4-39 illustrates the crack growth rates of various amounts of pre-strained samples.
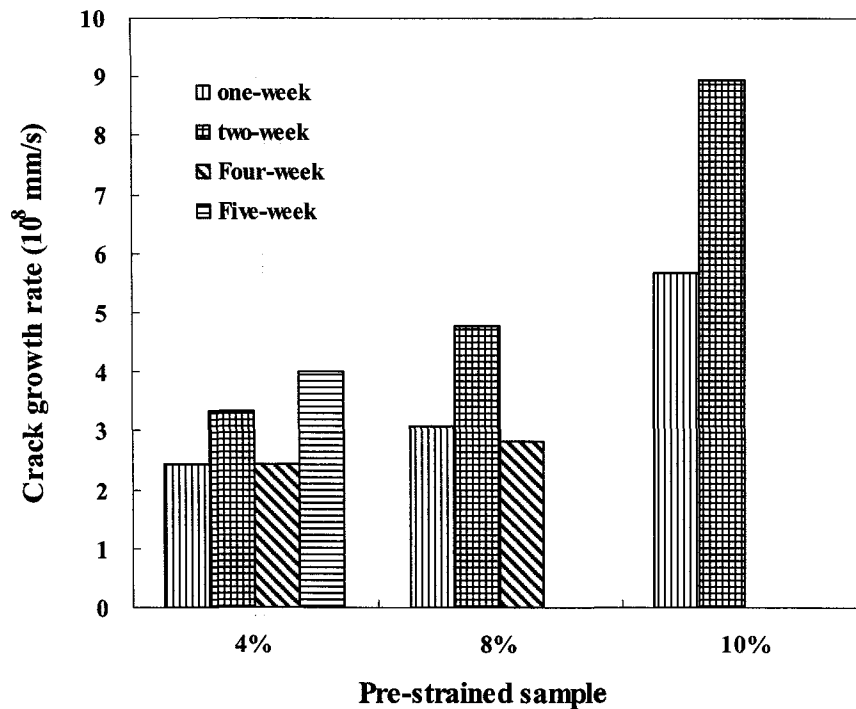
Figure 4-39 Crack growth rates of various amounts of pre-strained samples under the same cyclic loading condition in near-neutral pH environment.

Parkins *et al.* conducted similar experiments, but on smooth tensile samples (as received X-65). Under cyclic loading conditions in NS4 solution which was bubbled with 5%CO_2+N_2 gas mixture to achieve a pH ~6.5 at OCP, a mean crack growth rate

101

in the range of 7.5×10^{-9} to 1.86×10^{-7} mm/s was obtained (Parkins et al., 1994). From Figure 4-41, the crack growth rate was found to be in the range of 2.4×10^{-8} to 3.1×10^{-7} mm/s, so it fell in the same range as Parkins' results. The observed difference might be due to a difference in the microstructure present in the material used to carry out the tests. X-52 pipeline steel, for instance, had the pearlite-ferrite microstructures while X-65 steel possessed mostly ferritic grains with some banded pearlite structures. It was pointed out by Lu and Luo. (Lu and Luo, 2004) that the increase in pearlite content in the microstructures had a detrimental effect on the SCC performance. And also, it was expected that the C1 test solution would be more aggressive than NS4 solution (Chen et al., 2004), which probably would assist the crack growth.

The relative SCC susceptibility was determined from the crack growth rate curve in Figure 4-39. The high-to-low sensitivity ranking of the material to near- neutral pH SCC was therefore found to be 10% > 8% >4%.

4.6 Effect of cold work on SCC susceptibility

The results of sections 4.3, 4.4 and 4.5 all support the contention that the cold work increases the material's susceptibility to near-neutral pH SCC. It can be explained from two perspectives in relation to near-neutral pH SCC: the ingress of hydrogen and anodic dissolution.

4.6.1   Enhanced enrichment of hydrogen

The major effect of cold work is the increase of the number of dislocations, the dislocation density in a metal that has been highly deformed may be as high as 10^{10} mm^{-2} (Hertzberg, 1983). This would be expected to produce a decrease in hydrogen diffusivity, an increase in the number of hydrogen trapping sites (Xie and Hirth, 1982) and an increase of hydrogen adsorption coverage on the surface. The effects are inter-related since the cold work increases the number of dislocations, which could trap more hydrogen as a result of increased trapping, and decreases the diffusivity of hydrogen in steel, these two should promote more hydrogen absorption into the steel (Huang and Shaw, 1995).

The increase of dislocation density would produce an increase of the yield stress, which increases the stress fields around the crack tip. This means that hydrogen is more likely enriched at the crack tip. This enrichment is due to the fact that hydrogen is attracted to the crack tip in proportion to the hydrostatic stress parameter p, which is the sum of the principal stresses. Gu et al. (Gu et al., 1999) also suggested that hydrostatic stress could induce more hydrogen accumulation. On the other hand, the higher yield strength could produce smaller plastic zone size at the crack tip and lower ductility. This combination would produce more cracking in near-neutral pH environment.

4.6.2 Accelerated anodic dissolution

On the other hand, when steels are plastically deformed, some fraction of the deformation energy, approximately 5%, is retained internally. The major portion of

103

this stored energy is as strain energy associated with dislocations (Hertzberg, 1983). The increase in the amount of strain energy would allow easier dissolution on specific sites. This causes an increase in the corrosion rate with an increase of in the amount of cold work.

In addition, when hydrogen is trapped in the defects in steel, the lattice is dilated and the interatomic cohesion is decreased. It has been estimated that, 1% hydrogen concentration could reduce the atomic bonding energy by 5% for steels (Chen and Jack, 1997). So, absorbed hydrogen can accelerate the corrosion process (Gu et al., 1999 and Bulger, 2000).

104

5 Conclusions and Recommendations

5.1 Main conclusions

The following is the summary of major findings based on the experimental results and discussion:

1. The cold worked X-52 pipeline steel tested in near-neutral pH environment had increased yield strength and hardness due to the strain hardening effect. However, the ductility of the cold worked material was reduced.

2. The OCP of X-52 pipeline steel measured in the deaerated C1 solution was in the range of $-730 \sim -760$ mV (SCE), and it appeared not to be sensitive to the prior plastic deformation. However the corrosion current density increased with the amount of prior plastic deformation when the steel was exposed to near-neutral pH environment.

3. Cyclic stress in the elastic range of the steel increased the corrosion rate of the steel in near-neutral pH environment.

4. Compressive cyclic stress method can be used to fatigue pre-crack in steel. Relatively short pre-cracks (200-300 μm) were successfully produced on small size samples.

5. More severe loading condition gave much higher SCC velocity.

6. Plasticity had a significant effect on the susceptibility of X-52 pipeline steel to near-neutral pH SCC; the material with more plastic deformation had higher SCC velocity.

5.2 Recommendations for future work

1. This research has focused on the influence of cold work on crack propagation behavior. But its effect on crack initiation is still unknown. So a recommendation is made to investigate the cold work effect on crack initiation by using cyclic loading machine to simulate the service condition of pipeline steels. Then a complete conclusion about the effect of cold work can be drawn.

2. Since only one type of steel is tested, we cannot be certain that if the effect

extends to all classes of pipeline steel. Other tests conducted on different types of pipeline steel are therefore suggested.

3. The crack growth length was measured by interrupting the test in the replica technique, which presumed the interruption had no effect on the subsequent crack growth behavior, which is possibly not true. Hence the potential drop test results are regarded as more reliable and that technique is recommended.

6 References

1. Agatonovic R., Plumtree A. and Lambert S.B., "SCC Crack Growth Rates", Final Report, URIF Report, Waterloo, Ontario, 1993

2. Agatonovic R., Plumtree A. and Lambert S.B., "SCC in Pipeline steels: Orientation and Material Effects", Report to Nova Gas Transmission, Ltd., 1994

3. Ahmed T.M., Lambert S.B., Sutherby R. and Plumtree A., "Cyclic Crack Growth Rates of X-60 Pipeline Steel in a Neutral Dilute Solution", Corrosion, Vol.53, No.7, 1997

4. Anderson T.L, *Fracture Mechanics: Fundamental and Applications*, 2nd ed., CRC Press, 1995

5. Arrigoni B. and Sinigaglia E., "Transverse SCC in a Landslide Area", P/L Operations & Materials 2067, pp10-1, 10-10, April 7-11, 1997

6. Baker, Stress Corrosion Cracking Study, FINAL REPORT, Integrity Management Program Delivery Order DTRS56-02-D-70036, Submitted by: Michael Baker Jr., Inc., January 2005

7. Bardes B. (Editor), *Metals Handbook: Properties and selection: Irons and Steels*, Vol.1, 9th edition, American Society for Metals, pp 221, 1978

8. Beavers J.A., Durr C.L. and Shademan S.S., "Mechanistic studies of near-neutral-pH SCC on underground pipelines", *Materials for Resource Recovery and Transport*, Edited by L. Collins, The Metallurgical Society of CIM, 1998

9. Beavers J.A. and Harle B.A., "Mechanisms of High-pH and Near-neutral pH SCC of Underground Pipelines", *Proceedings of the 1st International Pipeline Conference*, Edited by Yoon M., Mensik M. and Mohitpour M. pp 555-564, 1996

10. Beavers, J.A. and Hagerdorn, E.L., "Near-Neutral pH SCC: Mechanical Effects on Crack Propagation," 9th Symposium On Line Pipe Research, PRCI, Arlington, VA, 1996.

11. Brongers M.P.H., Beavers J.A., Jaske C.E., "Cracks during Simulated Hydrostatic Testing", International Pipeline Conference, Vol.2, pp 743, ASME 2000

12. Brongers M.P.H., Beavers J.A., Jaske C.E. and Delanty B.S., "Effect of Hydrostatic Testing on Ductile Tearing of X-65 Line-pipe Steel with Stress-corrosion Cracks", Corrosion 2000, Paper No. 00355, 2000

13. Brown B.F., "SCC in high strength steels and in Titanium and Aluminium alloys", Naval Research Laboratory, U.S. Gov't printing office, Washington, pp 2, 1972

14. Bulger J.T., "The Effect of Microstructure on Near-neutral pH SCC", University of Alberta, Thesis, pp 137-139, 2000

15. CEPA. *Submission to the National Energy Board*, Proceeding MH-2-95, Vol. 2, Appendix D, Tab 1, 8, 1996

16. Chen W., Eadie R.L. and Sutherby R.L., "Environmental effects on near-neutral pH SCC in pipelines", Environment-induced cracking of metals, 2nd internl conf. September 19-2, 2004

17. Chen W., Jack T.R., Wimott M.J., "Environmental aspects of near-neutral pH SCC of pipeline steel", Metallurgical and Materials Transactions, Vol. 33A, pp 1429-1436, May, 2002

18. Chen X. and Gerberich W.W., "The Kinetics and Micromechanics of Hydrogen-assisted Cracking in Fe-3 pct Si Single Crystals", Metal. Trans. A, 22A, pp 59-71, 1991

19. Chen W. and Jack T.R., *Internal Report*, No.01225, Nova Research & Technology Center, Calgary, December 1997

20. Chen W., King F., Jack T.R. and Wilmott M.J., "Hydrogen Permeation Behavior of X-70 Pipeline Steel in a Near-neutral pH Soil Environment, 2000 International Pipeline Conference, Vol.2, pp953-960, 2000

21. Chen W., King F., Jack T.R. and Wilmott M.J., "Environmental Aspects of Near-neutral pH SCC of Pipeline Steel", Metallurgical and Materials Transactions A, Vol. 33A, P 1429-1436, May, 2002 (1)

22. Chen W., King F. and Vokes E., "Characteristics of Near-neutral pH Stress Corrosion Cracks in an X-65 Pipeline", Corrosion, Vol. 58, No 3, pp

267-275,2002 (2)

23. Chen W.X. and Wang S.H., "Room Temperature Creep Behavior of Pipeline Steels and Its Influence on SCC", 4th International Pipeline Conference, IPC 2002-27273, 2002

24. Davis J.R.ed., *Metals Handbook*, Disk Edition, ASM International, 1998.

25. Delanty B.S. and O'Beirne J., Oil and Gas J., p 39, June 1992

26. Devanathan M.A.V. and Stachuiski Z., Proc. Royal Soc. 270 P 33, 1962

27. Elboujdaini M., Wang Y.-Z and Revie R.R., "Initiation of SCC on X65 Linepipe Steel in Near Neutral pH Environment", Proc. 2000 Intern. Pipeline Conf. 2, pp 967, 2000(1)

28. Elboujdaini M., Wang Y.-Z, Revie R.R., Parkins R.N. and Schhata M.T., "Stress Corrosion Crack Initiation Processes: Pitting and Microcrack Coalescence", Corrosion' 2000, Paper No. 379, 2000(2)

29. Delanty B.S. and O'Beirne J., Oil and Gas J., p 39, June 1992

30. Devanathan M.A.V. and Stachuiski Z., Proc. Royal Soc. 270 P 33, 1962

31. Gu B., Luo J., Mao X., "Hydrogen-facilitated Anodic Dissolution-type SCC of Pipeline Steels in Near-neutral pH Solution", Corrosion, January, Vol.55, No.1, pp 96-106, 1999 (1)

32. Gu B., Yu W.Z., Luo J.L. and Mao X., "Transgranular SCC of X-80 and X-52 Pipeline Steels in Dilute Aqueous Solution with Near-neutral pH", Corrosion, pp 312-318, 1999(2)

33. Gu, J. and Yu, L.Y., "The Influence of Geometric Factors on Crack Depth Measurement Using the Potential Drop Technique", NDT International, Vol. 23, No. 3, pp 161-164, 1990

34. Gutman G.M., *Mechanochemistry of Metals and Corrosion Protection*, Metallurgiya, Moscow, 2nd Ed., 1981

35. Hall, R.J. and McMahon M.C., *"SCC Study"*, General Physics Corporation for U.S. Department of Transportation, Research and Special Programs Administration, Office of Pipeline Safety. Report No.DTRS56-96-C-0002-004, 1999

109

36. Harle B.A. and Beavers J.A., " Low-pH Stress Corrosion Crack Propagation in API X-65 Line Pipe Steel", Corrosion Vol. 49, No.10, pp 861-863, 1993

37. Harle B.A., Beavers J.A. and Jaske C.E., "Low-pH SCC of Natural Gas Pipelines", Corrosion 94, Paper No. 242, 1994

38. Hertzberg R.W., *Deformation and Fracture Mechanics of Engineering Materials*, 2nd edition, pp61-70, 1983

39. Huang H. and Shaw W.J.D, "Cold work effects on sulfide stress cracking of pipeline steel exposed to sour environments", Corrosion Science, Vol. 34(1), pp 61-78, 1993

40. Huang H. and Shaw W.J.D., "Hydrogen Embrittlement Interactions in Cold-Worked Steel", Corrosion, Vol.51, No.1, pp 30-36, 1995

41. Jaske C.E. and Beavers J.A., "Review and Proposed Improvement of a Failure Model for SCC of Pipelines", International Pipeline Conference, Vol. 1, pp 439-444, ASME 1998

42. Johnson H.H. "Calibrating the Electric Potential Method for Studying Slow Crack Growth", Materials Research & Standards", Vol.5, No.9, pp442-445, 1965

43. Jones R. H., *Stress-Corrosion Cracking*, chapter 1,2 and 17, Materials Park, Ohio, ASM international, 1992

44. Keh A.S., "Dislocation Arrangement in Alpha Iron During Deformationand Recovery," in Direct Observation of Imperfection in Crystal, eds. J.B. Newkirk, J.H. Wernick (New York, NY: Interscience Publishers), pp 213, 1962

45. Kuniya J., Anzai H. and Masaoka I., "Effect of MnS Inclusions on SCC in Low-Alloy Steels", Corrosion, Vol. 48, No.5, pp 419, 1992

46. Lambert S.B., Beavers J.A., Dalanty D., Sutherby R. and Plumtree A., "Mechanical Factor Affecting Stress Corrosion Crack Growth Rates in Buried Pipelines", International Pipeline Conference, Vol. 2, ed, Ellwood J.R., pp 961, ASME 2000

47. Leis B.N., "Update on SCC life prediction models for pipelines", First Pipeline Technology Conference, Ostende, Belgium, 1990

48. Lian K. and Meletis E.I., "Environment-induced Deformation Localization During

Transgranular SCC", Corrosion, Vol.52, No.5, 1996

49. Liberta S.D. and Gaberta G., "SCC by Anodic Dissolution and Hydrogen Permeation in Pipeline Steels", Materials Science, 33, P411, 1997

50. Lu B.T. and Luo J.L., "A Mechanistic Study on Mechanism of Near-neutral pH SCC of Pipeline Steel", Environmental-Induced Cracking of Metals, 2nd International Conference, Baff, AB, Canada, 2004.

51. Lu B.T., Luo J.L. and McCrady B., "Near-Neutral pH SCC Initiation and Early Propagation of X70 Pipeline Steel", International Pipeline Conference, IPC2002-27234, 2002

52. Mao S.X, Gu B., Wu N.Q. and Qiao L., "The Mechanism of Hydrogen-facilitated Anodic-dissolution type SCC: Theories and Experiments", Philosophical Magazine A, Vol. 81 No.7, pp1813-1831, 2001

53. McIntyre P., "Advanced Methods for Monitoring Fatigue Crack Growth", Journal of the Society of Environmental Engineers, pp3-7, 1974

54. Misra R.D.K., Hartmann J.E. and Boucek A.J., "Development of an Ultrahigh Strength Hot Rolled Steel", I &SM, 63, August, 2000

55. Nakai, Y. and Wei, R.P., "Measurement of Short Crack Lengths by an A.C. Potential Method", *Engineering Fracture Mechanics*, Vol. 32, No.4, pp 581-589, 1989

56. National Energy Board, "SCC on Canadian Oil and Gas Pipelines," Calgary, Alberta, Canada, Report # MH-2-95, Nov. 1996

57. Parkins R.N. and Greenwell B.S., "The Interface between Corrosion Fatigue and Stress-Corrosion cracking", Metals Science, 11, 405, 1977

58. Parkins R.N., "Investigations Relating to Environment-Sensitive Fracture in the TransCannada Pipeline System", Report to TransCanada Pipe Lines, 1988

59. Parkins R.N., "Overview of Intergranular Stress Corrosion Cracking Research Activities", Report PR-232-9401 to PRCI at the America Gas Association, November, 1994

60. Parkins R.N., Blanchard Jr W.K. and Delanty B.S., "Trangranular SCC of High-pressure Pipelines in Contact with Solutions of Near Neutral pH, Corrosion,

50, pp 394-410, 1994

61. Parkins R.N., "Hydrogen Diffusivity in Pipeline Steel Exposed to Near Neutral pH Solutions" Progress Report 1, 1997

62. Parkins R.N., "The Influence of Hydrogen on Crack Growth in Pipelines", Materials for Resource Recovery and Transport, ed. L. Collins, Met. Soc. Of CIM, pp 35-49, 1998 (1)

63. Parkins R.N., "Hydrogen Diffusivity in Pipeline Steel Exposed to Near-neutral pH Solutions", Report to Gas Research Institute, April 1998 (2)

64. Parkins R.N., "Intergranular and Transgranular SCC of High Pressure Gas Pipelines - Similarities and Differences", in Proceedings of NACE Northern Area Eastern Conference, Ottawa, Ontario, Canada, pp1-22, Oct. 24-27, 1999

65. Parkins R.N., "A Review of SCC of High Pressure Gas Pipelines", Corrosion 2000, Paper No. 00363, 2000

66. Pilkey A.K., "Experimental Investigations of Classical and Nonclassical SCC in Pipeline Steel", Master thesis, University of Waterloo, 1992

67. Pilkey A.K., Lambert S.B. and Plumtree A., "SCC of X-60 Line Pipe Steel in a Carbonate-Bicarbonate Solution", Corrosion, Vol.51, No.2, pp91-96, 1995

68. Pilkey W.D., *Peterson's Stress Concentration Factors*, 2nd ed., Chapter 2, pp 60-87, 1997

69. Plumtree A., Lambert S.B. and Sutherby R., "Crack Growth in Stressed Pipeline Steel in NS4 Solution", Paper No.6.2, NACE Northern Area Eastern Conference, Oct.24-27, 1999

70. Pugh E.N, "Progress Toward Understanding the Stress Corrosion Problem", Corrosion 41,9 pp517, 1985

71. Qiao L.J, Luo J.L. and Mao X., "The Role of Hydrogen in the Process of SCC of Pipeline Steels in Dilute Carbonate-bicarbonate Solution", Journal of Materials Science Letters, Vol.16, pp 516-520, 1997

72. Rebak R.B., Xia Z., Safruddin R. and Szklarska-Smialowska Z., "Electrochemical Process Controlling SCC of Underground Pipelines", Corrosion 95, Paper No.184, 1995

112

73. Rice J.R., "A path Independent Integral and the Approximate Analysis of Strain Concentration by Notches and Cracks", J. Appl. Mech., 1967.

74. Scott X.M, Luo J.L., Gu B. and Yu W., "Hydrogen Facilitated Anodic Dissolution Type SCC of Pipeline Steels in Coating Disbondment Chemistry", International Pipeline Conference, Vol.1, pp485-492, ASME 1998

75. Sahal M., Creus J, Sabot R. and Feaugas X., "Consequences of Plastic Strain on the Dissolution Process of Polycrystalline nickel in H2SO4 solution", Scripts Materials, Vol. 51, pp 869-873, 2004

76. Sutcliffe J.M., Fessler R.R. Boyd W.K. and Parkin R.N., "SCC of Carbon Steel in Carbonate Solutions", Corrosion 28, pp 313, 1972

77. Sutherby R.L., "The CEPA Report on Circumferential SCC", International Pipeline Conference, Vol.1, pp 493-503, ASME 1998

78. Szczepanski M., *The Brittleness of Steel*, John Wiley and Sons, London, 1963

79. Szklarska-Smialowska Z., Xia Z. and Rebak R.B., "SCC of X-52 Carbon Steel in Dilute Aqueous Solutions", Corrosion, Vol.50, No.5, pp 334-338, 1994

80. Urednicek M., Lambert S. and Vosikovsky O., "SCC Monitoring and Control" Int. Conf. Pipeline Reliability, Calgary, Cananda, Paper no. 7-2, June 1992

81. Vadhwana N.M. and Chen W., "Effect of Loading History on Hydrogen Content in Pipeline Steels", Proceedings of IPC'02, 4th International Pipeline Conference, pp 1-7, 2002

82. Wang S.H., Chen W., King F. and Jack T.R., "Role of Prior Cyclic loading in the Initiation of Stress Corrosion Cracks on Pipeline Steel Exposed to Near-neutral-pH Environment", Int. Pipeline Conf., Vol.2, ed. J.R. Ellwood, pp 1005, Calgary, Canada: ASME, 2000

83. Wang S.H., Chen W., King F., Jack T.R. and Fessler R.R., "Precyclic-Loading-Induced SCC of Pipeline Steels in a Near-Neutral-pH Soil Environment", Corrosion, Vol.58, No.6, pp526-530, June 2002

84. Wang Y-Z., Revie R.W. and Parkins R.N., "Mechanistic Aspects of Stress Corrosion Crack Initiation and Early Propagation", Corrosion, Paper No.143, 1999

85. William D. and Callister Jr, "Materials Science and Engineering- an Introduction", Six[th] Ed., 2002

86. Wilmott M.J and Diakow D.A., International Pipeline Conference, Vol.1, pp507-524, 573-585, ASME 1996

87. Wilmott M.J. and Sutherby R.L., "The Role of Pressure and Pressure Fluctuation in the Growth of Stress Corrosion Cracks in Line Pipe Steels", International Pipeline Conference, Vol.1, pp409-422, 1998

88. Xie S.X. and Hirth J.P., "Permeation of Hydrogen, Trapping, and Damage in Spheroidized AISI 1090 Steel", Corrosion, Vol. 38, No.9, pp 486-493, 1982

89. Zheng W., Sutherby R., Revie R., Tyson W.R. and Shen G., "SCC of Linepipe Steels in Near-Neutral pH Environment", Issues Related to the Effects of Stress, Corrosion Science, June 2000

90. Zheng W., Macleod F.A., Revie R., Tyson W.R., Shen G., Kiff D., Skaff M. and Wong E.-W., "Recent Progress in Study of Transgranular SCC in Linepipe Steels", In Corrosion Deformation Interactions CDI'96 , ed, pp 282, 1996

91. Zheng W., Macleod F.A., Revie R. W., Tyson W.R., Shen G., Shehata M., Roy G., Kiff D., and McKinnon J., "Growth of Stress Corrosion Cracks in Pipelines in Near-neutral pH Environment: The CANMET Full-Scale Tests-Final Report to the CANMET/Industry Consortium", CANMET/MTL, Ottawa, MTL 97-48(CF), 1997

114

7 Appendices

Effect of straining on anodic current

Experimental details for transient current test

The test was carried out in C1 solution and bubbled with 5% CO_2+N_2 gas mixture. The round tensile sample was sealed in a plastic container, which was the same as used for the Rp tests and potentiodynamic tests, as shown in Figure 3-8 in experimental section. A platinum wire (~99.9% pure) of diameter 0.5mm was used as a counter electrode while the saturated calomel electrode (SCE) was used as the reference electrode. A salt bridge was used at the tip of reference electrode to reduce the solution resistance and the contamination of the testing solutions. All electrodes were connected to a GAMRY potentiostat to generate the output from the corrosion cell.

The INSTRON machine was used to give the loading conditions. Transient current test was carried out under a strain rates of 4.92×10^{-4} s^{-1} and an anodic over-potential of 10 mV. In the test, the anodic current was recorded. In order to check the influence of the corrosion potential on anodic current, the corrosion potential was measured when the sample was loaded under a strain rate of 2.46×10^{-4} s^{-1}.

Results of transient current tests

The corrosion potential testing result, which is shown in Figure 7-1, indicated that the corrosion potential kept constant during the straining process.

115
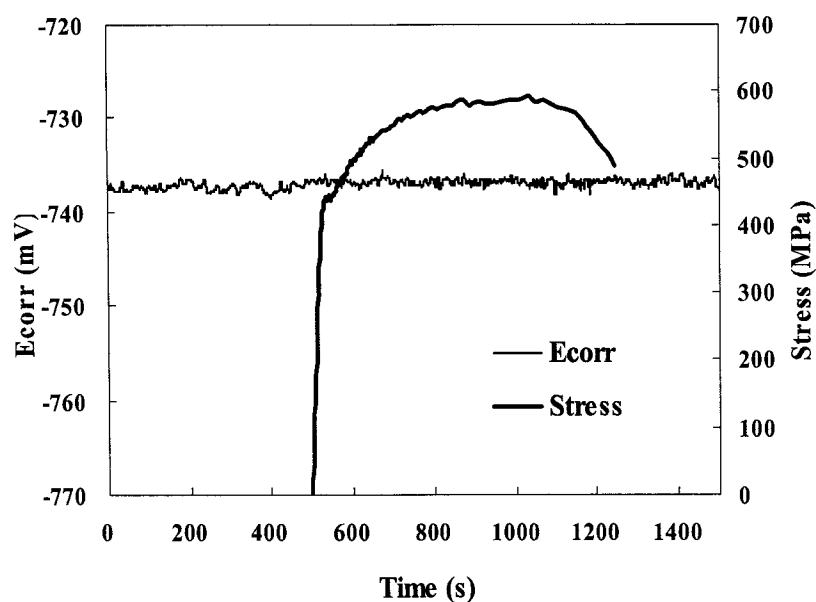
Figure 7-1 Corrosion potential of X-52 steel under a strain rate of 2.46×10^{-4} s^{-1}

Figure 7-2 shows the normalized anodic current change of samples under the interaction of an anodic over-potential, 10 mV, and a strain rate of 4.92×10^{-4} s^{-1}. Before the sample was strained, as shown by the region I in Figure 7-2, the anodic current was stable under the anodic polarization. In the early elastic loading stage, as shown by region II in Figure 7-2, the anodic current kept constant and then in main elastic loading stage and the early plastic loading stage, as defined by region III in Figure 7-2, the anodic currents decreased from 0.15 μA/cm^2 to 0.07 μA/cm^2 within 50 s. The current density decrease would occur if the corrosion potential increased with time during the tensile loading, because the corresponding anodic over-potential, η_A, would decrease. But from Figure 7-1, the corrosion potential was constant. So we cannot presently explain the current drop in the elastic loading range and the early plastic loading stage.

116
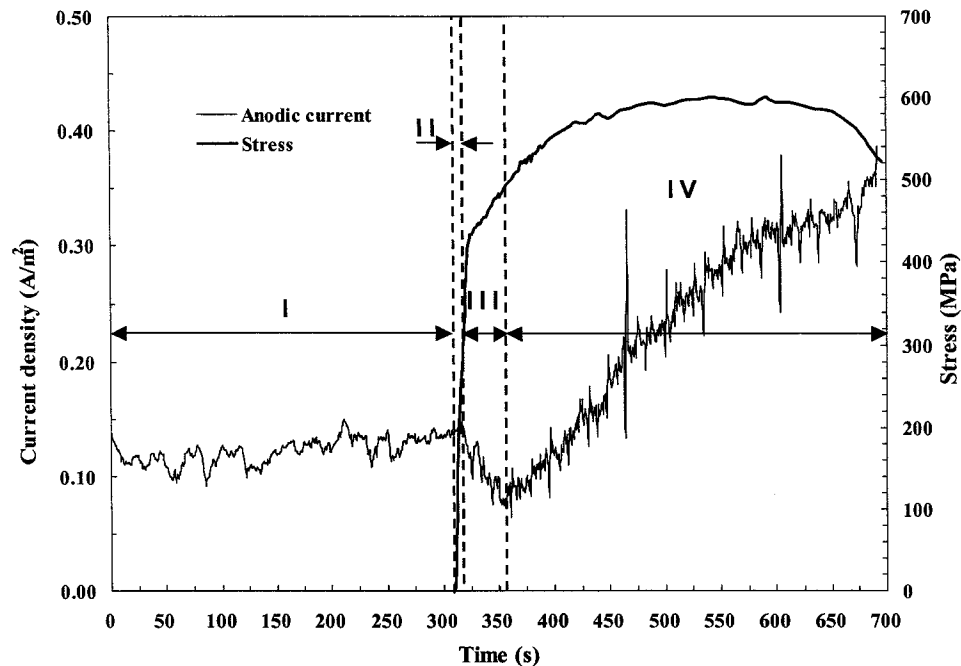
Figure 7-2 Anodic current changes during material straining process, anodic over-potential: 10 mV, strain rate: 4.92×10^{-4} s^{-1}

In the main plastic stage (t>357 s), the current density of dissolution showed an increase with the straining of the material. This part of the result agrees well with the results of other researchers (Garz and Hafke, 1971, Gutman et al., 1996, Sahal et al., 2004)) although their tests were all conducted for corrosion systems with active-passive transition. This interesting result could be explained as an increased activity of dissolution at the edges of the slip steps and an increased surface roughness caused by plastic deformation.

Conclusions

1. Anodic dissolution rate decreased slightly when the steel experienced elastic strain and a little bit of plastic strain.

2. Anodic dissolution rate increased when the steel experienced plastic strain.

117